공학박사학위논문

유동질식에 의한 불시동 및 경계층 유출을 통한 불시동 유동제어에 대한 실험적 연구

Experimental Studies of Choking-induced Inlet Unstart and its Control via Fast-acting Boundary-layer Suction

2021 년 2 월

서울대학교 대학원

기계공학부

강 경 래

유동질식에 의한 불시동 및 경계층 유출을 통한 불시동 유동제어에 대한 실험적 연구

Experimental Studies of Choking-induced Inlet Unstart and its Control via Fast-acting Boundary-layer Suction

지도교수 도 형 록

이 논문을 공학박사 학위논문으로 제출함

2020 년 10 월

서울대학교 대학원

기계공학부

강 경 래

강경래의 공학박사 학위논문을 인준함

2020 년 12 월

위 원 장 : 송 한 호 (인)

부위원장 : 도 형 록 (인)

위 원 : 황 원 태 (인)

위 원 : 양 인 영 (인)

위 원 : 임 성 균 (인)

Abstract

A comprehensive study on inlet unstart and its control via boundary-layer suction in a dual-mode scramjet is conducted. The current work encompasses i) modeling effort of boundary-layer suction in supersonic internal flows, ii) extensive experimental studies and analyses of inlet unstart under cold- and high-enthalpy conditions.

Firstly, boundary-layer suction in a dual-mode scramjet isolator was modeled as compressible laminar flow with non-zero wall-normal velocities in a constant-area channel to investigate the performance under different operating conditions. It was shown that the efficiency of boundary-layer suction is maximum at the suction rate of around 1 %. Also, it was turned out that the execution of suction control requires a few tens of milliseconds to be effective. Nevertheless, suction showed that choking mass flow rate can be increased more than 20 % at high confinement parameter and high suction rate conditions.

Then, boundary-layer suction control was implemented experimentally in unstarting and unstarted flows, and its effectiveness was experimentally investigated. A model dual-mode scramjet of a rectangular constant cross-sectional area was tested in an arc-heated supersonic blown-down wind tunnel. The model has an inlet, an isolator with a supersonic gaseous fuel injector, a combustor with

a backward-facing step cavity flameholder, and a nozzle to reproduce typical flow conditions in a dual-mode scramjet. Perforated plates were installed in the model to drive boundary-layer suction flow which was controlled by fast-acting solenoid valves. By switching on and off the arc-heater, high- and low-enthalpy freestream conditions could be provided approximately 0.5 s, which is typically long enough to simulate the whole process of inlet unstart. Accordingly, two sets of experiments are conducted for different objectives.

Under low-enthalpy conditions, inlet unstart was triggered by an excessive injection of a non-reacting jet under Mach 6 freestream. The primary objective is to improve understandings of the detailed processes and the dynamics of unstarting and unstarted flows. High-speed schlieren imaging covering the whole region of the internal flow was adopted to capture the temporal and spatial evolution of inlet unstart. Two jet injection rates were selected to vary the mass-loading of flow choking which leads to different completion times for inlet unstart. When boundary-layer suction was triggered at lower mass-loading fast enough, inlet unstart was completely avoided. Otherwise, inlet unstart could only be delayed by a few tens of milliseconds. Moreover, boundary-layer suction showed faster re-starting capability when combined with a jet cut-off.

On the other hand, shock-induced ignition from an ethylene fuel injection and consequent thermal choking incurred inlet unstart under high-enthalpy Mach 4.5 freestream. Under this combusting environment, the main aim was to seek inlet unstart precursors with pressure measurements and CH* chemiluminescence imaging to examine the effectiveness of boundary-layer suction. When the overall equivalence ratio was sufficiently low, the model was operated in a ramjet mode. When the equivalence ratio exceeded a certain value, an abrupt pressure drop, weakened high-frequency pressure fluctuations, and reduced CH* intensity variations are simultaneously observed, which were herein

regarded as inlet unstart indicators. These unstart indicators were shown significantly earlier with increasing equivalence ratios. When boundary-layer suction was activated near the unstart threshold, inlet unstart could be delayed by a few tens of milliseconds, even more than a hundred milliseconds, however, never suppressed solely by the suction. Inlet unstart was delayed longer and control still remained effective with trigger delays at higher suction rates.

Keywords: dual-mode scramjet, inlet unstart, flow control, boundary-layer suction

Student Number: 2016-20666

Acknowledgments

This thesis encompasses some of my work of five years of my graduate school. I knew nothing about scramjets and inlet unstart, but the extensive guidance, creative ideas, and supports from my advisor, associate professor Do, led me possible to accomplish this work. It is a shame I cannot list the names of all of you and thank every person individually in this thesis who helped me out to reach this point, but I would like to outline some of them here.

Firstly, Professor Seung Jin Song gave me invaluable intuitions on fluid dynamics and analytical skills to be a fluid dynamicist. His early guide in my master's course truly promoted me to cultivate essential engineering and analytical skills as a Ph.D. candidate. RFL members including Seong-ik Cha, Sungkyun Oh, Sangeun Bae, Juhyun Bae, Clémence Rubiella, Namyoung Kim, Youchan Park, Seon Woong Kim, Hosung Byun, Taekeun Yoon, and Kyeongsun Kim, also recently Jonggyu Choi and Jongwun Choi always have encouraged and inspired me to improve my work.

Also, Lydia Wermer, Nozomu Kato, and associate Professor Sungkyun Im helped me out so much in the U.S. to get the experimental data. I really appreciate the opportunity to perform the experiment at the university of Notre Dame and If it had not been for them, I would not have been able to conduct

the experiment, get the data, and organize as thoroughly as now.

Last but not least, my family, my father Kyungwoon, my mother Im-joo, and my sister Na-Yeon have been always supportive and believed me to get me through here.

There are dozens of other people who should have been mentioned as well but although I did not, I equally and genuinely appreciate all of them.

Table of Contents

List of Figures

List of Tables

Nomenclature

Alphabetical

$\dot{m}$	Mass flow rate
A	Area
C_p	Pressure coefficient
c_p	Isobaric specific heat
CMR	Internal-to-choked mass flow rate ratio
dtS	Suction activation trigger relative to the jet injection trigger
$dtS2$	Suction activation trigger relative to the (virtual) unstart indicator
f	Darcy friction factor
H	Half the height of the channel for modeling
h	Enthalpy
JMR	Jet-to-freestream mass flow rate ratio
L	Longitudinal length of each wall of the model

L_x	Stream-wise length of the suction for modeling
Ma	Mach number
P	Pressure
Pr	Prandtl number
Q	Heat transfer
R	Specific gas constant
Re_x	Reynolds number based on the stream-wise length
T	Temperature
u	x-velocity
V	Velocity magnitude
v	y-velocity
v_s	Suction-induced wall-normal velocity
x	Stream-wise coordinate
y	Wall-normal coordinate

Greek letters

δ	Velocity boundary-layer thickness
γ	Specific heat ratio
κ	Thermal conductivity
ψ	Stream function

μ	Dynamic viscosity
ϕ	Equivalence ratio
ρ	Density
σ	Standard deviation of time-averaged CH* image intensity
τ	Shear stress
τ_s	Characteristic time-scale of boundary-layer suction activation

Subscripts

0	Total property
∞	Freestream static property
f	Freestream property
j	Jet property
ref	Properties at the reference state
w	Properties at wall

Chapter 1

Introduction

Inlet unstart is a unique flow feature for flow Mach number greater than unity. Simplified flows of supersonic/hypersonic internal flows are introduced here to better understand the quintessential phenomenology of unstarting and unstarted flows. Then, previous studies for simulating inlet unstart and flow control strategies in supersonic internal flows are given. Finally, research motivation and the scope of the current study are presented.

1.1 Dual-mode Scramjet Engine

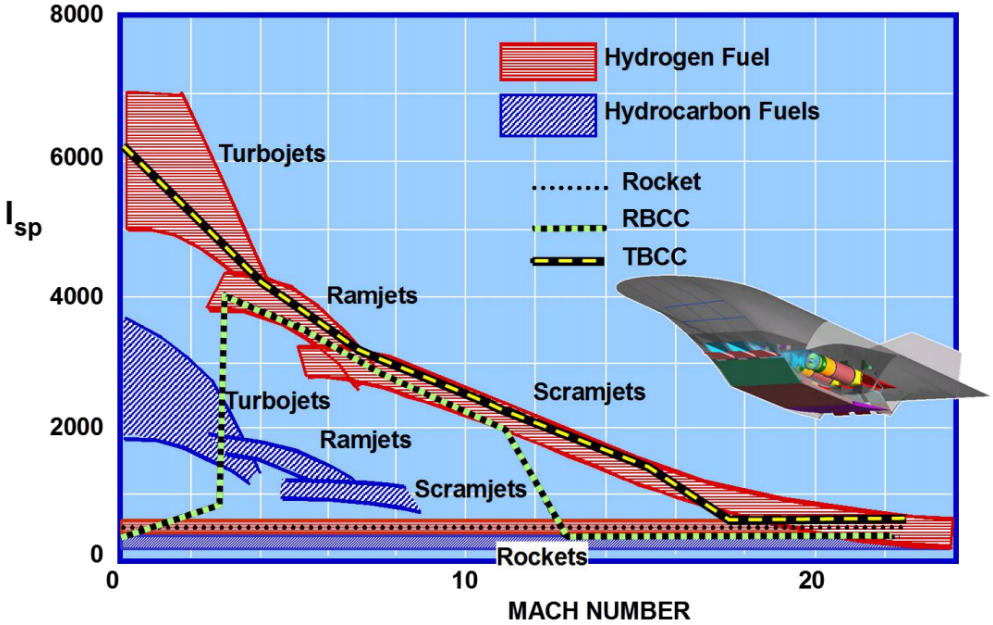

Fig. 1.1 Typical specific impulses of various propulsion systems [1]

Ramjets and scramjets are developing next-generation air-breathing propulsion systems that aim for fuel-efficient supersonic and hypersonic cruise flights [3–6, 8, 9, 24–71]. As an illustrative comparison, typical specific impulses from cycle analyses of ramjets and scramjets along with turbofan and rocket, representing conventional propulsion systems, are presented in Fig. 1.1. The turbojet-based cycles (e.g. turbofans with afterburners) have been the most popular engine and they are very efficient in low Mach number (around $Ma < 1.5$) flights. However, turbojets abruptly lose the efficiency at flight Mach numbers over 3. Theoretically, between Mach numbers of 3 and 6, ramjet is more efficient than any other cycle presented here. If the cruise flight Mach number exceeds 6, scramjet is now the most efficient cycle, covering Mach numbers up to 10. Al-

though rockets can also be used for high Mach number flights, those have to load oxidizer and fuel at the same time, reducing their specific impulses inherently.

Comparative schematics for turbojets, ramjets, and scramjets are presented in Fig. 1.2 to understand the prime differences between the propulsion systems. Most of air-breathing engines have three major components: compression, combustion, and expansion. Compression parts decelerate and compress the captured stream to be adequate for the combustion reaction downstream. Combustion parts inject/mix fuel and burn to convert fuel's chemical energy into the flow's kinetic energy. Expansion parts accelerate the flow such that pressure/momentum difference can generate thrust. For turbojet-based propulsion systems (Fig. 1.2(a)), compressors and turbines are the compression and the expansion devices, respectively. Those rotating machines can be efficient specifically in subsonic and low supersonic regimes. However, as the flight Mach number increases, shockwave structures upstream of the compressor are formed inevitably, significantly reducing the efficiency of the compressor and the engine.

As an alternative cycle for supersonic cruise flights, ramjets (Fig. 1.2(b)) utilize the very shockwave structure that decreased the efficiency for the turbojet engines since shockwaves in nature decelerate and compress the flow. Therefore, an inlet, or the compression part of ramjets and scramjets, is designed such that the shockwave structures in the inlet are well controllable and predictable so that the inlet can supply adequate inflow for the combustor.

As shown in Fig. 1.1, ramjets can be efficient between flight Mach numbers of 2 and 5. However, beyond flight Mach number of 5, the losses from flow deceleration at the inlet are exceedingly significant as ramjet inlets have to decelerate the flow to subsonic. Therefore, a supersonic-combustion ramjet or shortly scramjet is proposed which burns fuel in supersonic streams. By adopting supersonic combustors, fuel-economy at hypersonic speeds can be significantly increased.

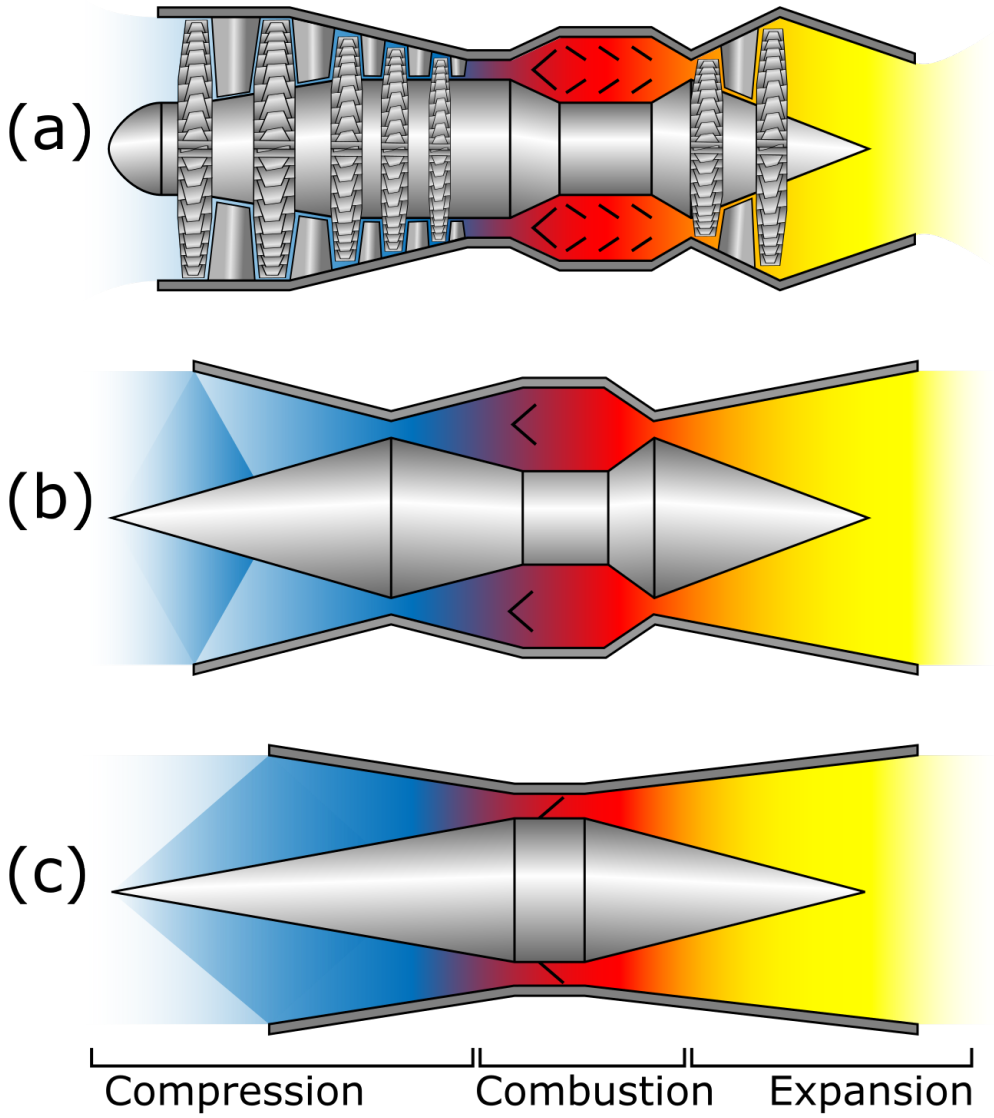

Fig. 1.2 Comparative schematics for (a) turbojets, (b) ramjets, and (c) scramjets [2]

However, since the residence time of the fuel-air mixture in the combustor is considerably reduced, enhancing mixing and combustion efficiency becomes one of the key problems for designing scramjets.

As mentioned above, ramjets and scramjets share the operating mechanism of the inlet but different combustors. Therefore, the dual-mode concept is proposed, combustor of which can operate under both ram- and scram-mode. By adopting multi-mode combustors, a dual-mode scramjet can operate efficiently in a broader Mach number regime. However, The transition between the operational modes is strongly coupled with the operational conditions, including flight Mach number, angle of attack (AoA), altitude, and fueling rate, and significantly change the vehicle performance [6, 10, 72–82]. Due to this complexity, some dual-mode concept adopts separate flow paths for ram- and scram-mode operation [3]. Therefore, a thorough analysis considering transient trajectory information with an appropriate mode transition logic [1, 62, 80, 82–86]is required for designing and operating a dual-mode scramjet.

In summary, ramjets and scramjets are proposed and studies specifically for supersonic/hypersonic air-breathing cruise flights. The biggest difference from the conventional propulsion system comes from the inlet, which passively compresses the captured stream with shockwaves at the inlet. Because of this passiveness, the design and the operation of ramjets and scramjets are highly dependent on operational conditions, and each component is closely related to each other. In the following sections, general considerations for designing and operating each component of a typical ramjet/scramjet (or a dual-mode scramjet) are presented, excluding the nozzle which has relatively small significance.

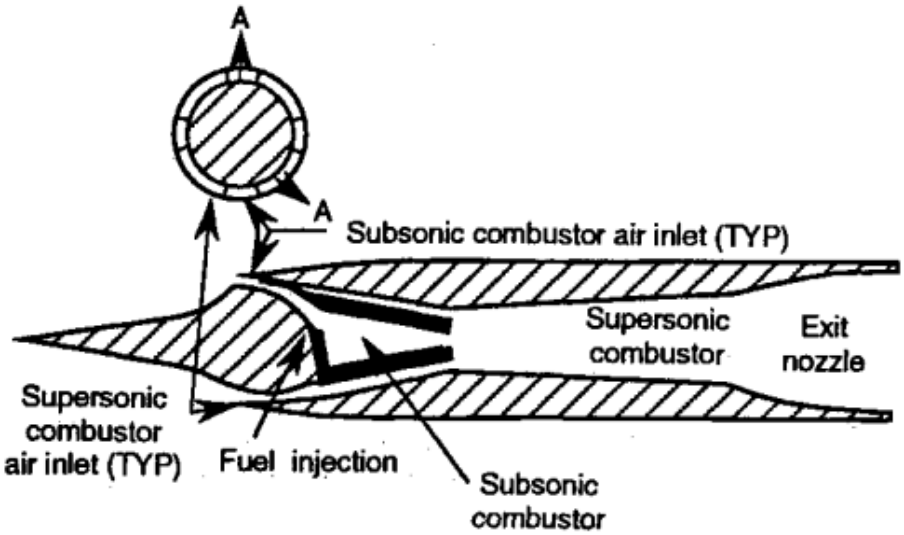

Fig. 1.3 A schematic of dual combustor scramjet [3]

1.1.1 Compression: Inlet

Inlet forms a shockwave structure inside to compress and decelerate the capture flow which inevitably induces loss across it. This shockwave loss is most commonly represented as total pressure recovery (TPR), which is essentially a ratio of total pressures across the inlet (at the capture and the exit).

$$TPR = \frac{P_{0,exit}}{P_{0,capture}} \tag{1.1}$$

To maximize TPR, the shockwave structure must be predictable at the design stage. For this reason, two-dimensional inlets having rectangular or circular cross-sectional areas have been most widely used for investigations since the shockwave structure is relatively easily predictable with inviscid oblique shockwave relations or Taylor-Maccoll equations [13, 26, 30, 41, 62, 87–92].

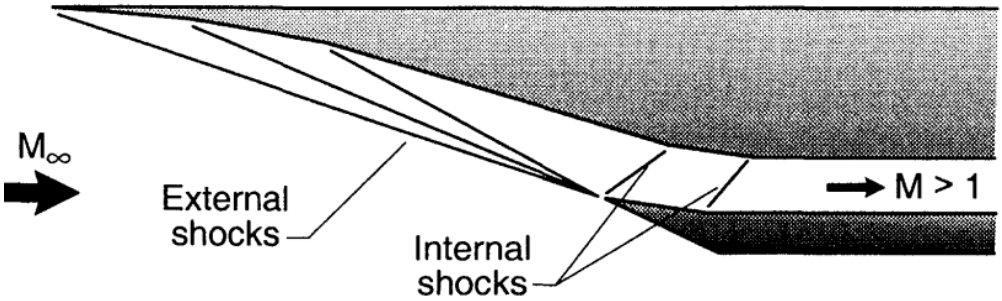

Fig. 1.4 Schematic of a two-dimensional scramjet inlet [4]

Moreover, two-dimensional inlets, both rectangular and circular, often adopt multiple-shock configurations to reduce shock losses by distributing the required pressure rise since the shock loss is proportional to the square of Mach number. Although their design methodology and resultant geometries are simple, the internal flow field and the performance is highly sophisticated especially at off-design conditions [33, 40, 61, 63, 64].

There are also inlets with three-dimensional design methodologies [36, 39, 57–60, 68], the most popular being based on the streamline-tracing inlets [7, 57–60, 68]. SCOOP inlet is one of the stream-tracing inlets which is designed by tracing circular capture shape in a base compression field, resulting in a circular exit [7, 68, 93]. There are also streamline transition inlets such as the rectangular-to-elliptical transition inlet [57–60]. This method is a variant of the stream-tracing concept that the desired shape is formed by tracing multiple capture shapes at the inlet and the cross-sectional shape is smoothly changed from one to another via a transition function. As a result, REST has different capture (rectangular) and exit (elliptical or circular) shape. The three-dimensional inlets are known to show better performances than two-dimensional inlets near on-design conditions. Moreover, three-dimensional inlets have better starting characteristics than equivalent two-dimensional inlets having the same static

pressure rise [58–60, 68].

Fig. 1.5 A rectangular-to-elliptic shape transition (REST) inlet [5]

Unlike subsonic inlets, supersonic inlets could be started or unstarted. Since supersonic inlets are designed to swallow supersonic flow inside, this state is defined as the started state and vice versa [94]: unstarted with subsonic flows.

For a fixed geometry inlet, this process requires lower backpressures, showing hysteresis: start/unstart characteristic depends on the previous state [95–98]. One of the geometric parameters that affect the performance and the start/unstart characteristic of inlets is the contraction ratio (CR), which is an area ratio between the capture (inlet) and the throat section.

$$CR = \frac{A_{capture}}{A_{throat}} \tag{1.2}$$

For example, the starting/unstarting boundary of a given inlet can be defined as a function of CR, Mach number, Angle of Attack (AoA), and so on. The Kantrowitz limit could tell the starting limit and is obtained by assuming isentropic flow with choking (no shockwave losses) across the inlet, acting as the lowest limit for self-starting inlet [99].

$$\begin{aligned} CR_{Kantrowitz} = \frac{1}{Ma^2} & \left[\frac{(\gamma+1)Ma^2}{(\gamma-1)Ma^2+2}\right]^{\frac{\gamma}{\gamma-1}} \\ & \left[\frac{\gamma+1}{2\gamma Ma^2-(\gamma-1)}\right]^{\frac{1}{\gamma-1}} \left[\frac{1+\gamma-1/2Ma^2}{\gamma+1/2}\right]^{\frac{\gamma+1}{2(\gamma-1)}} \quad [99] \end{aligned} \tag{1.3}$$

Typical starting limit of two-dimensional and three-dimensional inlets are presented in terms of the reciprocal of CR in Fig. 1.6. Since the Kantrowitz limit does not consider complex flow phenomena at the inlet, the maximum CR deviates from the Kantrowitz limit, starting at much higher CRs [40, 64, 67, 100]. However, CRs cannot be higher than that from the isentropic limit, which is the lower limit of the starting envelope in Fig. 1.6.

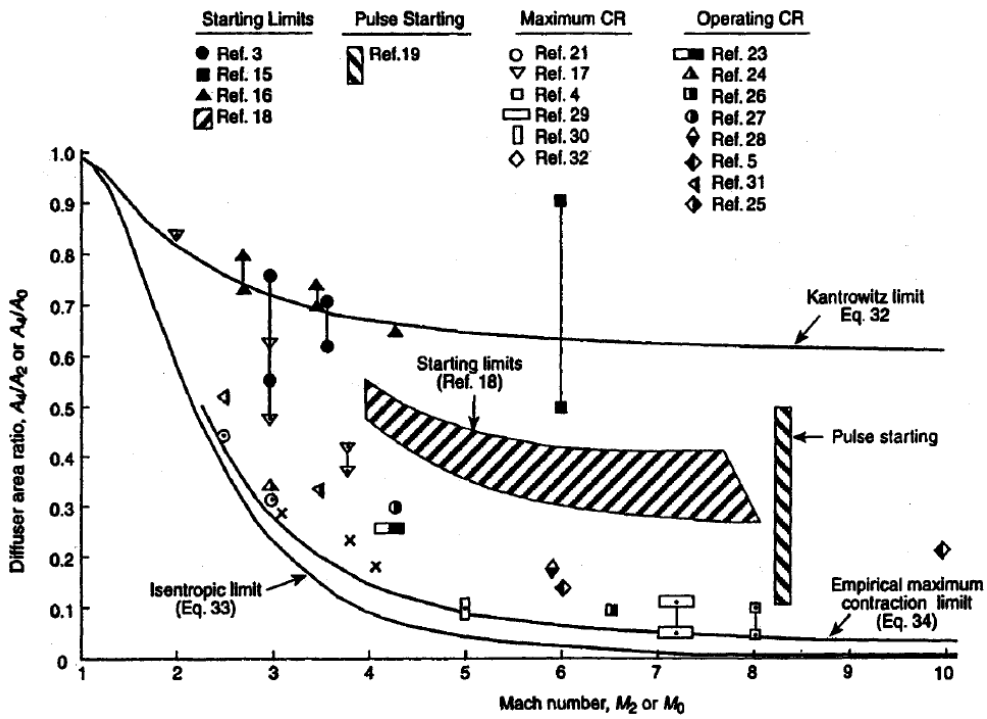

Fig. 1.6 Starting and maximum contraction ratio (CR) limits [6]

Although an inlet is firstly started, the inlet could suffer from unstart due to flow phenomena downstream, for example, severe backpressure rise and flow choking. Therefore, one of the key performance parameters of supersonic inlets is the starting capability which is evaluated in terms of unstarting margin [67, 101–104]. The margin from the unstart limit can be defined in various ways, the most simple parameter being the outlet Mach number. This is a common parameter for scramjet operation as flow Mach number tends to decrease in the streamwise direction due to frictional and thermal choking in the passage, and highly likely to be unstarted once choked at the combustor [87, 105–110].

1.1.2 Compression: Isolator

For ramjets and scramjets, an inlet is a device to form a shockwave in- or outside of the engine providing an adequate amount of compressions and flow decelerations. However, if the inlet is directly connected to a combustor, the inlet could suffer from inlet unstart due to pressure fluctuations and excessive pressure rise at the downstream combustor. Thus, an isolator is often installed between the inlet and the combustor to "isolate" the pressure information [6, 74]. For this reason, isolators are often simple ducts with constant-area or a small expansion to compensate for the viscous effect, since the stream-wise isolation of the inlet from the combustor is the key operating mechanism [34, 35, 42, 49, 50, 53, 71].

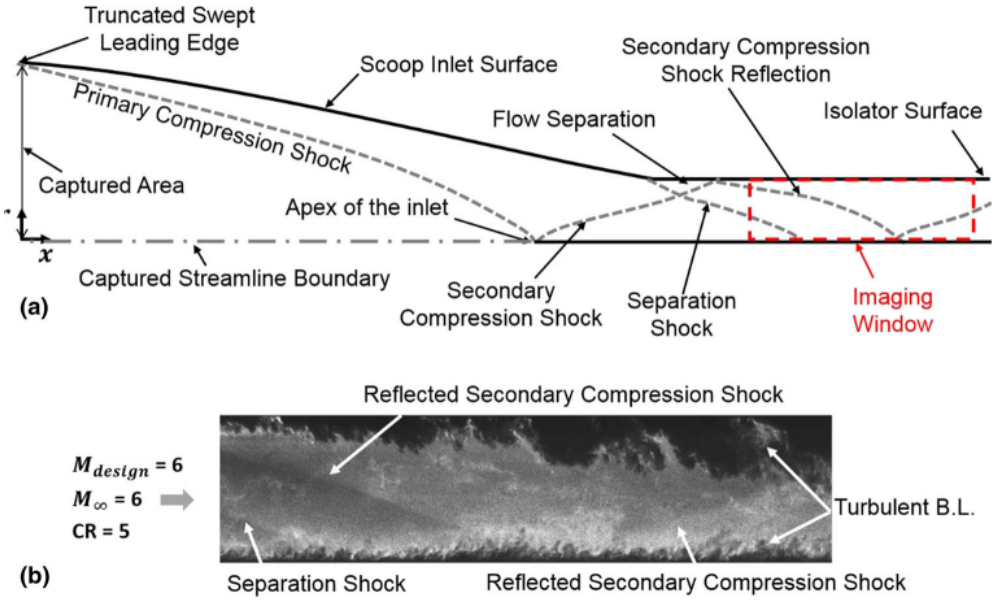

Fig. 1.7 (a) A schematic of the expected shockwave structures in SCOOP inlet, and (b) a visualized isolator flow by PLRS imaging [7]

Although the performance objective is rather simple, there still exist oblique shockwave reflections and perhaps pseudo-shockwave structures in the isolator,

therefore, the shockwave structure from the inlet to the isolator is commonly referred to as pre-combustion shockwave train (PCST), For this reason, an isolator is usually considered as a compression device since an isolator can contribute considerably to the overall pressure rise due to the PCST and viscous effect (effective area decrease).

A longer isolator would offer a larger buffer for the pressure disturbances at the downstream to keep an inlet started, but also increases the internal drag (skin friction) loss, resulting in decreased choked flow rates (unstart margin); therefore, the length of the isolator must be compromised [49]. To estimate the needed length of an isolator, experimental correlations are developed for pressure rise [50, 71]. Meanwhile, the PCST structure in the isolator specifically is sometimes assumed as a pseudo-shockwave structure, which is formed by a complex SBLI in a constant-area duct [8, 53, 111, 112]. For pseudo-shockwave structures, analytical modelings are also possible [8, 70, 113, 114], providing flow properties as a function of the stream-wise direction.

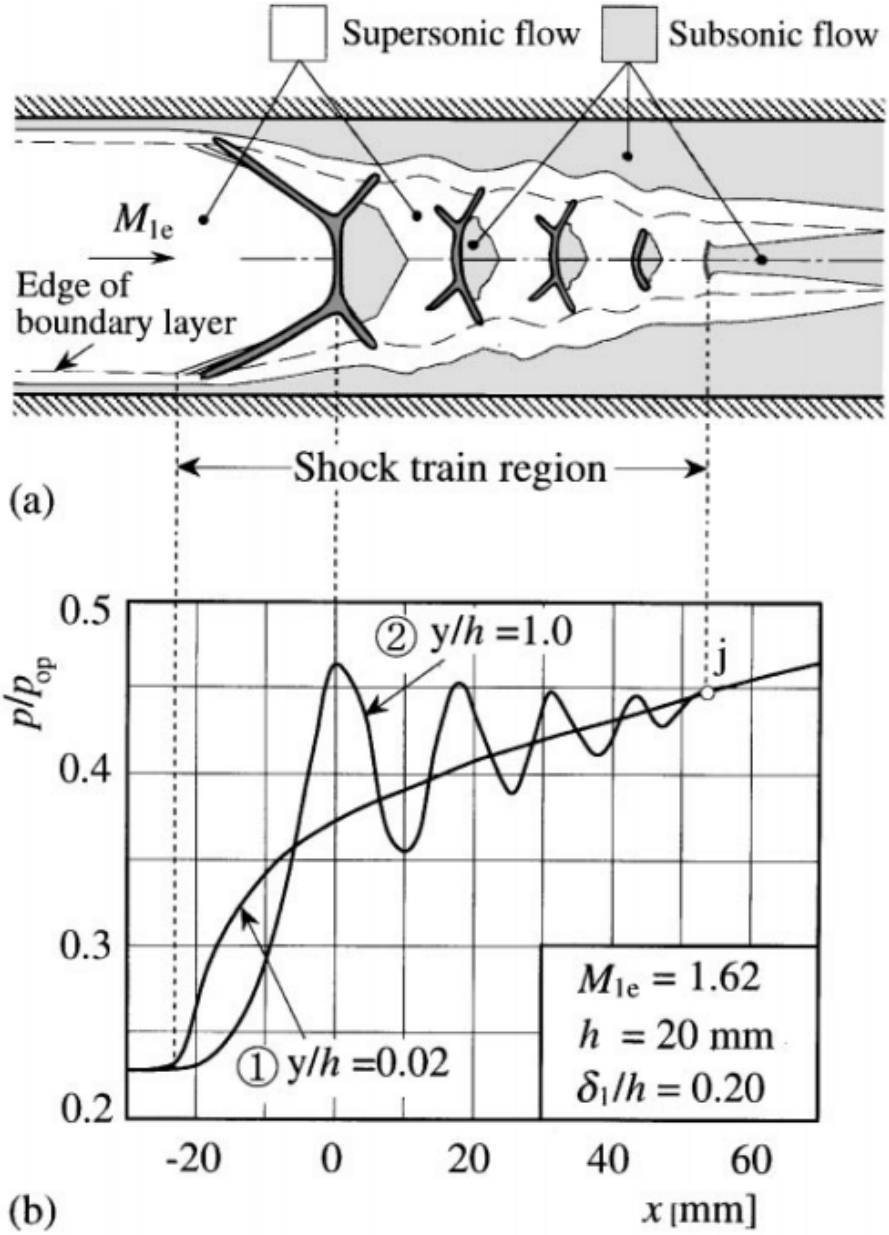

Fig. 1.8 (a) A schematic of pseudo-shockwave, and (b) a typical wall-pressure profile [8]

1.1.3 Combustion: Combustor

Ramjets burn fuel in subsonic streams while scramjets in supersonic. Therefore, fuel injection scheme and rate, ignition, and flame holding methods are used differently depending on the operation modes. To avoid this complexity in a dual-mode scramjet, two independent combustors (one subsonic and the other supersonic) and corresponding two flow paths are often installed at the same time and the captured air from the inlet is bypassed through either of the combustors to accomplish the dual-mode operation. The cross-sectional shape of the supersonic combustor is predominantly determined by the shape of the inlet and the isolator since any abrupt area change in supersonic streams would incur excessive losses; for example, rectangular combustors for two-dimensional rectangular inlets [24, 26, 27, 38, 43], circular combustors for SCOOP inlet [7, 68, 93], elliptical combustors for REST inlets [5, 9, 66]. In contrast, subsonic combustors are relatively free from this issue.

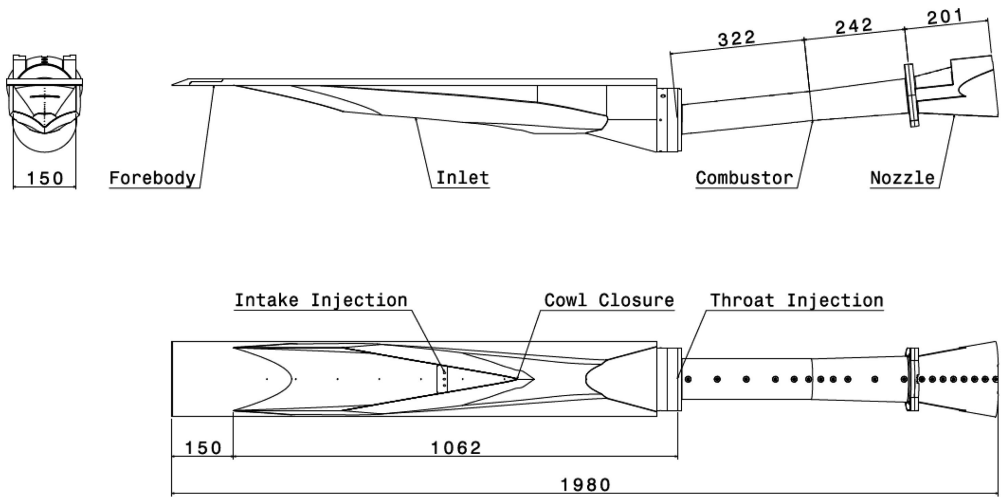

Fig. 1.9 An elliptical combustor with a REST inlet [9]

Since the whole process of fuel injection to subsequent supersonic combustion

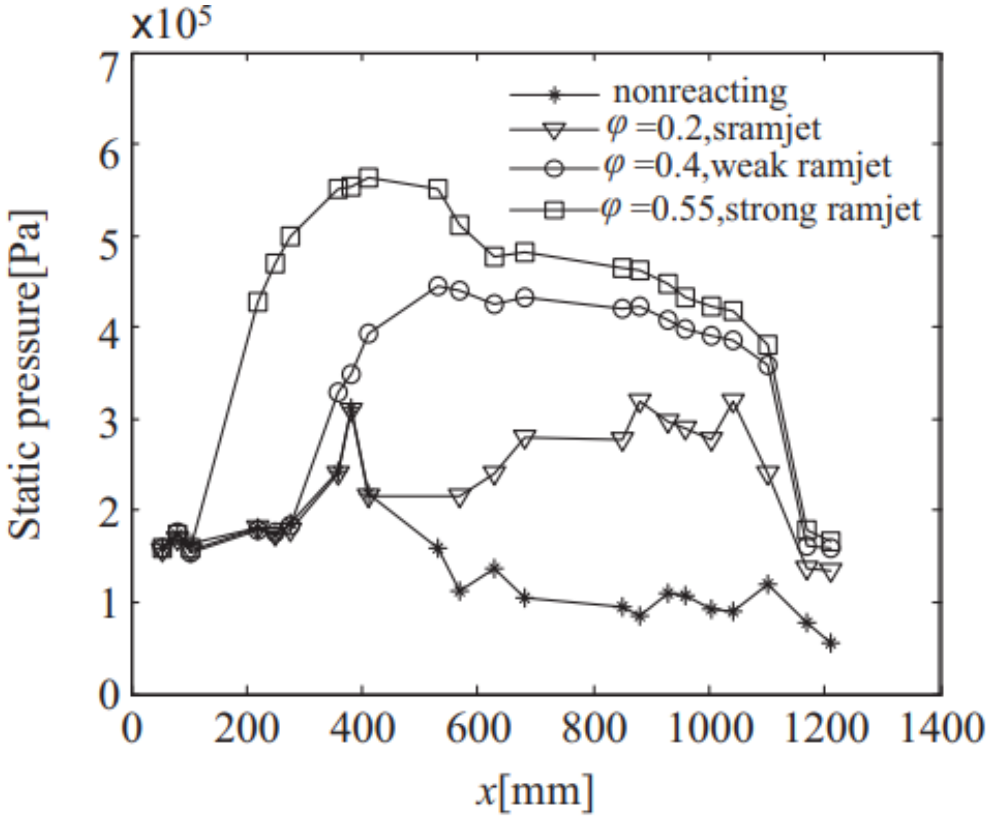

Fig. 1.10 Mode transition due to change of the equivalence ratio (φ) [10]

must take place in a very short time under scram-mode operation, there have been rigorous research efforts to successfully stabilize the flame and to enhance combustion efficiency for supersonic combustors [3, 25, 27, 27–30, 38, 43, 45, 46, 48, 51, 52, 54–56, 69]. Nevertheless, one of the biggest issues of designing and operating a combustor of a ramjet/scramjet vehicle is avoiding thermal choking, which could lead to non-spontaneous mode transition to ram-mode or unstart-mode [47, 87, 90, 105–110, 115]. Especially under scram-mode operation, the internal passages are designed such that the core stream maintains supersonic speeds: there must be no throat throughout the flow field. Therefore, once the

flow is choked before expanded through the nozzle, the flow downstream of the choked throat is highly likely to turn subsonic, possibly leading to inlet unstart [17, 105, 115–117]. For ramjet operations, flow is once turned to subsonic before the combustor and has to become supersonic again at the exit. In other words, a choked throat is needed between the combustor and the nozzle [80, 82, 84]. However, any inappropriate location of the choked throat would deteriorate the performance: premature choking likely leads to inlet unstart whereas late choking could result in significant under-expansion and subsequent thrust losses. Therefore, an accurate description of the operating envelope and unstart margin is required for better performance.

1.2 Flow choking

Inlet unstart is a sophisticated flow phenomenon that accompanies multiple sophisticated flow phenomena including a high level of turbulence, a complex shockwave structure, boundary-layer separation, shockwave/boundary-layer interaction (SBLI), mass injection, and frictional/thermal choking [12–17, 85–90, 95, 96, 98, 100–110, 115–140]. For this reason, accurately predicting or simulating inlet unstart is still challenging. Nevertheless, simplified equations with appropriate assumptions can still reflect the important features of the target flow phenomenon. Thus, supersonic internal flows, specifically supersonic duct flows, are reduced under certain assumptions to elucidate the flow parameters that affect inlet unstart. The most common practices for simplification are steady and one-dimensional assumptions. In addition to these assumptions, heat transfer or skin friction can be neglected to yield simpler flows, Fanno flow, and Rayleigh flow, respectively.

1.2.1 Ideally Choked Flow: Isentropic Flow with Area Changes

In the previous section, steady and one-dimensional flow assumptions are introduced. For a compressible duct flow, the most ideal and simplified condition is to assume there is no losses (isentropic) and no heat transfer (adiabatic). As the problem is one-dimensional, every variable is only a function of the streamwise distance, x. Then, combining the equation of continuity, momentum, and energy yields

$$\frac{dp}{\rho} + VdV = 0 \tag{1.4}$$

Given the definition of the speed of sound, eliminating dp and $d\rho$ terms in the equation of continuity and momentum leads to Eq. (1.5), expressing the relationship between the changes of area and velocity depending on the Mach number range.

$$\frac{dV}{V} = \frac{dA}{A}\frac{1}{Ma^2 - 1} \tag{1.5}$$

When the flow is subsonic ($Ma < 1$), dV and dA are on the opposite signs: velocity increases with decreasing areas and vice versa. However, in supersonic flows ($Ma > 1$) velocity increases with increasing areas since dV and dA are on the same signs. The sonic point ($Ma = 1$) is the critical point where this change occurs. When all the properties are expressed at the sonic point, the relationship between the Mach number and the area change can be obtained,

$$\frac{A}{A^*} = \frac{1}{Ma}\left[\frac{1 + \frac{1}{2}(\gamma - 1)Ma^2}{\frac{1}{2}(\gamma + 1)Ma}\right]^{(1/2)(\gamma+1)(\gamma-1)} \tag{1.6}$$

where the superscript * represents the properties at the sonic point.

Meanwhile, the right side of the Eq. (1.6) is zero when $Ma = 0$, unity at $Ma = 1$, and down to zero again for high Mach numbers. Therefore, the maximum allowable flow rate is realized at $Ma = 1$ (sonic condition) for given conditions. For a given stagnation condition, a flow is said to be choked if the mass flow rate does not increase unless the throat area is increased: the maximum allowable flow rate is determined by the stagnation conditions and the throat area. The

maximum flow rate is then expressed as Eq. (1.7).

$$\dot{m}_{max} = \rho^* A^* V^* = \gamma^{\frac{1}{2}} \left(\frac{2}{\gamma + 1} \right)^{(1/2)(\gamma+1)(\gamma-1)} \frac{P_0 A^*}{(RT_0)^{1/2}} \tag{1.7}$$

Finally, a mass flow rate ratio between the incoming (captured) and the choked can be defined at an arbitrary station using Eq. (1.6) and Eq. (1.7) with given flow conditions, which is herein defined as the internal-to-choked mass ratio (CMR).

$$CMR = \frac{\dot{m}_{captured} + \dot{m}_{added}}{\dot{m}_{choked}} \tag{1.8}$$

1.2.2 Compressible Duct Flow with Friction: Fanno Flow

In the previous section (Section 1.2.1), the concept of flow choking and maximum allowable flow rate (choked flow rate) are introduced, which are deduced under frictionless (isentropic) and adiabatic assumptions. In the present section, the skin friction effect at the wall is added for compressible internal flows. For simplicity, area change along the stream-wise direction is neglected ($\frac{dA}{dx} = 0$). Other assumptions, such as steady and one-dimensional, stay the same. This kind of flow is often referred to as "Fanno flow".

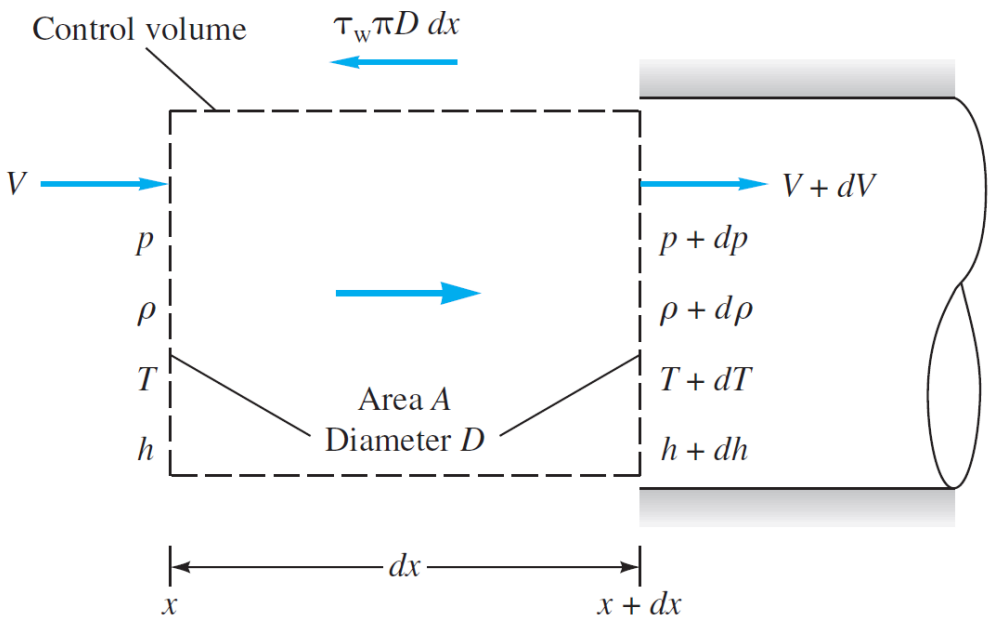

Fig. 1.11 Control volume analysis for Fanno flows [11]

A control volume analysis of such flow is presented in Fig. 1.11. The main differences from the previous section are i) no area change considered, ii) the shear stress (τ_w) is now considered to reflect the skin friction effect at the wall. The equations of continuity, momentum, and energy take the form below, respectively.

$$\frac{d\rho}{\rho} + \frac{dV}{V} = 0 \tag{1.9a}$$

$$-AdP - \tau_w \pi D dx = \dot{m} dV \tag{1.9b}$$

$$c_p dT + V dV = 0 \tag{1.9c}$$

To close the equations, perfect-gas law and Darcy friction factor (f) are introduced.

$$\tau_w = \frac{1}{8} f \rho V^2 = \frac{1}{8} f \gamma P Ma^2 \tag{1.10}$$

Combining three equations in Eqs. (1.9a) to (1.9c) and use the definition of Mach number, the change of pressure, density, stagnation pressure, temperature, and Mach number as a function of flow inlet Mach number (Ma), diameter (D), specific heat ratio (γ), and Darcy friction factor (f) can be obtained as below.

$$\frac{dP}{P} = -\gamma \ Ma^2 \frac{1 + (\gamma - 1) Ma^2}{2(1 - Ma^2)} f \frac{dx}{D} \tag{1.11a}$$

$$\frac{d\rho}{\rho} = \frac{\gamma Ma^2}{2(1 - Ma^2)} f \frac{dx}{D} = -\frac{dV}{V} \tag{1.11b}$$

$$\frac{dP_0}{P_0} = -\frac{1}{2} \gamma Ma^2 f \frac{dx}{D} \tag{1.11c}$$

$$\frac{dT}{T} = -\frac{\gamma(\gamma - 1) Ma^4}{2(1 - Ma^2)} f \frac{dx}{D} \tag{1.11d}$$

$$\frac{dMa^2}{Ma^2} = \gamma Ma^2 \frac{1 + \frac{1}{2}(\gamma - 1) Ma^2}{1 - Ma^2} f \frac{dx}{D} \tag{1.11e}$$

It is interesting to note that every working relation except for the stagnation pressure in Eqs. (1.11a) to (1.11e) has the factor $(1 - Ma^2)$ in the denominator,

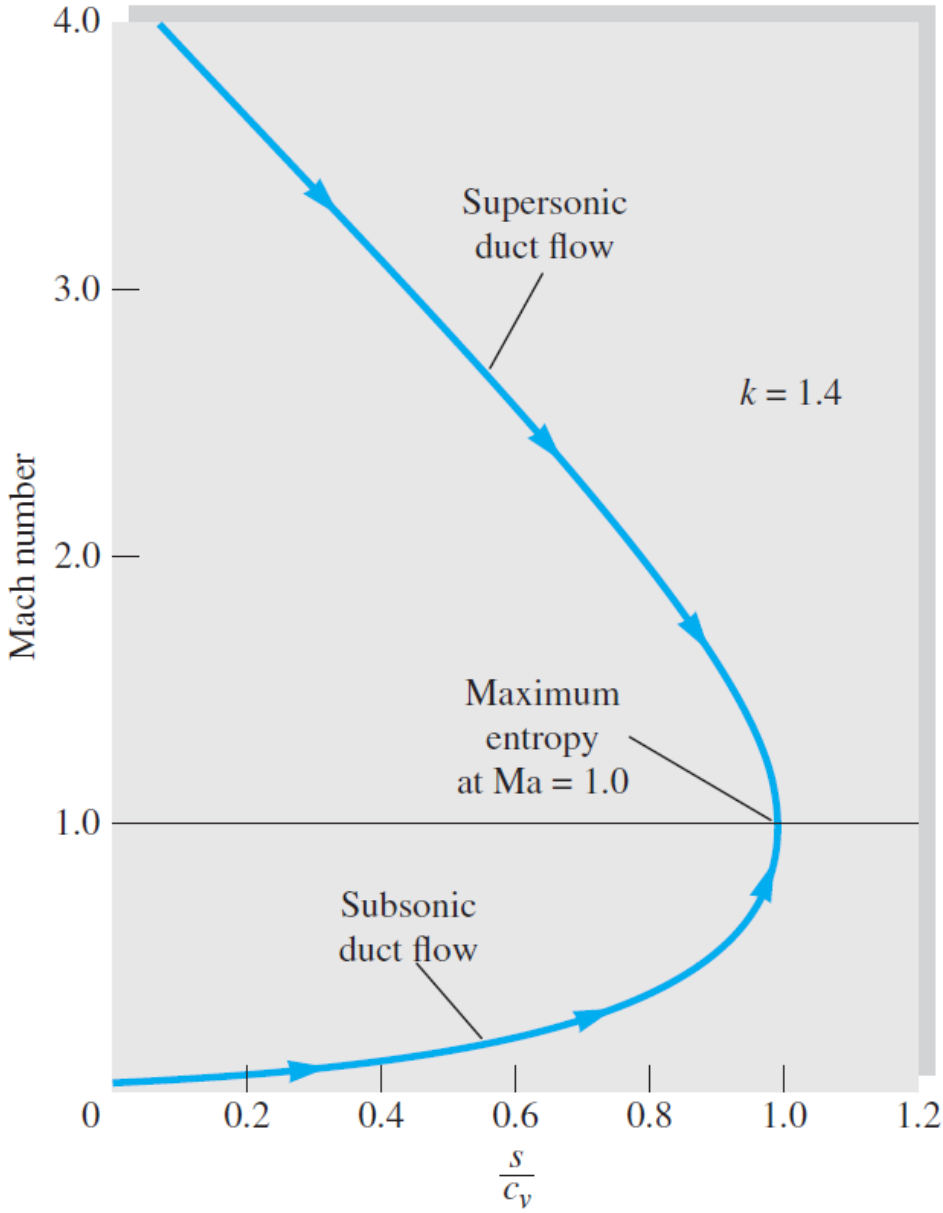

Fig. 1.12 Fanno plot: Mach number versus entropy [11]

having the same effect as in Eq. (1.5): the change is dependent on *Ma*. The stagnation pressure must be decreasing along the stream-wise direction to satisfy

the second law of thermodynamics since entropy is never decreasing for adiabatic flows.

Among the equations in Eqs. (1.11a) to (1.11e), the Mach number relation is worth noting. Because of the factor of $(1 - Ma^2)$ in the denominator, the Mach number always tends to change towards unity: flow is "frictionally choked" in the end. It becomes more obvious if the change of the Mach number is expressed in terms of entropy. This can be done by combining pressure (Eq. (1.11a)) and density (Eq. (1.11b)) along with the definition of entropy. For the specific heat ratio of 1.4, entropy versus Mach number is plotted in Fig. 1.12. It is now clear that the maximum entropy occurs at the Mach number of unity, making the flow Mach number heading towards $Ma = 1$ regardless of subsonic or supersonic.

1.2.3 Frictionless Duct Flow with Heat Transfer: Rayleigh Flow

In the previous section, it was shown that Mach numbers in duct flow always tend to increase/decrease towards unity under skin friction effect at the wall. Now, heat addition/rejection in a constant area duct is considered in the current section. A control volume analysis for such flow commonly referred to as "Rayleigh flow", is presented in Fig. 1.13.

For a one-dimensional Rayleigh flow, the incoming and outgoing fluxes are calculated at stations 1 and 2, and an incremental amount of heat transfer (δQ) is considered at the boundaries of the control volume. Combined with the assumptions of steady and constant-area flow, the simplified equations of continuity, momentum, and energy take the form below, respectively.

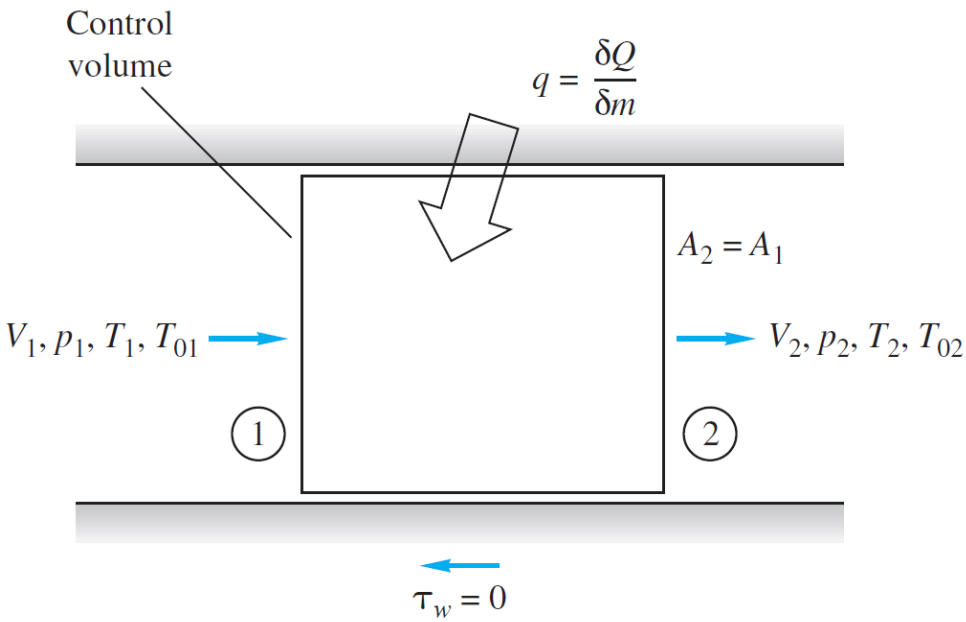

Fig. 1.13 Control volume analysis for Rayleigh flow [11]

$$\rho_1 V_1 = \rho_2 V_2 = G = const \tag{1.12a}$$

$$P_1 - P_2 = G(V_2 - V_1) \tag{1.12b}$$

$$\delta\dot{Q} = \delta\dot{m}(h_2 + \frac{1}{2}V_2^2 - h_1 - \frac{1}{2}V_1^2) \tag{1.12c}$$

The heat transfer at the boundaries changes the temperature (or more strictly the stagnation enthalpy) of the flow. Therefore, it is natural to plot the change of the Mach number in terms of the change of the stagnation temperature of the flow. For a given heat transfer rate ($\delta\dot{Q}/\delta\dot{m}$), Eqs. (1.12a) to (1.12c) can

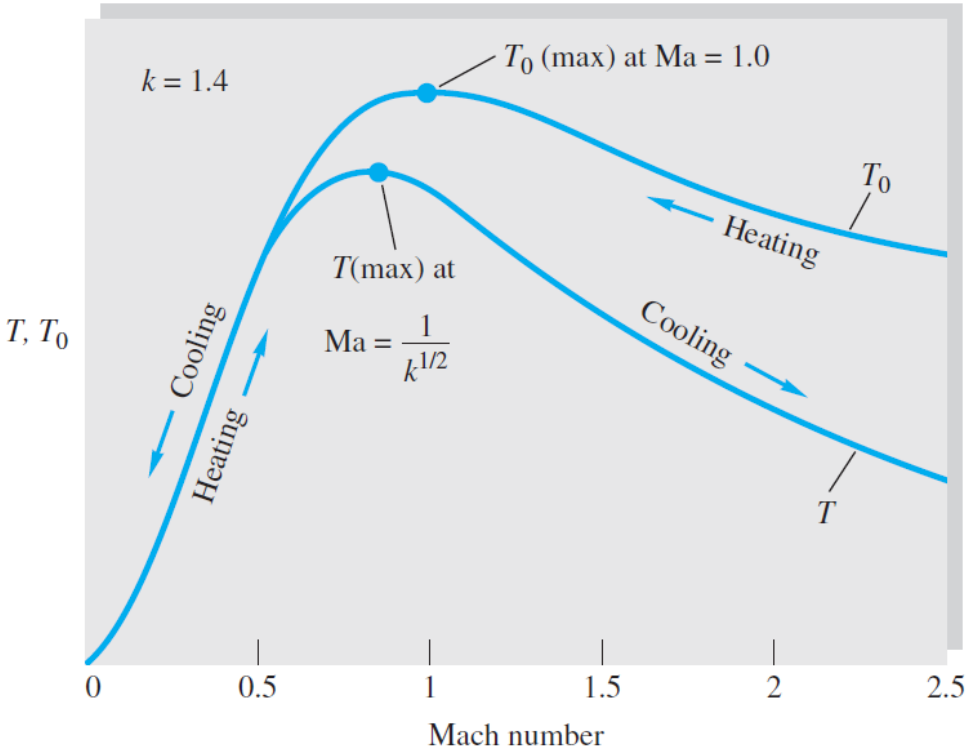

Fig. 1.14 Rayleigh lines: stagnation temperature versus Mach number [11]

be solved algebraically for property ratios (such as P_2/P_1) with the perfect-gas and Mach number relations, resulting in Fig. 1.14.

1.3 Inlet Unstart

In Section 1.1, typical features of each device in a dual-mode scramjet have been introduced. Depending on operational conditions, a dual-mode scramjet can operate in either ram- or scram-mode and switch from one mode to another [72, 75, 82]. As opposed to this voluntary mode transition, there exists the third operation mode under which flow turns subsonic non-spontaneously, which is called "inlet unstart". The term "unstart" came from the term "started" which refers to a state wherein a supersonic internal flow device has swallowed a supersonic flow. Now it is clear that the term "unstart" refers to the opposite state, a subsonic flow in a supersonic device [94]. If an inlet is unstarted, the engine suffers from a significant loss of net thrust and control, possibly leading to a catastrophic failure [6, 74, 105].

Typical flow structures captured with schlieren imaging for ram-, scram-, unstart-mode operation are shown in Fig. 1.15. When the model is operating as scram-mode (Fig. 1.15(a)), oblique shockwave and Mach wave structures are clearly seen at the inlet, remaining the internal flow supersonic until it reaches the fuel jet. Moreover, the flow structure of jet-in-crossflow in supersonic freestream is visualized by schlieren imaging.

When the model is operating in a ram-mode (Fig. 1.15(b)), there is a strong shockwave structure at the inlet (the vertical white element) to decelerate flow to subsonic. As a result, the supersonic jet structure is not seen in ram-mode operation. Moreover, it is noteworthy that boundary-layers at the upper and the lower side of the model significantly thickens downstream of the normal shock.

Under unstart mode (Fig. 1.15(c)), the supersonic flow structures (oblique and normal shockwaves) disappear and the flow appears considerably chaotic and fluctuating. This is because the shockwave structures at the inlet are dis-

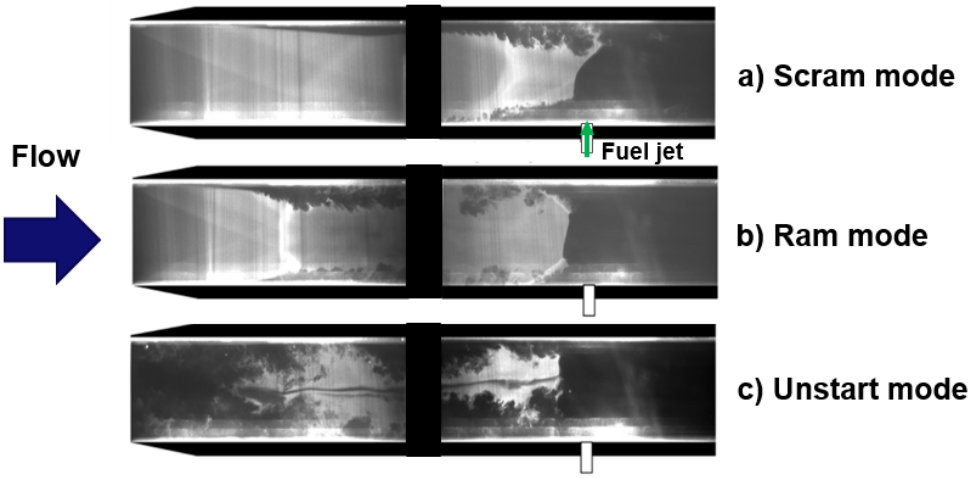

Fig. 1.15 (a) Scramjet mode, (b) ramjet mode, and (c) unstarted mode for an inlet of a dual-mode scramjet [12]

gorged out of the inlet, forming a strong shock system upstream of the inlet to turn the whole internal flow subsonic immediately. Under this operational mode, net thrust generation is significantly reduced owing to the reduced thrust and the increased spillage drag from the unstart shock, possibly leading to fatal failures. Therefore, inlet unstart mode must be avoided to achieve stable and fuel-efficient supersonic/hypersonic cruise flights.

However, a great number of flow parameters and phenomena affect the process of inlet unstart, making it difficult to predict and comprehend: detailed flow structures vary not only from different geometries (different shockwave structures) but also from different operating conditions (Mach number, angle of attack, etc.). Despite these difficulties, previous studies have found that some of the major causes of inlet unstart are backpressure rise/flow separation [14, 15, 85, 101, 119–121, 124, 125, 127, 129, 140], excessive fuel injection [12, 16, 105, 106, 117] and burning rates [115, 116], and their possible combina-

tions [17, 109]. In this regard, Section 1.2 presented one of the most important supersonic flow characteristics, flow choking which can lead to inlet unstart: area changes, skin friction effect, or heat transfer could lead to a decrease in Mach number to unity. When the internal flow in ramjets or scramjets is prematurely choked, it is highly likely to suffer from inlet unstart. In other words, inlet unstart is a transient phenomenon that could be triggered by flow choking. The previous simplified analysis in Section 1.2.1 (Eq. (1.7)) shows the parameters for the local choked mass flow rate: choked mass decreases with lower stagnation pressures (P_0), smaller effective areas (A^*), and higher stagnation temperatures (T_0). In supersonic and hypersonic flows, some of the primary flow phenomena that affect the aforementioned parameters are summarized below.

- Stagnation pressure: shockwave, skin friction, and mixing
- Effective area: boundary-layer growth, and separation
- Total temperature: combustion reaction, and wall heat transfer

Therefore, the local choked mass flow rate can change significantly depending on the structure and the conditions of the internal flow.

Meanwhile, in subsonic flows, pressure information from the choked throat travels upstream to reduce the incoming flow rate once the flow is choked. However, because the pressure information does not travel upstream in super- and hypersonic flows, the incoming (captured) mass flow rate can locally exceed the choked flow rate, or maximum allowable mass flow rate. Since this maximum flow rate through the passage is already determined by upstream conditions and

the flow structure, the resultant difference between the maximum and the incoming is accumulated near the choking point, forming a high-pressure region. This high-pressure region turns the flow downstream of the choking point to subsonic and promotes boundary-layer to grow. As a result, the choked flow rate even further decreases leading to an expansion of the high-pressure region. This is continued until the mass flow rates of the incoming and the local choked flow rate are balanced. If it is continued, another shockwave system is formed to compensate for the pressure difference, commonly referred to as "unstart shockwave". This unstart shock system travels upstream until the mass imbalance is resolved due to the continued growth of the high-pressure region; losses and pressure rise from unstart shock also substantially decrease the local choked flow rate. When the unstart shock reaches the inlet, it could be disgorged out of the inlet to form a strong shock system upstream of the inlet, turning downstream flow to subsonic. This induces spillages that could be highly unsteady which could result in an unsteady flow called "inlet buzz" [10, 89, 138, 139, 141, 142]. Therefore, thrust generation is reduced from the decreased oxidizer rate and abnormal combustor operations, meanwhile, drag also increases from the spillages through the unstart shock near the inlet [93, 95, 133, 135]. This whole transient flow process of supersonic internal flow to subsonic is often called "unstarting flow" and the resultant subsonic flow "unstarted flow" as opposed to "started flow". Also, it is noteworthy that fuel injections could induce additional shock losses (decreased stagnation pressure), directly add to the incoming rate, and incur combustion reaction downstream (elevated total temperature), making it one of the major causes of flow choking [17, 105].

Despite the technical challenges, previous studies have tried various methods and triggers to mimic inlet unstart. In addition, since providing realistic operating conditions for the period of the whole inlet unstart process is costly, studies

are conducted under so-called "cold" conditions [10, 89, 138, 139, 141, 142]. The term "cold" condition refers to non-reacting conditions that have significantly lower total temperature than a model aims for (e.g., cruise altitude and Mach number), possibly matching for Ma only to that from the target condition. This practice is sometimes preferred because i) it is not as costly as high-enthalpy experiments, ii) easier to consistently trigger inlet unstart in some ways (e.g., less flow fluctuation due to combustion), and while iii) still containing some of the major features of realistic unstarting and unstarted flows. Although those cold-flow experiments show varying unstart completion time, from a few tens of milliseconds to even a few hundreds of milliseconds, the unstarting and unstarted flows displayed somewhat similar behavior compared to those under the real operating conditions, which can still provide the valuable physics to comprehend the mechanism of inlet unstart [17].

1.3.1 Mechanical blockages

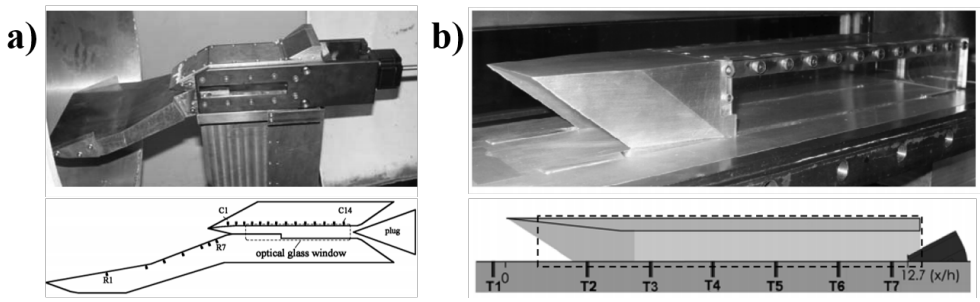

Fig. 1.16 (a) Mechanical plug (left) [13], and (b) movable flap (right) for cold unstart studies [14]

Under cold flow conditions, one of the popular methods to incur inlet unstart

is using flow blockages, commonly as a movable flap [14, 15, 85, 127, 134, 136, 140] or a plug (throttle) [13, 87, 89, 90, 110, 124, 125, 129, 138, 139] to abruptly reduce the effective area for simulating backpressure rise and flow choking at the combustor. In other words, mechanical blockages are preferred in cold flows with inlet-isolator configurations to mimic the interaction with the combustor. As a consequence, the internal flow suffers from an immediate mass imbalance leading to inlet unstart.

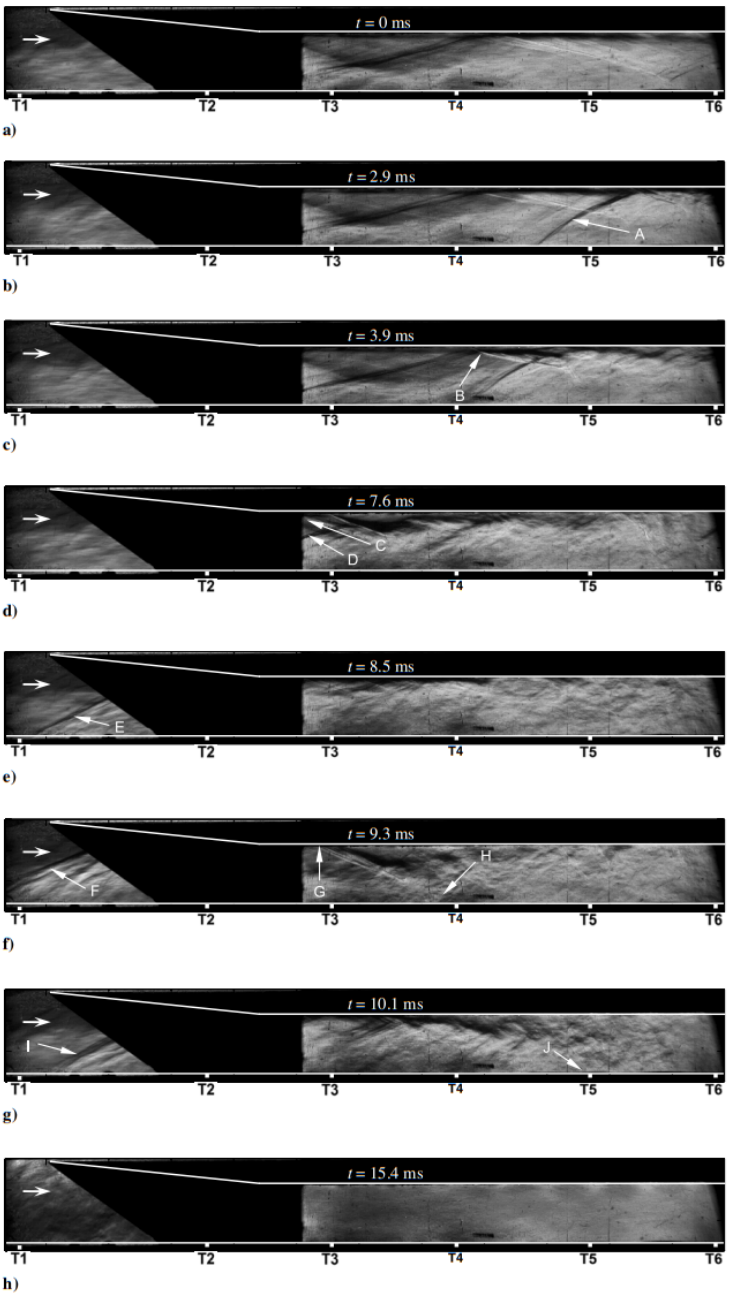

Fig. 1.17 Time-sequential schlieren images for unstarting flow with a flap under cold conditions [15]

1.3.2 Mass addition

An additional stream (most commonly as a non-reacting jet injection) can also be used for triggering inlet unstart [12, 17, 31, 97]. Under such configurations, the additional stream not only increases the total flow rate but also often decreases the local choked flow rate from the injection.

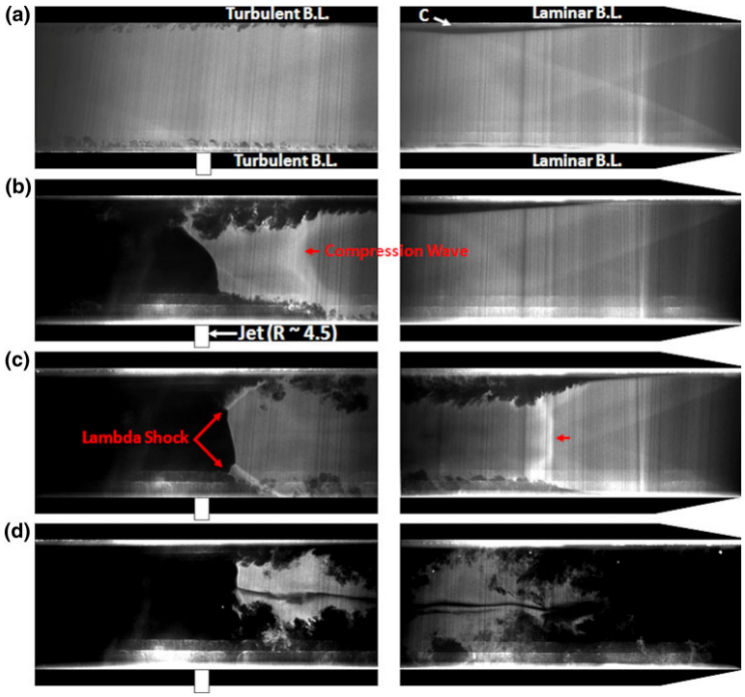

Fig. 1.18 Time-sequential schlieren images for mass-induced unstarting flow [16]

1.3.3 Combustion

A more realistic trigger for inlet unstart is to induce combustion reactions under high-enthalpy conditions [17, 106–109, 115–117, 128, 135]. Under the com-

busting environment, a direct mass addition from the fuel, fuel-air mixings, and heat release from the reaction all act to decrease the local choked flow rate, resulting in being highly susceptible to inlet unstart. Although liquid fuels have a variety of advantages over gaseous ones, liquid fuels usually require longer residence (flow) times in the passage from droplet evaporation to subsequent combustion reactions, however, which are often too long for ground-based test facilities to simulate. Instead, gaseous fuels, including hydrogen and ethylene, are commonly selected for injections since their ignition delays are fast enough to complete the combustion processes in typical geometries.

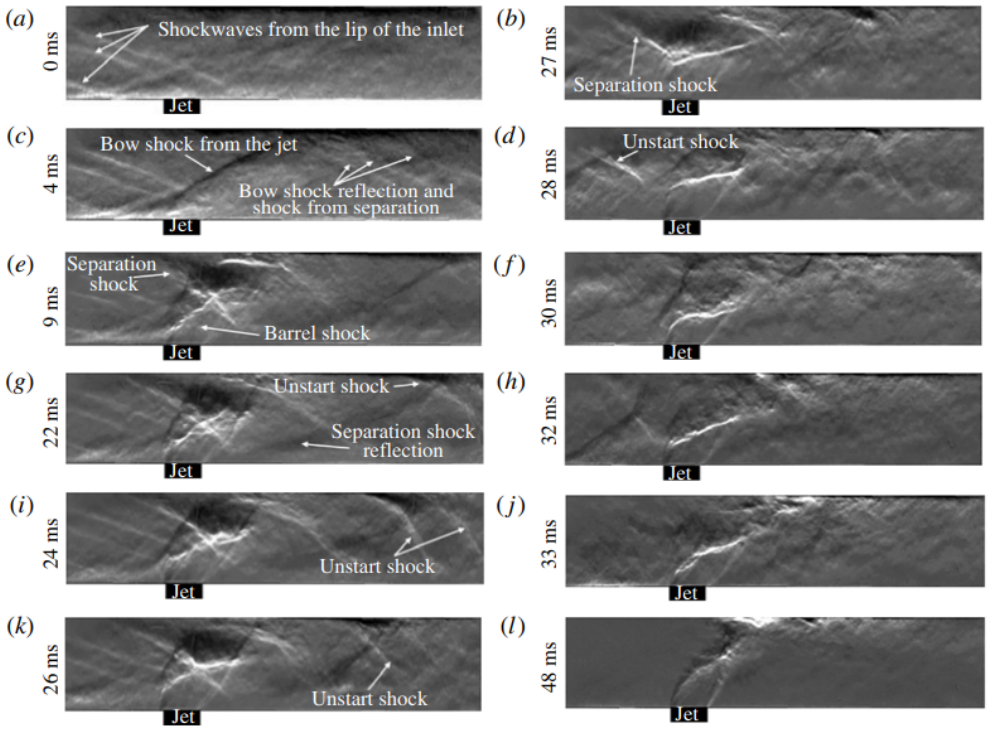

Fig. 1.19 Time-sequential schlieren images for thermal-choking-induced unstarting flow near the jet [17]

1.4 Flow Control Strategies in High-speed Flows

As presented in the previous sections, inlet unstart is an abrupt and catastrophic phenomenon that could disable net thrust generation within tens of milliseconds [14, 15, 85, 127, 134, 136, 140]. Moreover, the unstarted inlet must go through a "re-start process" to recover the performance requiring extra controls and time, which is difficult to be executed once unstarted due to the unsteady nature of unstarted flows [67, 95, 96, 100]. Fuel injection rate is one of the most important operation parameters not only for a higher vehicle performance but also for inlet unstart: the higher the fuel injection rate is, the higher the chance of flow choking will be since the local choked flow rate is significantly decreased. However, the fueling rate must be sufficiently high to generate large enough to overcome the vehicle drag and should be even higher especially in accelerating or ascending stages. In other words, it is inevitable for ramjets/scramjets to operate near the threshold of inlet unstart. If the threshold of inlet unstart can be accurately predicted, one can simply avoid this problem by carefully controlling the operation parameters such as the fuel injection rate. However, an accurate representation of the inlet unstart threshold is practically infeasible. This is not only because a large number of parameters, including flight Mach number, flight altitude, Angle of Attack (AoA), combustion (flame) dynamics, fueling rate, and even freestream turbulence levels, affect the dynamics of inlet unstart [6, 67, 74, 93, 95, 96, 100, 103, 118], but also the threshold and the subsequent flow processes can be highly dependent on the internal geometries: to author's knowledge, there is no single correlation developed to associate the parameters and geometry altogether. Moreover, even a test facility's characteristics could affect the fidelity of the experimental results, for example, due to high wet steam and carbon dioxide content from ground-based vitiated heater

wind tunnel operations, flame dynamics could be changed markedly [37]. On top of the fact the threshold cannot be accurately predicted, there must be a reliable and agreeable margin to inlet unstart, which would inevitably degrade the engine performance. Alternatively, some flow control devices could offer reduced or no margins to inlet unstart by mitigating the mass imbalance from flow choking.

In supersonic internal flows, any disturbances to the core flow would induce redundant shockwaves, resulting in increased losses. Therefore, flow control strategies in such flows should limit the disturbances to the subsonic portion of boundary-layers. The most common categorization of flow controls is passive or active: Active control strategies can choose when and/or where to execute the control whereas not for passive ones. Another categorization can be made by whether control involves mass transfers or not. Accordingly, four different types of controls are explained below.

1.4.1 Passive without Mass Transfer

Since inlet unstart is triggered by the mass imbalance between the choked (maximum) flow rate and the incoming flow rate, control strategies without mass transfer must increase the local choked flow rate to control inlet unstart. This can be achieved by elevated total pressures, enlarged effective areas, and lower total temperatures, as Eq. (1.7) implies. However, lower total temperatures may not be preferable since it directly leads to a reduced cycle efficiency. Therefore, this type of flow control device commonly aims for higher total pressures or larger effective areas in the passage. For the formal type of devices, the most accessible way is to alter the flow's shockwave/boundary-layer interaction (SBLI) [143].

Perforated plates or porous media are often used near strong SBLI or boundary-layer separation points to reduce the extra losses, which could lead to increased total pressure of the flow.

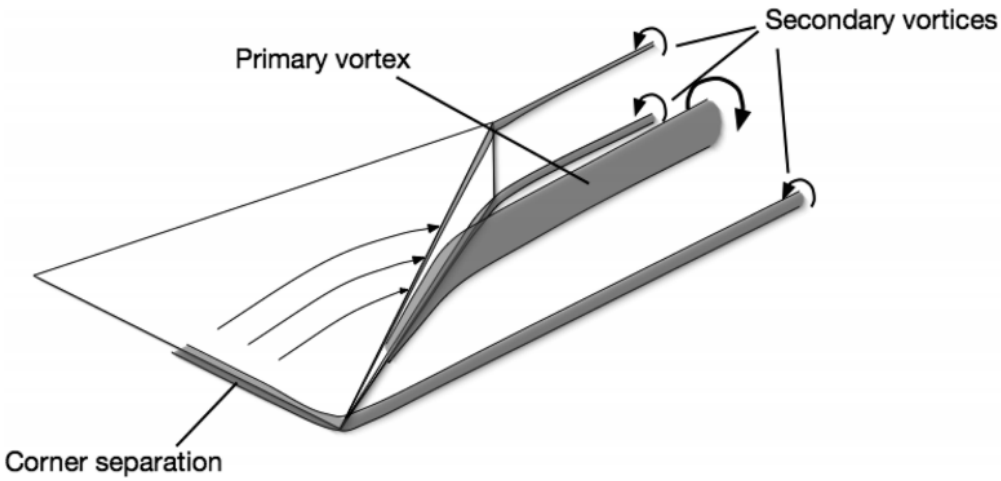

Fig. 1.20 A schematic of a micro vortex generator (MVG) [18]

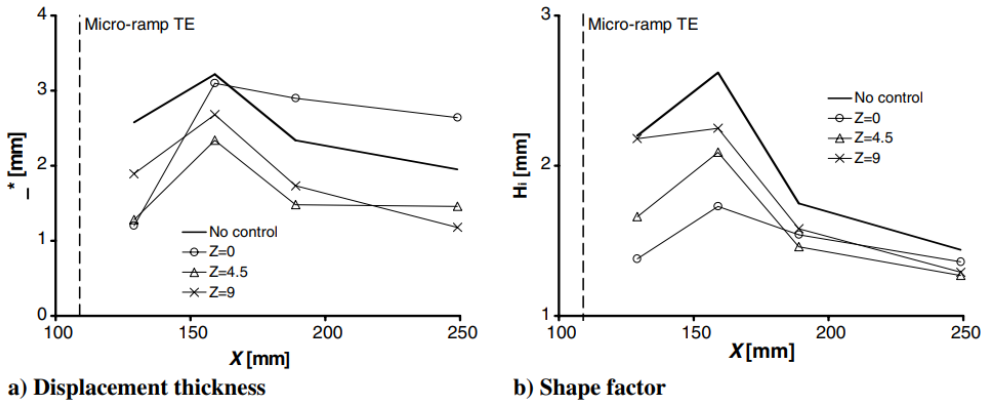

Fig. 1.21 Boundary-layer characteristic control by MVG [18]

Micro-ramps (MR) [18, 144] and micro vortex generators (MVG) [145–151] are the most popularly used for the latter kind because the flow disturbances are

limited to the subsonic portion of the flow (sub-boundary-layer). These devices induce stream-wise vortices that promote mixing between high-kinetic-energy flow (core) and low-kinetic-energy flow (near boundary-layer). By some expenses in the total pressure, flows at the low-speed region are accelerated leading to larger effective areas.

Although these devices can reduce flow separation and yield substantially better performances near the design point, the performance degrades and even deteriorates at off-design points since their operations are fixed and supposed to deal only with the on-design flow [18, 145].

1.4.2 Passive with Mass Transfer

The most popular method of this kind is bleeding [19, 91, 92, 152–177]. The term suction and bleeding are often used interchangeably as they share the quintessential mechanism, however, herein "suction" refers to an active strategy and "bleeding" to a passive one for clarity. Because it essentially extracts the mass from the internal flow by a few percent, the removed mass contributes to mitigating the mass imbalance from flow choking. Moreover, the wall-normal velocity component from the extraction could thin boundary-layers nearby, enlarging the effective area, especially near separated locations or throats [155, 169, 171, 176] For this reason, it is sometimes called "boundary-layer bleeding" to emphasize this boundary-layer suppression effect. However, the reduction of incoming mass directly reduces the oxidizer rate (and consequently reduced fueling rate) which could lead to reduced net thrust. Nevertheless, previous studies showed an appropriate use of bleeding could result in better performance [19, 92, 158, 161, 163, 169, 171, 174, 176, 177], better starting

characteristics [152–155, 157, 165], and larger unstart margins [164, 165, 170]. However, the larger the wall-normal velocity from the bleeding, the higher the disturbances will be to the flow, therefore, the configuration of the holes or the porosity for bleeding must be carefully chosen to minimize additional losses from the mass extraction and the disturbances [19, 91, 92, 159, 160, 175–177].

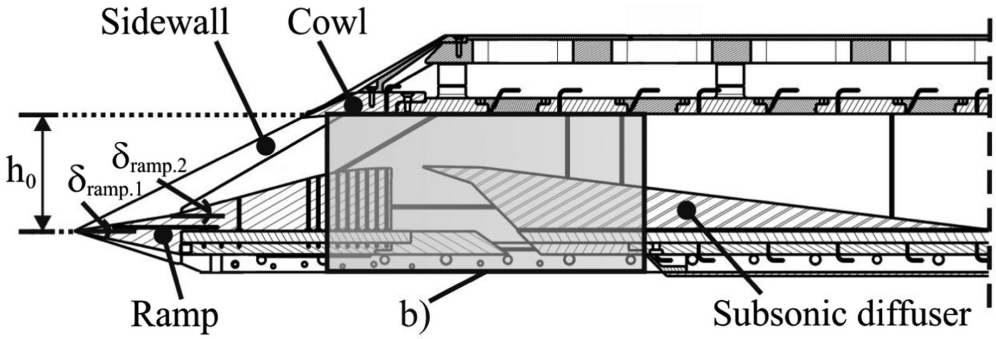

a) Sketch of inlet model

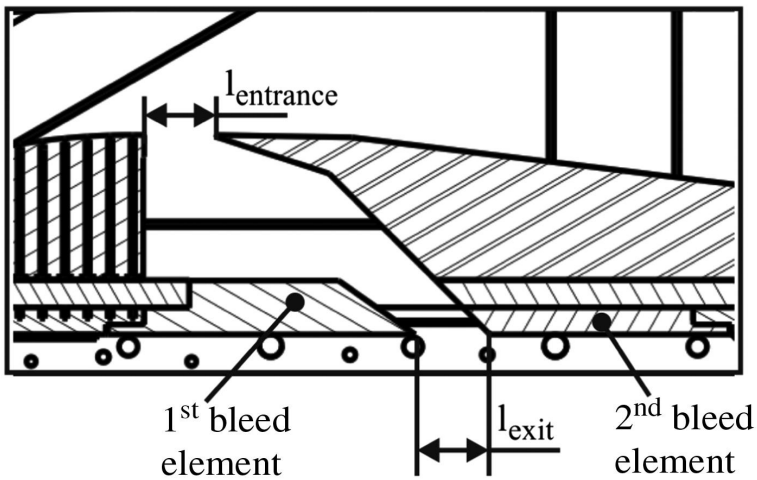

b) Inlet model with boundary-layer bleed configuration 16/16

Fig. 1.22 (a) An example sketch of inlet model and (b) boundary-layer bleeding configuration [19]

1.4.3 Active without Mass Transfer

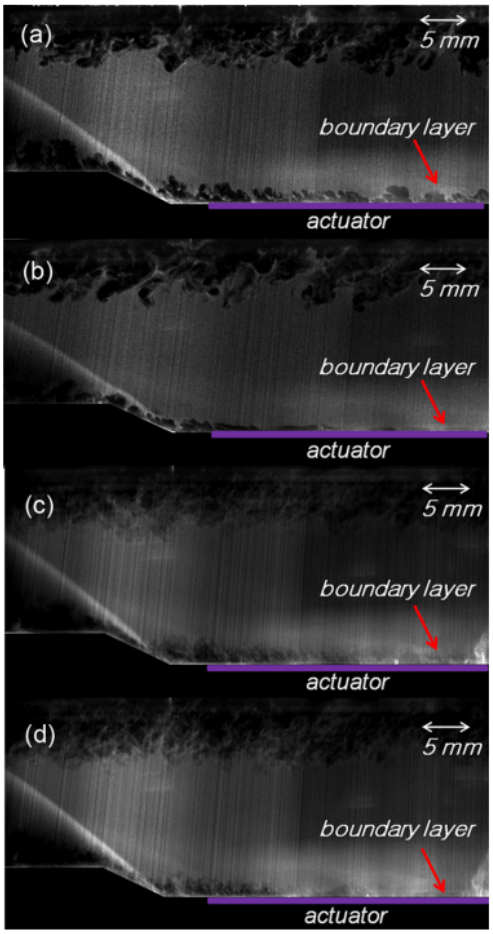

Fig. 1.23 Instantaneous CO2 Rayleigh scattering images (a) plasma-off case, (b) plasma-on case, averaged images, (c) plasma-off case, and (d) plasma on case. [20]

Similar to the passive ones without mass transfer (MRs and MVGs), this type of control devices often utilize vortex structures to boost mixing between low- and high-kinetic energy streams. A dielectric barrier discharge (DBD) actuators are exactly one of the kind, which can suppress boundary-layers

[16, 20, 178].

Although the DBD actuators showed an immediate boundary-layer suppression and subsequent inlet unstart control, the inlet unstart could not be completely suppressed but rather delayed by tens of milliseconds [16, 20, 178]. Furthermore, the surface of internal walls and electrodes degrade after activations, which significantly deteriorates the performance of the DBD actuators and the inlet. In addition, DBD actuators require a high-voltage source which also could be problematic in real applications.

1.4.4 Active with Mass Transfer

As introduced in Section 1.4.2, the most popular method is (boundary-layer) suction. This technique is often implemented with fast-activating valves to minimize actuation delays [97]. Due to this feature, compared to bleeding (passive mass extraction), active strategies can decide when and where to perform the control, broadening the operating envelope, and minimizing losses for well-operating modes.

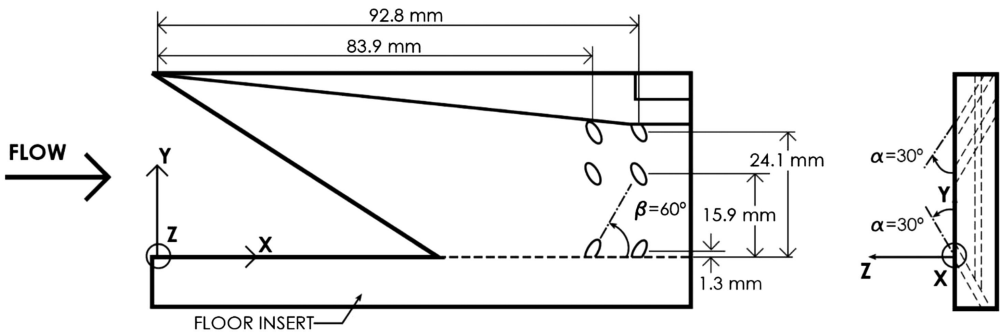

Fig. 1.24 Schematics of the inlet instrumented for VGJs with 60 deg skewed and 30 deg pitched injection ports. [21]

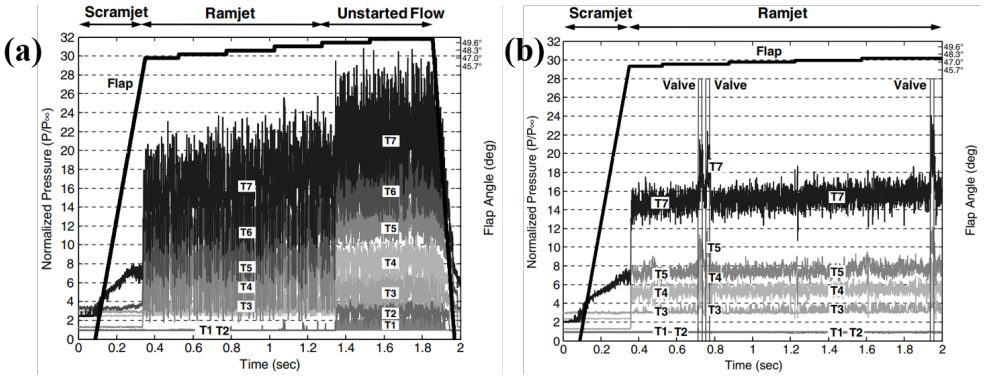

Fig. 1.25 Pressure measurement in (a) base case, and (b) Wheeler doublets (WD) + Vortex generator jets(VGJ). [21]

Another method is to inject mass as a jet to create secondary vortex structures, as fluidic vortex generators [21, 179]. Similar to passive vortex generators, inclined wall-near jets can create a pair of vortices that change boundary-layer characteristics to increase the local choked flow rate. Recently [21] demonstrated inlet unstart could be completely avoided via using a combination of passive and activate vortex generator jets.

1.5 Motivation and Overview of the Study

Inlet unstart is an abnormal and fatal failure mode and its onset of occurrence and subsequent processes are not well understood yet. Due to its highly non-linear nature near the onset, accurately predicting inlet unstart is still challenging. However, a ramjet/scramjet must operate near the onset of inlet unstart for the maximum performance which necessitates active flow control strategies for suppressing/delaying inlet unstart.

Therefore, the aim of this work is i) to provide better understandings of inlet unstart under various freestream conditions, and ii) to examine the effectiveness of boundary-layer suction control of unstarting and unstarted flows in super- and hypersonic air-breathing vehicles. A simplified model of a dual-mode scramjet engine is used. Two categorically different sets of experiments are performed, namely low-enthalpy conditions and high-enthalpy conditions. The first set, low-enthalpy condition, is to investigate the flow characteristics of cold (non-combusting) unstarting and unstarted flows and the effectiveness of boundary-layer suction control under these circumstances. The second set of experiments under high-enthalpy condition is for simulating more realistic flow conditions to incur inlet unstart: fuel injection, combustion, and thermal choking.

Chapter 2

Modeling of Boundary-layer Suction

Boundary-layer suction is an active flow control strategy that extracts a small portion of the low-speed region to enlarge the effective area of channel flow. In this section, typical supersonic channel flow, representing a scramjet isolator, is modeled as two-dimensional compressible laminar flows to estimate the performance of the suction control. Whilst maintaining the important physical features of the compressible internal flows, such modelings can offer useful information including the change of choking mass flow rate, and the characteristic time-scales of suction activation.

2.1 Modeling Overview

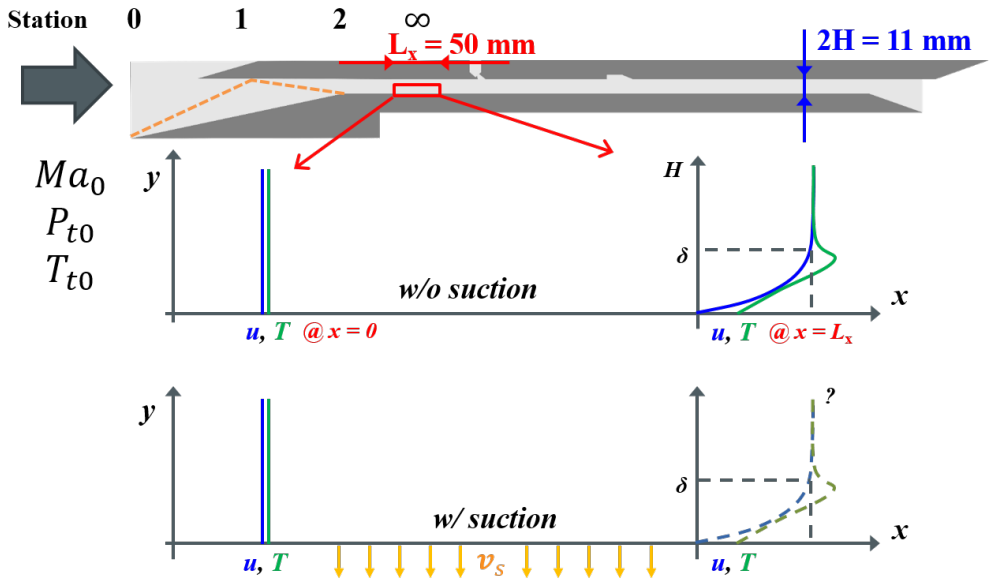

Fig. 2.1 A schematic of boundary-layer suction modeling

Boundary-layer suction is often applied either/both at the inlet and the isolator to thin the boundary-layer. When suction is utilized at the inlet, thinner boundary-layers can reduce the degree of flow separation near shockwave impingement points which can result in better performance of the inlet. On the other hand, boundary-layer suction at the isolator is primarily used to increase the choking flow rate via thinner boundary-layers which leads to a lower risk of inlet unstart. In the current section, a typical isolator flow is modeled as two-dimensional compressible laminar flow for the half of the channel (isolator). To quantitatively investigate the performance of suction, compressible laminar flow is directly solved via a compressible form of boundary-layer equations, similar to its incompressible counterpart, the Blasius equation. Assuming clean (uniform) velocity/temperature profiles at the inlet, the development of compressible lam-

inar boundary-layer is solved with and without wall-normal velocity at the wall which is from boundary-layer suction. The modeled stream-wise length of suction (L_x in Fig. 2.1) is 50 mm and the half channel height is 5.5 mm (H in Fig. 2.1). It is assumed that the wall-normal velocity due to suction (v_s) is uniformly distributed on the suction surface. To investigate the performance of suction at various conditions, wall temperature and suction rate are varied from 300 K to adiabatic, and 0.1% to 2.0%, respectively. Moreover, as introduced in section 1.1.2, one of the critical parameters that represent the level of shockwave/boundary-layer interaction is the confinement parameter [8], which is often defined as the ratio of the boundary-layer thickness to the half channel height (δ/H). Therefore, the confinement parameter is also varied from 0.2 to 0.4 for representing different operation conditions for boundary-layer suction

2.2 Mathematical Approach

2.2.1 Compressible laminar boundary-layer equations

The incompressible laminar boundary-layer equations are derived via order-of-magnitude analysis by Ludwig Prandtl and solved numerically by Blasius, therefore, also known as the Blasius equation. The compressible form of the laminar boundary-layer equation is developed by Y. Wang *et al.* for correcting compressible laminar-turbulent boundary-layer transition model [22].

Continuity equation (conservation of mass) in two-dimensional, compressible flow can be written as Eq. (2.1).

$$\frac{\partial \rho u}{\partial x} + \frac{\partial \rho v}{\partial y} = 0 \tag{2.1}$$

From order-of-magnitude analyses, x- (stream-wise) and y-direction (wall-normal) momentum equations are reduced as Eq. (2.2a) and Eq. (2.2b), respectively.

$$\rho u \frac{\partial u}{\partial x} + \rho v \frac{\partial u}{\partial y} = -\frac{\partial P}{\partial x} + \frac{\partial}{\partial y}\left(\mu \frac{\partial u}{\partial y}\right) \tag{2.2a}$$

$$\frac{\partial P}{\partial y} = 0 \tag{2.2b}$$

In a similar fashion, the energy equation can be reduced as follows.

$$\rho u \frac{\partial h}{\partial x} + \rho v \frac{\partial h}{\partial y} = \frac{\partial}{\partial y}\left(\kappa \frac{\partial T}{\partial y}\right) + u \frac{\partial P_\infty}{dx} + \mu \left(\frac{\partial u}{\partial y}\right)^2 \tag{2.3}$$

To close the equations, calorically perfect gas assumption (Eq. (2.4a)), ideal gas law (Eq. (2.4b)), and Sutherland's law (Eq. (2.4c)) are introduced,

$$p = \rho R T \tag{2.4a}$$

$$h = c_p T \tag{2.4b}$$

$$\frac{\mu}{\mu_{ref}} = \left(\frac{T}{T_{ref}}\right)^n \frac{T_{ref} + S}{T + S} \tag{2.4c}$$

where the constants for Sutherland's law for typical air are as follows (Eqs. (2.5a) to (2.5f)).

$$\mu_{ref} = 1.1789 \times 10^{-5} kg\ m^{-1}\ s^{-1} \tag{2.5a}$$

$$T_{ref} = 288\ K \tag{2.5b}$$

$$S = 110\ K \tag{2.5c}$$

$$n = 3/2 \tag{2.5d}$$

$$Pr = 0.74 \tag{2.5e}$$

$$\gamma = 1.4 \tag{2.5f}$$

For a similarity solution, coordinate transform is conducted via ξ and η, which are defined in Eq. (2.6a) and Eq. (2.6b), respectively,

$$\xi = \int_0^x \rho_\infty u_\infty \mu_\infty \, dx \tag{2.6a}$$

$$\eta = \frac{u_\infty}{\sqrt{\xi}} \int_0^y \rho \, dy \tag{2.6b}$$

where similarity functions for velocity and temperature are defined as f' and g, respectively as in Eqs. (2.7a) and (2.7b).

$$u(x,y) = u_\infty \; f^{'}(\eta) \tag{2.7a}$$

$$T(x,y) = T_\infty \; g(\eta) \tag{2.7b}$$

Rearranging Eqs. (2.1) to (2.3) using Eqs. (2.4) to (2.7) yields Eq. (2.8a) and Eq. (2.8b), where another function C is introduced as in Eq. (2.8c) for simplicity.

$$Cf''' + C'f'' + ff'' = 0 \tag{2.8a}$$

$$Cg'' + C'g' + Pr \cdot fg' + C \cdot Pr(\gamma - 1)Ma^2 \left(f''\right)^2 \tag{2.8b}$$

$$C = \frac{\rho\mu}{\rho_\infty \mu_\infty} = \sqrt{g}\frac{(1 + S/T_\infty)}{g + S/T_\infty} \tag{2.8c}$$

To apply the wall-normal velocity induced from boundary-layer suction (v_s) as a boundary condition, a stream-function approach is adopted as in Eq. (2.9).

$$\frac{\partial \psi}{\partial y} = u(x,y) = u_\infty f'(\eta) \tag{2.9}$$

By the definition of two-dimensional stream function, wall-normal velocity component can be expressed as in Eq. (2.10).

$$v(x,y) = -\frac{\partial \psi}{\partial x} = \frac{1}{\sqrt{2\rho}}\xi^{-\frac{1}{2}}\rho_\infty u_\infty \mu_\infty \ + \ \frac{\sqrt{2\xi}}{\rho} f' \frac{\partial \eta}{\partial x} \tag{2.10}$$

Substituting y with 0 to get the wall-normal velocity at the wall results in Eq. (2.11).

$$v_s = v(x,0) = -\frac{\partial \psi}{\partial x}\bigg|_{y=0} = -\frac{\sqrt{\rho_\infty u_\infty \mu_\infty}}{\sqrt{2x}\rho} f(0) \tag{2.11}$$

Rearranging Eq. (2.11) in terms of $f(0)$ yields Eq. (2.12). This shows $f(0)$ is 0 when there is no suction rate ($v_s = 0$), which is consistent with the incompressible Blasius equation.

$$f(0) = -\sqrt{2}\frac{\rho_w}{\rho_\infty}\frac{v_s}{u_\infty} {Re_x}^{\frac{1}{2}} \tag{2.12}$$

The equations Eqs. (2.8a) to (2.8c) are non-linear ordinary differential equations in terms of two functions, f and g. Since the equations are third-order in f, and second-order in g, respectively, five different boundary conditions are needed to solve the equation numerically. The boundary conditions are summarized in Table 2.1. The second column, "Adiabatic wall" represents the set of boundary conditions assuming adiabatic wall anywhere.

Firstly, $f(0)$ is determined from the suction rate as in Eq. (2.12), and $f'(0)$ is always zero due to non-slip condition at the wall. For an adiabatic wall, the no heat transfer at the wall is allowed leading to $g'(0) = 0$. Yet, it is impossible to get $f''(0)$ and $g(0)$ before solving the problem. Similarly, either $g(0)$ or $g'(0)$ is known in a priori from the conditions ($g(0)$ for constant wall temperature case, and $g'(0)$ for constant heat flux case), the other cannot be obtained in advance, allowing only three boundary conditions at the wall. Instead, two additional boundary conditions can be obtained from the definition of the freestream, which are $f'(\infty) = 1$ (definition of the freestream velocity, Eq. (2.7a)) and $g'(\infty) = 1$ (definition of the freestream temperature, Eq. (2.7b)), respectively. However, those two conditions are not known in advance as well before solving the equations. Therefore, a Newton-Raphson-type iterative solver using the shooting method is adopted to guess the unknown conditions at the wall until matching the freestream conditions.

Table 2.1 Boundary conditions for compressible laminar boundary-layer equations

Type	Adiabatic wall	Constant T_w	Constant $\dot{Q}_w$
$f(0)$	$f_{cn}(v_s)$	$f_{cn}(v_s)$	$f_{cn}(v_s)$
$f'(0)$	0	0	0
$f''(0)$	N/A[1]	N/A	N/A
$g(0)$	N/A	T_w/T_∞	N/A
$g'(0)$	0	N/A	$\frac{\dot{Q}_w}{\kappa T_\infty} / \frac{d\eta}{dx}\Big\vert_{y=0}$
$f'(\infty)$	1	1	1
$g(\infty)$	1	1	1

[1] N/A denotes "not available" in priori

2.2.2 Accelerated Runge-Kutta (ARK) methods

To numerically integrate the equations in Eqs. (2.8a) to (2.8c), Accelerate Runge-Kutta fourth(ARK4) scheme is used. Compared to the classical Runge-Kutta fourth scheme (RK4), ARK4 requires one less number of function evaluation (four with RK4, three with ARK3) while keeping the order of accuracy [23]. This is allowed by utilizing the results and constants from the previous calculations. For an arbitrary function u with the nth step of integration, the formulation of ARK4 method is as follows in Eq. (2.13).

$$y_{n+1} = c_0 y_n - c_{-0} y_{n-1} + c_1 k_1 + c_{-1} k_{-1} + \sum_{i=2}^{3} c_i (k_i - k_{-i}) \tag{2.13}$$

where

$$\begin{aligned} k_1 &= hf(y_n) & k_{-1} &= hf(y_{n-1}) \\ k_2 &= hf(y_n + a_1 k_1) & k_{-2} &= hf(y_{n-1} + a_1 k_{-1}) \\ k_3 &= hf(y_n + a_2 k_2) & k_{-3} &= hf(y_{n-1} + a_2 k_{-2}) \end{aligned} \tag{2.14}$$

Now it is clear that although ARK4 method requires larger computational storage to save the previous computation results (for k_{-1}, k_{-2}, and k_{-3}), the reduced number of function evaluations could result in faster calculations, hence got its name. There are three sets of available optimized parameters as summarized in Table 2.2. In the current study, Set 1 is used to integrate the compressible laminar boundary-layer equations. However, ARK method is not self-starting:

previous results are not available for the first integration. Therefore, the classical RK4 method is employed only for the first integration.

Table 2.2 Optimized parameter sets for ARK4 method [23]

Parameter	Set 1	Set 2	Set 3
c_0	1.0	$-4\frac{\sqrt{41}-11}{9+\sqrt{41}}$	$-4\frac{\sqrt{41}-11}{9+\sqrt{41}}$
c_{-0}	0.0	$-5\frac{\sqrt{41}-7}{9+\sqrt{41}}$	$-5\frac{\sqrt{41}-7}{9+\sqrt{41}}$
c_1	1.0176276732044952467496 35	$\frac{16}{3}\frac{6\sqrt{41}-1}{(9+\sqrt{41})^2}$	$\frac{16}{3}\frac{6\sqrt{41}-1}{(9+\sqrt{41})^2}$
c_{-1}	0.0176276732044952467496 3508	$\frac{4}{3}\frac{3\sqrt{41}-13}{(9+\sqrt{41})^2}$	$\frac{4}{3}\frac{3\sqrt{41}-13}{(9+\sqrt{41})^2}$
c_2	-0.1330037778097525280771293	0	$\frac{200}{3(9+\sqrt{41})^2}$
c_3	0.6153761046052572813274942	$\frac{400}{3(9+\sqrt{41})^2}$	$\frac{200}{3(9+\sqrt{41})^2}$
a_1	0.3588861139198819376595942	$\frac{9+\sqrt{41}}{40}$	$\frac{200}{3(9+\sqrt{41})^2}$
a_2	0.7546602348483596232355257	$\frac{9+\sqrt{41}}{20}$	$\frac{9+\sqrt{41}}{20}$

An example of boundary-layer profiles of velocity magnitude and temperature is plotted in Fig. 2.2 [22]. For incompressible laminar boundary-layers ($Ma = 0.2$ as dashed lines in Fig. 2.2), the profiles are identical to the results from Blasius equations. In a compressible regime, however, skin friction at the wall is greater resulting in a "fuller" velocity profile. Moreover, thermal (temperature) boundary-layer effect is significant, resulting in a considerably changing Mach number in the boundary-layer.

The boundary-layer suction effect can be simulated via Eq. (2.12) assuming a uniform distribution of suction across the device. However, since boundary-layer theory was originally developed for external flows, applying non-zero wall-normal velocity leads to profiles with a higher mass flow rate, which is not

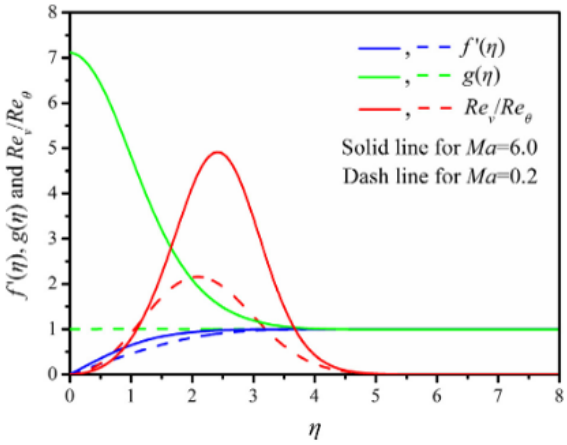

Fig. 2.2 Velocity and temperature boundary-layer profiles for incompressible (dashed line) and compressible flows (solid line) for adiabatic wall [22]

physical in internal flows. Therefore, the freestream Mach number is adjusted by an iterative method as in Fig. 2.3 until the mass flux balance is met; other freestream properties, including freestream static pressure and static temperature, are re-estimated using isentropic relations, assuming zero loss from the suction.

2.2.3 Boundary-layer suction performance parameters

Once the calculation of profiles of boundary-layer is completed, a few suction performance parameters are introduced and analyzed. Firstly, the formula for the suction flow rate of one-dimensional flow is modified for reflecting the velocity/temperature profile of the flow. The choking area of a small portion a flow, dA^*, can be expressed from Eq. (1.6) as in Eq. (2.15).

$$\frac{dA}{dA^*} = \frac{1}{Ma(\eta)} \frac{[1 + 0.2\, Ma(\eta)^2]^3}{1.728} \qquad for\ \gamma = 1.4 \tag{2.15}$$

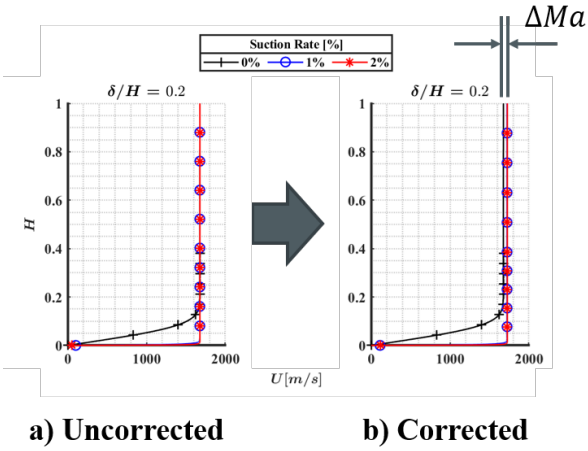

Fig. 2.3 An example of freestream correction for mass flux balance

Similarly, the choking mass flow rate in Eq. (1.7) is expressed in differential form as in Eq. (2.16).

$$d\dot{m}_{choked} = 0.6847 \frac{P_0(\eta)}{\sqrt{RT_0(\eta)}} dA^* \tag{2.16}$$

Integrating Eq. (2.16) from the wall ($\eta = 0$) to the freestream ($\eta = \infty$) gives an alternative formula for choking mass flow rate taking the spatial variation of the profiles into account.

$$\dot{m}_{choked} = \int_{\eta=0}^{\eta=\infty} 0.6847 \frac{P_0(\eta)}{\sqrt{RT_0(\eta)}} dA^* \tag{2.17}$$

Therefore, the change of the choking mass flow rate from suction can be defined as Eq. (2.18), where superscript $\circ$ represents the choking flow rate without suction at the same condition.

$$\Delta\, \dot{m}_{choked} = \frac{\dot{m}_{choked} - \dot{m}^{\circ}_{choked}}{\dot{m}^{\circ}_{choked}} \tag{2.18}$$

To investigate the change of mass-loading from boundary-layer suction, *CMR* in Eq. (1.8) is estimated and used for the analyses, where *CMR* in the current section is defined as in Eq. (2.19).

$$CMR = \frac{\dot{m}_{in}}{\dot{m}_{choked}} = \frac{\int_{\eta=0}^{\eta=\infty} \rho u \, dA}{\dot{m}_{choked}} \tag{2.19}$$

Similar to the choking flow rate, the variation of *CMR* can be defined as in Eq. (2.20), which represents the change of mass-loading of the flow due to 1) mass extraction and 2) choking mass increase from boundary-layer suction,

$$\Delta CMR = \frac{CMR}{CMR^{\circ}} = \frac{\dot{m}_{in}/\dot{m}_{choked}}{CMR^{\circ}} \tag{2.20}$$

where again superscript $\circ$ denotes the properties at non-suction conditions.

Moreover, ΔCMR_{Mass} is introduced as in Eq. (2.21) to separate the two effects and the suction, and only to consider the effect from mass extraction.

$$\Delta CMR_{Mass} = \frac{\dot{m}_{in}/\dot{m}^{\circ}_{choked}}{CMR^{\circ}} \tag{2.21}$$

Above two performance parameters, $\Delta\,\dot{m}_{choked}$ and ΔCMR, are quasi-steady-state parameters. To estimated the time-scale of the boundary-layer suction activation, the change of boundary-layer thicknesses is computed. Having known the wall-normal velocity at the wall (v_s), a ratio can be defined as below (Eq. (2.22),

$$\tau_s = \frac{\Delta\delta}{v_s} = \frac{\delta - \delta^{\circ}}{v_s} \tag{2.22}$$

which has a unit of time. A physical interpretation of Eq. (2.22) is the ratio of boundary-layer suppression via suction ($\Delta\delta$) to its suppression speed (v_s), which represents the amount of time needed for the suction activation to its full capacity.

2.2.4 Calculation conditions

Conditions for boundary-layer suction are selected from typical operating conditions of isolators summarized as in Table 2.3. The Mach number and the

total temperature at the inlet is assumed to be uniform at 2.75 and 2400 K, respectively. Four wall temperature boundary conditions are considered: adiabatic wall and constant temperature wall at 300, 500, and 1000 K. The confinement parameter, δ/H are varied from 0.2 to 0.4. Lastly, five different suction rates are taken into account to elucidate the performance of boundary-layer suction in terms of the suction rate. Via Newton-Raphson-type iterative solve with the shooting method, the tolerance is set to be 10^{-4}, that is, calculations are conducted until $|f'(\infty) - 1| < 10^{-4}$ and $|g(\infty) - 1| < 10^{-4}$ are met simultaneously. For the freestream (∞), $\eta = 8$ is selected assuming far enough from the wall. The thickness of the velocity boundary-layer is chosen as the vertical location at which velocity becomes 99.9% of the freestream value, i.e., $f'(\infty) = 0.999$.

Table 2.3 Calculation conditions for boundary-layer suction modeling

Parameter	Value
Ma	2.75
T_0, K	2400
T_w, K	($adiabatic$), 300, 500, 1000
δ / H	0.2, 0.3, 0.4
$Suction$, %	0.1, 0.25, 0.5, 1.0, 1.5, 2.0

2.3 Results

2.3.1 Velocity/temperature profiles for non-suction cases

Normalized velocity (u/u_∞), temperature (T/T_∞), and Mach number profiles for non-suction cases are plotted for different confinement parameters for 0.2, 0.3, and 0.4 in Figs. 2.4 and 2.6, respectively. The four sub-figures in each plot are from different wall temperature boundary conditions: a) adiabatic wall, b) constant temperature wall at 300 K, c) constant temperature wall at 500 K, and d) constant temperature wall at 1000 K.

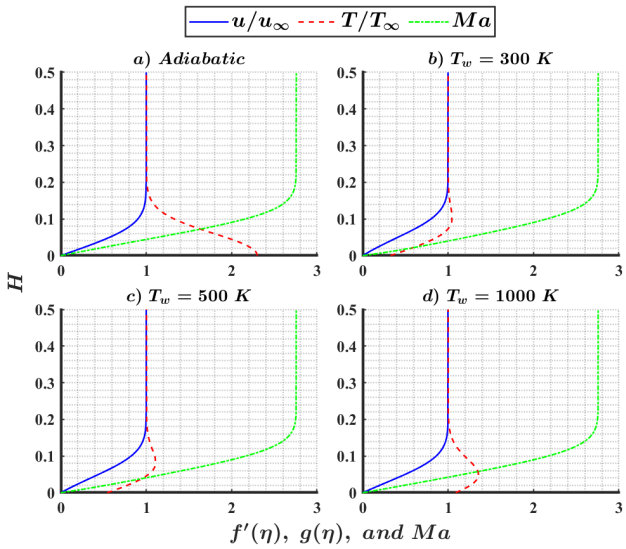

Fig. 2.4 Normalized Velocity (f'), temperature(g), and Mach number profile for different wall temperatures $\delta/H = 0.2$

Although the Mach number profiles are almost constant over the change of wall temperature changes, temperature profiles change significantly, resulting in slightly varying velocity profiles over different wall temperatures.

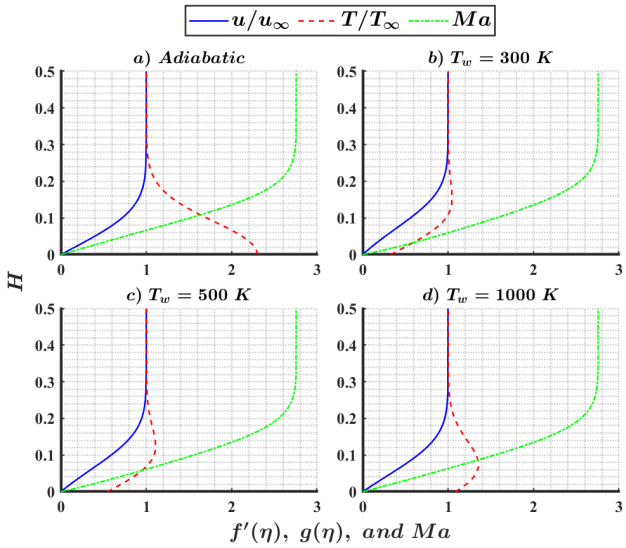

Fig. 2.5 Normalized Velocity (f'), temperature(g), and Mach number profile for different wall temperatures $\delta/H = 0.3$

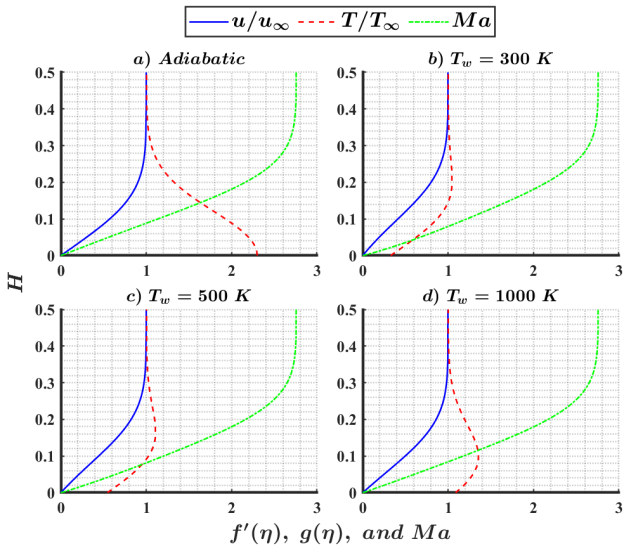

Fig. 2.6 Normalized velocity (f'), temperature(g), and Mach number profile for different wall temperatures $\delta/H = 0.4$

2.3.2 Velocity profiles for suction cases

Based on the non-suction profiles in Section 2.3.1, velocity boundary-layer profiles under suction rates of 0.1, 0.25, 0.5, 1.0, and 2.0 % are computed. Velocity profiles for non-suction and suction cases are plotted for different wall temperature conditions are plotted in Figs. 2.7 to 2.10. The sub-figures represent different confinement parameters, a) $\delta/H = 0.2$, b) $\delta/H = 0.3$, and $\delta/H = 0.4$, respectively.

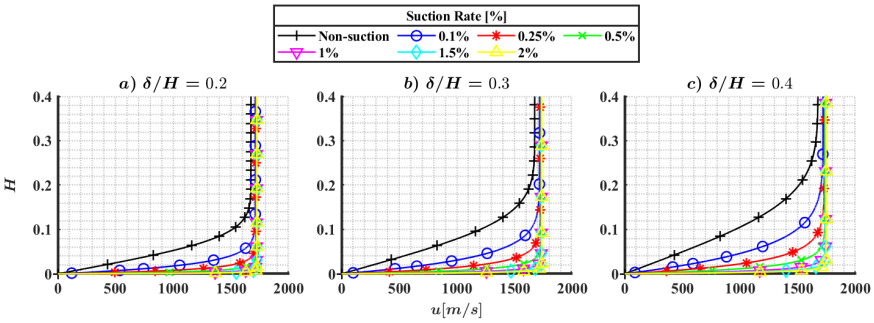

Fig. 2.7 Velocity profiles at different confinement parameters and suction rates (adiabatic wall)

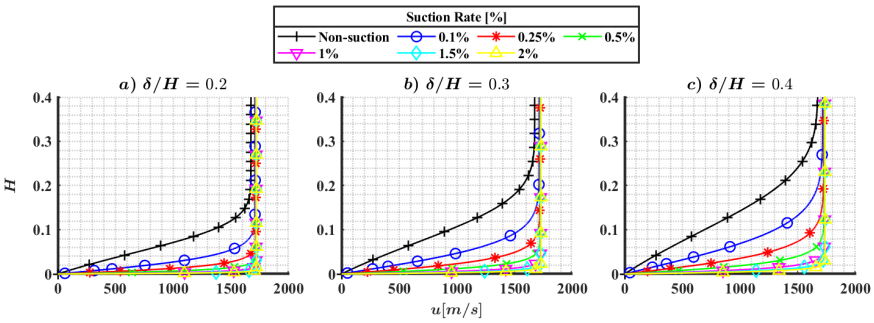

Fig. 2.8 Velocity profiles at different confinement parameters and suction rates ($T_{wall} = 300\ K$)

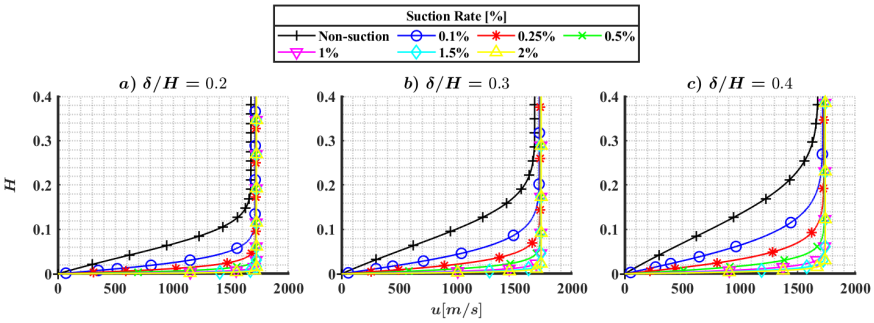

Fig. 2.9 Velocity profiles at different confinement parameters and suction rates ($T_{wall} = 500\ K$)

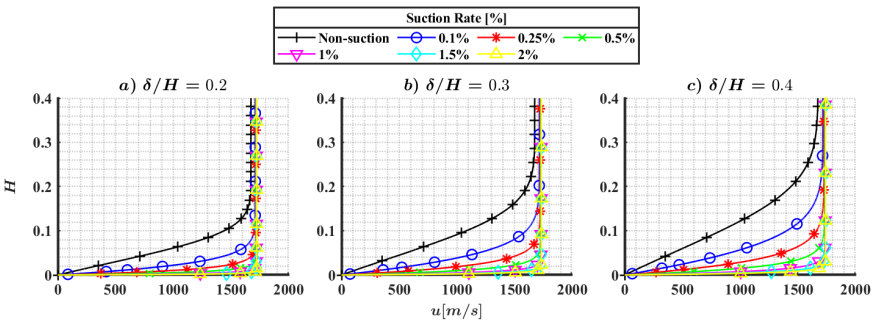

Fig. 2.10 Velocity profiles at different confinement parameters and suction rates ($T_{wall} = 1000\ K$)

As the suction rate increases, velocity profiles become steeper at the wall, resulting in "fuller" profiles. However, no significant effect on wall temperature boundary conditions is observed.

2.3.3 Temperature profiles for suction cases

Similar in Section 2.3.2, temperature profiles at different confinement parameters and wall temperature conditions are plotted in Figs. 2.11 to 2.14.

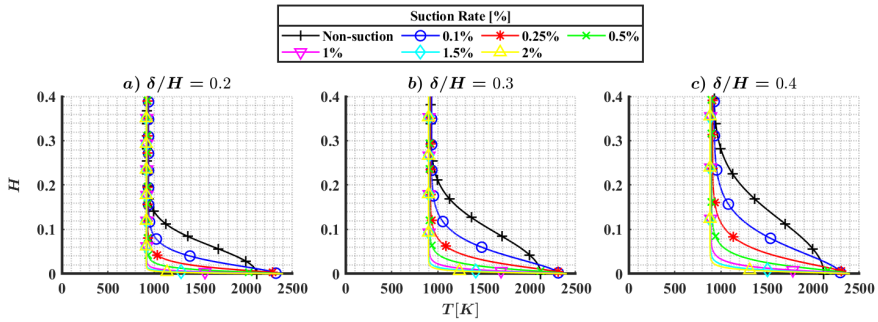

Fig. 2.11 Temperature profiles at different confinement parameters and suction rates (adiabatic wall)

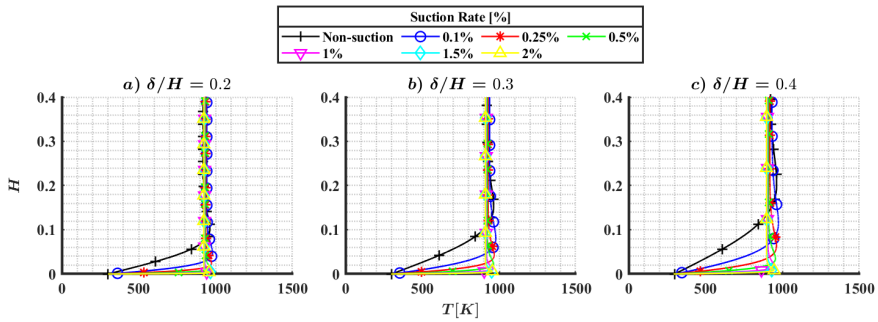

Fig. 2.12 Temperature profiles at different confinement parameters and suction rates ($T_{wall} = 300\ K$)

In contrast with the velocity profiles which were affected little by wall temperature changes, temperature profiles in the boundary-layer are directly affected by wall temperature conditions, leading to significant changes.

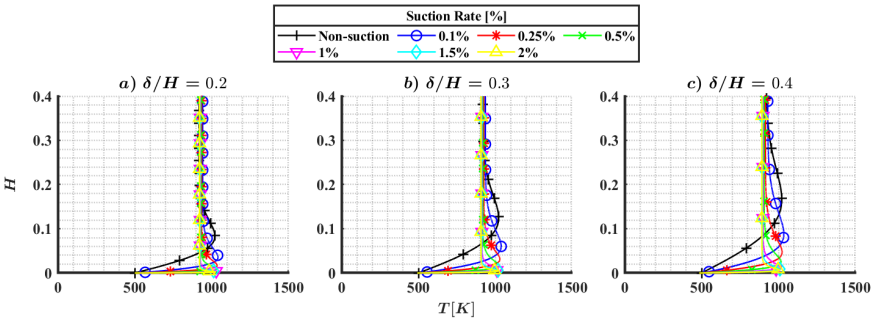

Fig. 2.13 Temperature profiles at different confinement parameters and suction rates ($T_{wall} = 500\ K$)

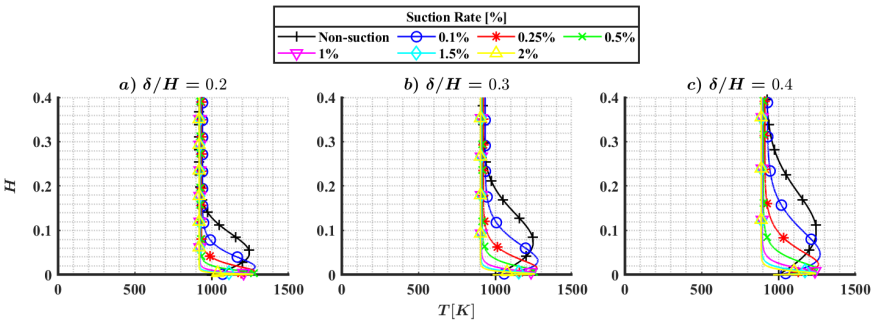

Fig. 2.14 Temperature profiles at different confinement parameters and suction rates ($T_{wall} = 1000\ K$)

2.3.4 Boundary-layer suction performance analysis

To quantitatively investigate the performance of boundary-layer suction, performance parameters defined in Section 2.2.2 are introduced for choking mass flow rate (Eq. (2.18)), CMR (Eqs. (2.20) and (2.21)), and characteristic time-scale (Eq. (2.22)).

Firstly, the change of choking mass flow rate is analyzed as in Fig. 2.15. Although the degree of the choking mass increase differs by different confinement parameters, the increase of choking mass flow rate becomes maximum at around 1 % of the suction rate, and even slightly decreasing for $\delta/H = 0.2$ and $\delta/H = 0.3$. The maximum choking mass flow rate increase is about 9 %, 16 %, and 23 % for $\delta/H = 0.2$, $\delta/H = 0.3$, and $\delta/H = 0.4$, respectively. The variation of wall temperatures does not significantly impact the choking mass flow rate, leading to variations within 10 % at the same suction rate.

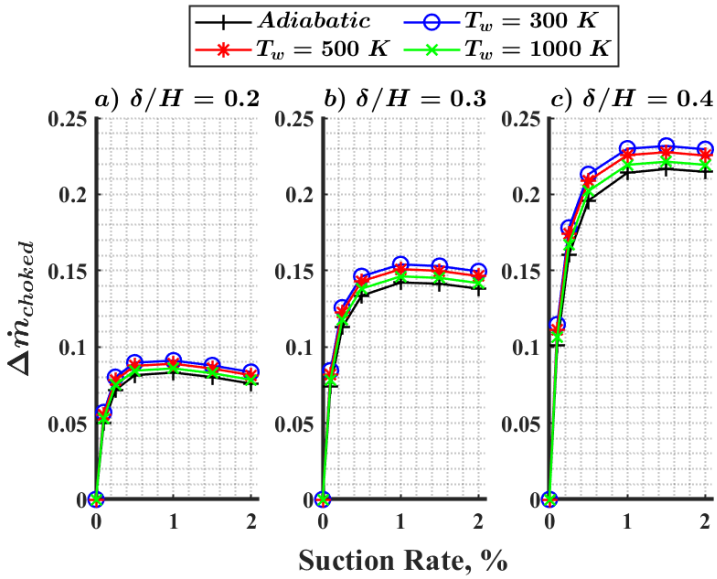

Fig. 2.15 The change of choking mass flow rate via boundary-layer suction

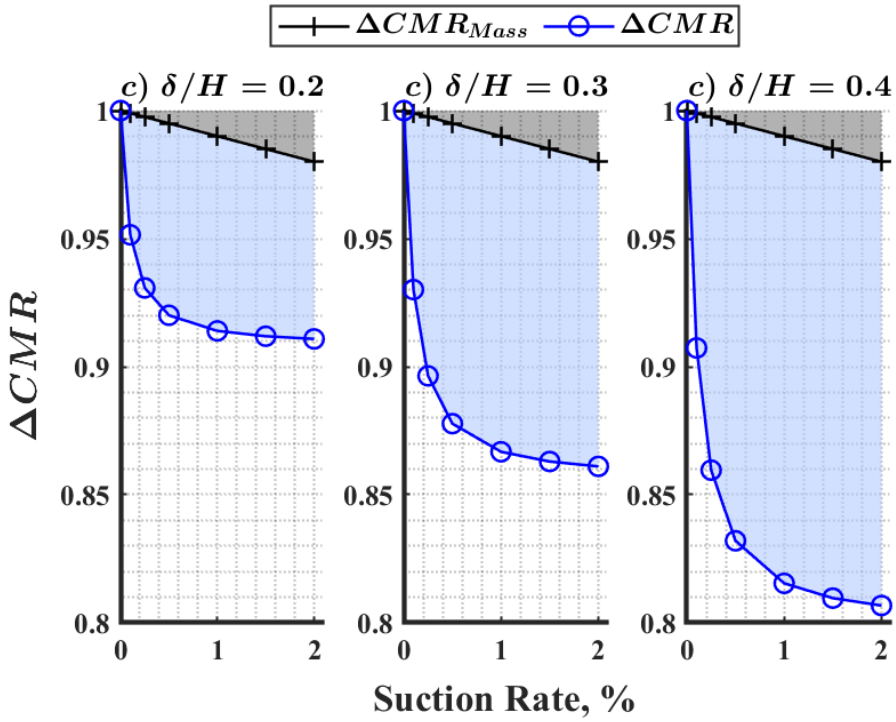

Fig. 2.16 Change of CMR via boundary-layer suction under adiabatic wall condition

Also, CMR is estimated for different conditions to investigate the change of mass-loading of the flow at different suction rates as in Fig. 2.16. Only adiabatic wall case is presented here since other wall temperature conditions show similar trends. The gray-shaded area in each sub-figure represents the portion of CMR decrease only due to the decreased flow rate from the suction. On the other hand, the blue-shaded area indicates the CMR decrease due to the increase of choking flow rate attributable to the re-distribution of flow momentum (different velocity/temperature profiles). In Fig. 2.16, the blue-shaded area is always larger than the gray-shaded area; the decrease of CMR (and the increase of the

choking mass flow rate) is primarily due to the re-distribution of flow momentum. However, in spite of decreasing CMR at higher suction rates, the slope becomes less steep at again around 1 % of the suction rate. This implies that although the increase of choking flow rate accounts for more than 80 % of the decreased mass-loading, the decrease of CMR at suction rates higher than 1 % is more attributable to the direct mass extraction from the suction. This could suggest that suction rates larger than 1 % might not be efficient.

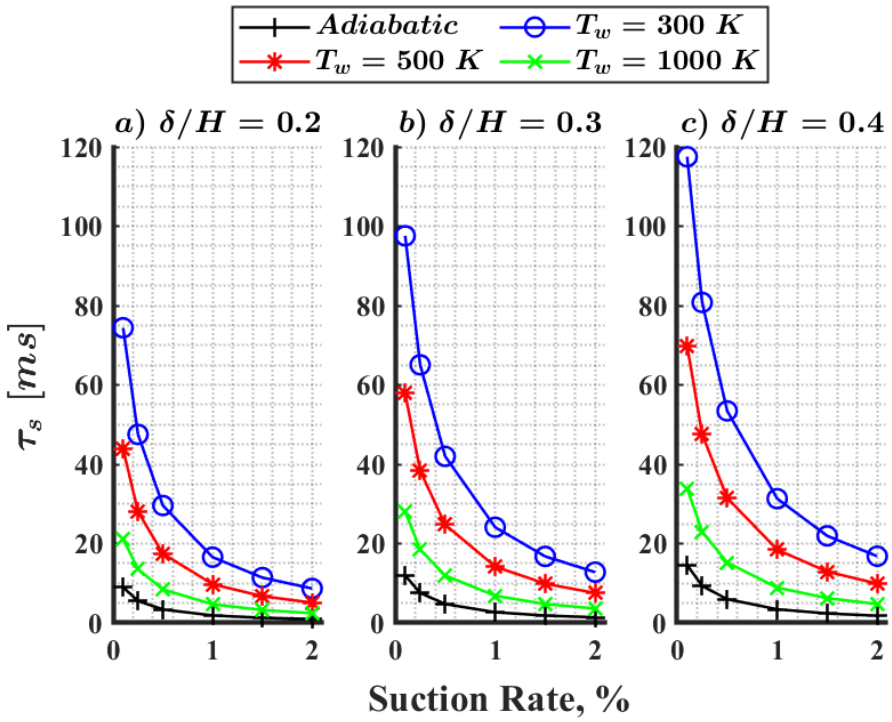

Fig. 2.17 Characteristic time-scales for boundary-layer suction

The characteristic time-scale for boundary-layer suction is estimated and plotted in Fig. 2.17. The characteristic time-scale is ranging from a few milliseconds to even more than a hundred milliseconds, primarily varying from different

suction rates and wall temperatures. In contrast to the previous performance parameters where wall temperature did not significantly affect, τ_s is considerably changing with different wall thermal conditions. This is attributable to the different density near the wall, resulting in different suction velocities (v_s) for the same amount of suction rate. In other words, since the density near the wall is the highest at $T_w = 300\ K$ case, suction velocity is the lowest, resulting in the longest time-scale.

2.4 Summary

Boundary-layer suction is modeled as compressible laminar flow in a two-dimensional constant area channel. Given with typical operating conditions of scramjet isolators, the internal flow is solved with different confinement parameters, wall thermal conditions, and suction rates. It was turned out that suction is capable of increasing choking mass flow rate (and decreasing mass-loading) more than 20 %, especially at higher confinement parameters. The mechanism under boundary-layer suction increasing the choking flow rate is mainly attributable to the re-distribution of the flow momentum, not from the direct mass extraction, whose effectiveness significantly decreases at suction rates higher than 1 %. Nevertheless, CMR keeps decreasing with higher suction rates. Wall thermal effect on choking flow rate and mass-loading were relatively insignificant. However, for the characteristic time-scale of suction execution, wall thermal condition plays a pivotal role, increasing the execution time more than five times than in adiabatic conditions. The characteristic time-scale ranges from a few milliseconds to more than a hundred milliseconds. For a typical suction rate (1 %), the time-scale was an order of few tens of milliseconds, which is a comparable time-scale for inlet unstart. This implies that inlet unstart should be sensed as early as possible and the boundary-layer suction should be activated and executed fast enough for controlling unstarting flows.

Chapter 3

Boundary-layer Suction Control in Low-Enthalpy Flows: Unstarting Flows

Boundary-layer suction control in low-enthalpy freestream flows, or namely "cold" flows is presented in this section. With a given test model, the threshold for mass-induced inlet unstart was carefully found by altering the jet injection rate. Then, the effectiveness of boundary-layer suction control is quantitatively evaluated in delaying or completely suppressing inlet unstart with different mass-loadings and suction trigger timings.

3.1 Experimental Configuration

3.1.1 Test Model

The test model used for this study is comprised of an inlet, a constant-area isolator, a combustor, and a divergent nozzle to simulate a whole flow passage of a typical scramjet as presented in Fig. 3.1. The inlet has a single ramp of 12° at the lower lip for a shockwave-compression. The cowl of the inlet (the leading of the upper wall) is recessed by 55 mm for examining unstarting flows. However, the cowl is further recessed by 55 mm (110 mm in total) for unstarted flows to provide a faster re-starting capability for simulating the inlet buzz phenomenon. The suction device for driving boundary-layer suction flows is located approximately 86 mm downstream of the cowl. At roughly 210 mm downstream of the cowl, there is a fuel jet nozzle that injects fuel at supersonic speed with 60° inclined to the freestream flow. A 3 mm-deep flame holder cavity is located at 100 mm downstream of the fuel jet which is followed by a divergent nozzle. Each sidewall has windows at the inlet and throughout the isolator to the combustor to enable optical access to the flow.

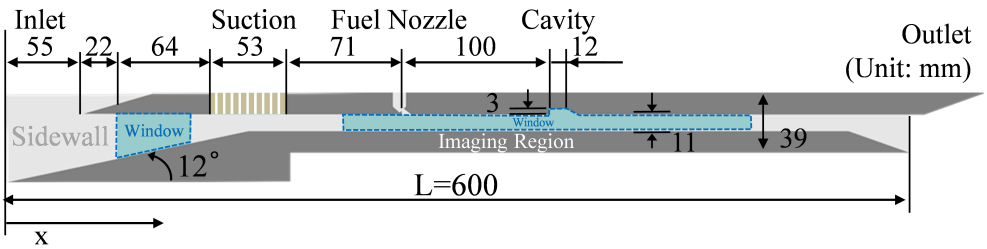

Fig. 3.1 Schematic of the model scramjet for low-enthalpy unstarting flows

A perforated plate shown in Fig. 3.2 is installed at the upper wall in the isolator. This plate has 78 holes of 0.8 mm in diameter (13 in the stream-wise

direction, 6 in the span-wise direction) and spaced equally by 4 mm. The distribution and the size and the hole are carefully chosen to meet the following requirements: minimized losses/disturbances to the flow and easy manufacturing.

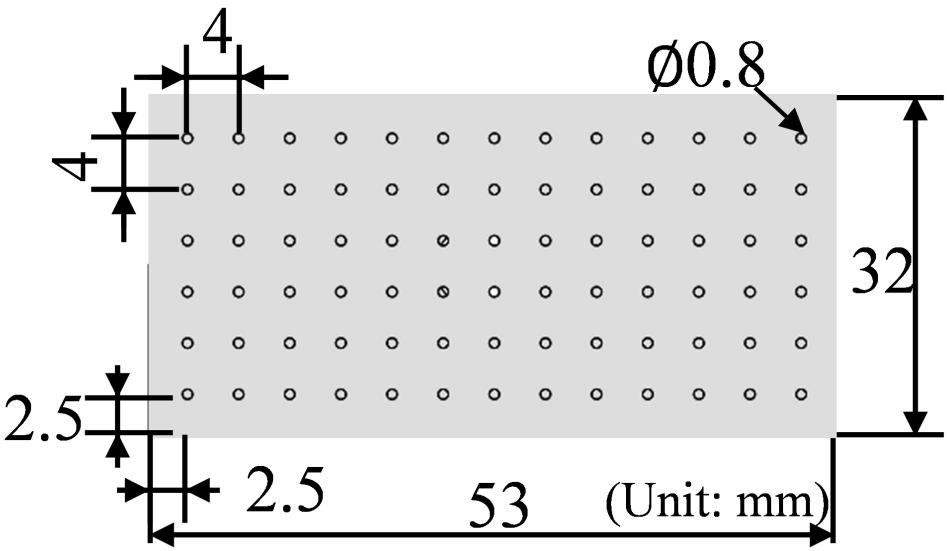

Fig. 3.2 Perforated plate for boundary-layer suction flow

3.1.2 Test rig and Instrumental Setups

A super- and hypersonic blown-down wind tunnel at the University of Notre Dame (Act-heated Combustion Test-rig 1, ACT-1) was used to conduct the experiments. To firstly test the control under low-enthalpy freestream flows, the arc-heater was deactivated and the total temperature of the tunnel flows was assumed to remain constant at room temperature (approximately 298 K) in this section. A mixture of 80 % nitrogen and 20 % carbon dioxide in volume was

supplied through a convergent-divergent (C/D) nozzle and a model scramjet was placed approximately 20 mm downstream of the nozzle exit at zero angle of attack. The diameter of the C/D nozzle used in this setup is 67.6 mm providing a uniform Mach 6 freestream core at the exit approximately 44 mm in diameter. The test section is connected to a vacuum chamber of 10 m^3 enabling a relatively long test period of up to one second. The test section was evacuated by a two-stage high-performance vacuum pump and the estimated average vacuum pressure was 20 Pa. Another small vacuum tank of 2.1 liters was placed inside the test section to drive suction flow from the model.

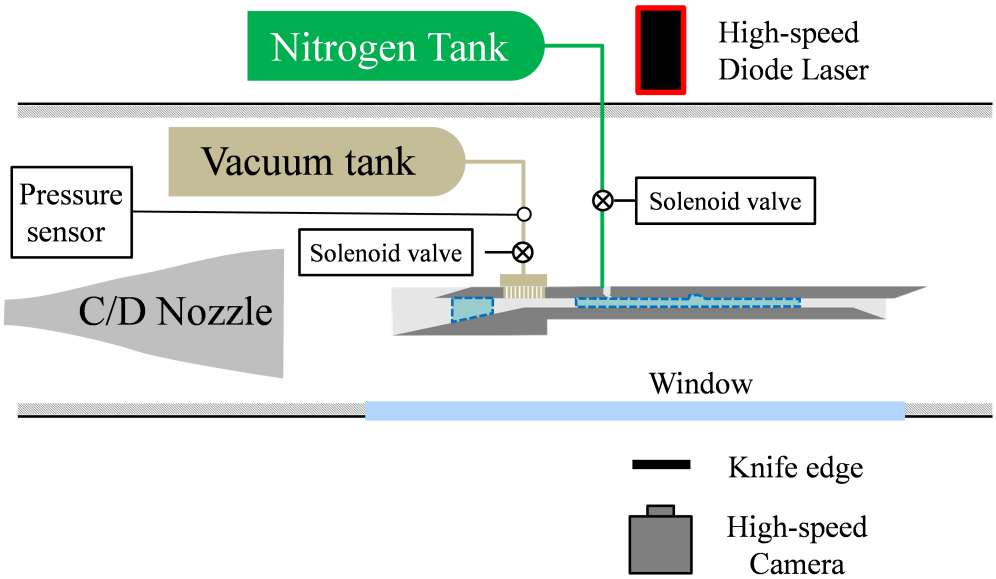

Fig. 3.3 Schematic of the experimental configuration for low-enthalpy flows

Pure nitrogen jet was injected to incur mass-induced inlet unstart in cold conditions. The jet injection was triggered 5 ms after the freestream trigger for 300 ms as shown in Fig. 3.4. A heavy-duty pressure transducer (Honeywell, PX2) monitored the injection pressure. Suction was activated relative to

the jet injection trigger and two suction timings are examined which are designated as "fast" and "late", respectively. The "fast" suction triggers the opening of the suction device 10 ms after the jet injection trigger whereas the "late" triggers after 20 ms. The openings of the nitrogen jet and suction flow were controlled by fast-acting solenoid valves (SMC, VT307) and the estimated suction activation delay was 20 ms on average. An example of activation instances for freestream, jet, fast suction, and late suction are plotted in Fig. 3.4. Suction pressures were monitored by a pressure transducer (Kulite, XCE-062-5A) at a sampling frequency of 20 kHz. The pressure transducer was mounted at the exit of the suction device and the monitored suction pressures were converted into equivalent suction flow rates via ideal gas law with the vacuum tank's volume.

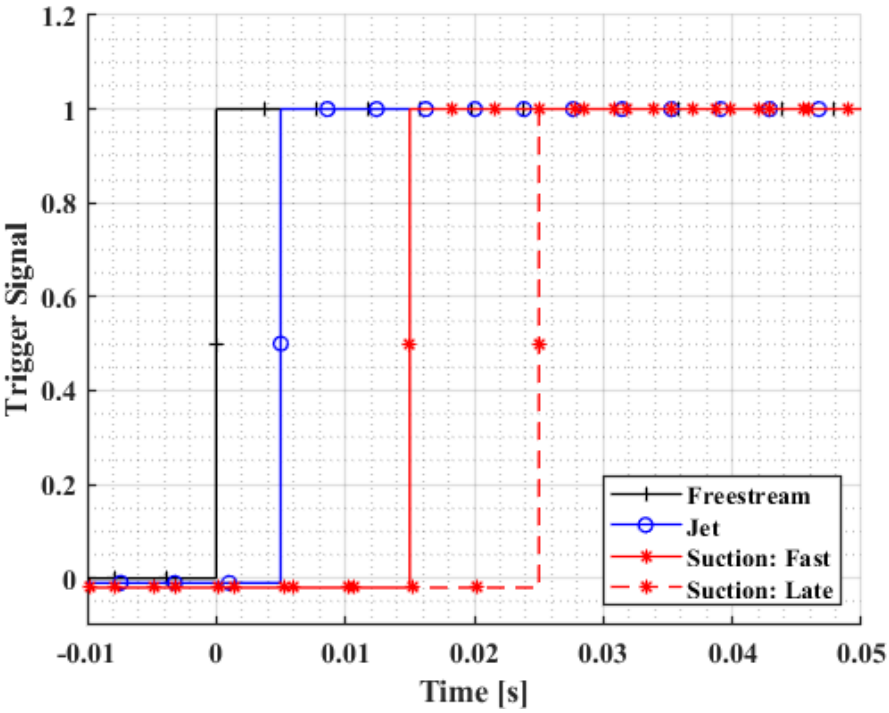

Fig. 3.4 Activation instances for low-enthalpy unstarting flows

A high-speed schlieren imaging technique was adopted to capture the fast-evolving flow structures of unstarting and unstarted flows. The schematic of the schlieren setup is presented in Fig. 3.5. A high-speed diode laser (Cavitar Cavilux Smart. 640 nm) was installed at one side of the test condition and the light from the laser was collected, collimated, focused, and through a pine hole. A high-speed camera (Photron, FASTCAM Ultima APXS) was placed at the other side to capture the temporal and spatial evolutions of the unstarting and unstarted flows at 4,000 frames per second.

To maintain the image resolution high enough, multiple regions of interest (ROI) were selected since the total length of the model was over 600 mm. As a result, five ROIs were chosen to visualize the behavior of unstarting and unstarted shock depending on local pressure gradients; the inlet, isolator, near the jet, near the cavity flameholder, and near the nozzle. Although the images in the ROIs were made individually, at least five identical back-to-back runs were conducted to assure the repeatability of the experiments by moving the imaging region back and forth. The variation of inlet unstart completion was estimated from different runs and was less than 5 ms in the 95 % confidence interval at a given experimental condition. The images are then concatenated when the whole behavior of the unstarting and unstarted flows is needed. More detailed information on tunnel operation is presented in Ref. [180].

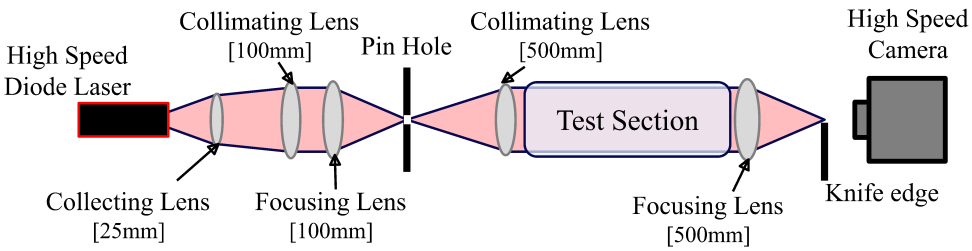

Fig. 3.5 Schematic of schlieren setup

3.1.3 Experimental Conditions

The freestream Mach number and freestream total pressure are fixed at 6 and 300 kPa in both sets of experiments, respectively. For the measure two pressure values, the freestream total pressure (P_{0f})and the jet total pressure P_{0j}, the time-averaged values along with errors in a 95 % confidence interval are tabulated. Two jet injection pressures are selected to vary the mass-loading of unstarting flows: the lower one induces marginally unstarting flows within the test period referred to as "weak unstart", and the other results in a faster unstart by tens of milliseconds, or "strong unstart" via elevating the jet injection pressure by approximately 13 %. In the fifth column of Table 3.1, "*JMR*" is tabulated as the jet-to-freestream mass ratio, representing higher mass-lading for C11 and C12 than for C01 – C03. This higher-loading is even more clear when it comes to the sixth column, "*CMR*". This column tabulates the internal-to-choked mass ratio, as defined in the previous section. For weak unstart flows, *CMR* is just below 0.85, whereas for strong unstart flows *CMR* is around 0.86 which is only 2 % higher than that in weak unstart flows. It is noteworthy that the threshold in mass-loading unstart exists *CMR* below unity. This could be from additional losses such as skin frictions or boundary-layer separations that 1-D equations cannot fully account for. However, because the *CMR* margin to unity is rather significant, it is conjectured that jet injections in high rates led to significant losses through the jet-induced bow-shockwave structure, resulting in severe choked flow rate losses.

To elucidate the effect of suction control, two non-suction cases are set and designated as C01 and C11 for the weak and the strong unstarts, respectively. For the weak unstart, two suction timings are tested as in the last column of Table 3.1, "*dtS*". For the strong unstart, only one suction timing is examined

Table 3.1 Test matrix for cold unstarting flows

Case	Ma	P_{0f}, kPa	P_{0j}, kPa	JMR	CMR	dtS, ms[1]
C01	6	301 ± 2.01	584 ± 8.81	0.146	0.847	N/A [2]
C02	6	301 ± 2.01	584 ± 8.81	0.146	0.847	+10
C03	6	301 ± 2.01	584 ± 8.81	0.146	0.847	+20
C11	6	301 ± 2.01	661 ± 6.30	0.166	0.862	N/A [2]
C12	6	301 ± 2.01	661 ± 6.30	0.166	0.862	+10

[1] Suction trigger relative to the jet injection trigger.

[2] N/A denotes "not applicable".

which will be discussed in the later section.

The temporal profiles of critical tunnel operation parameters are plotted in Fig. 3.6 for the freestream total pressure, jet total pressure, and suction pressures for suction activated cases. The freestream total pressure and jet total pressure are normalized by their respective time averages (left vertical ordinate) and suction pressures and normalized by the nominal freestream static pressures. The suction was deactivated concurrently with the jet injection and pressures at 500 ms were assumed to be in equilibrium and used to estimate the suction mass flow rate.

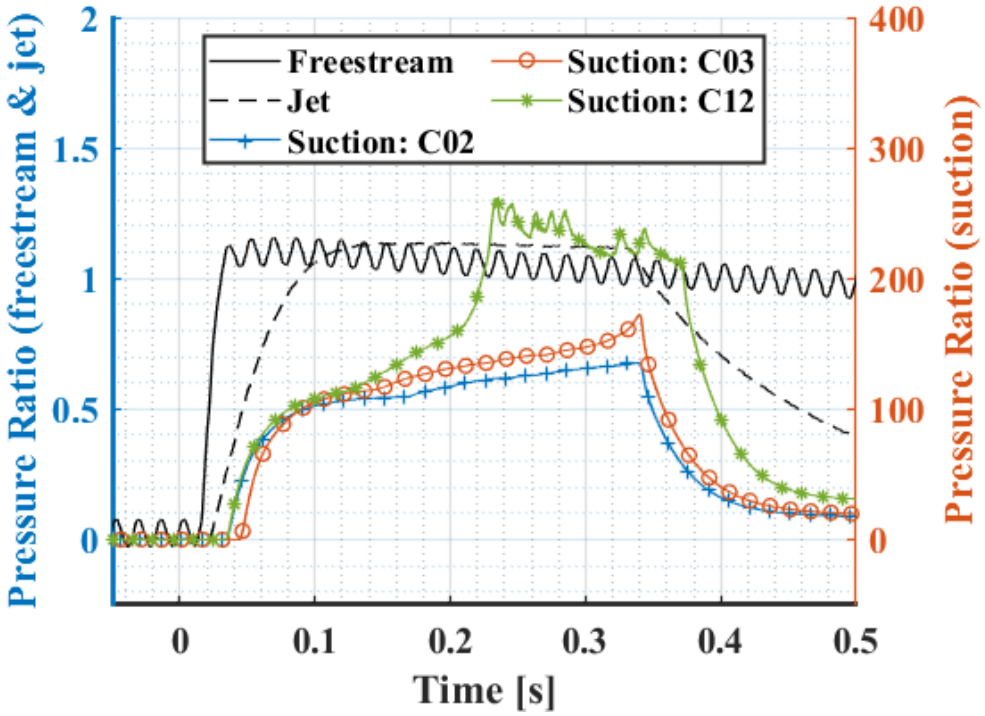

Fig. 3.6 Critical tunnel operation parameters for low-enthalpy unstarting flows

3.2 Test Results

3.2.1 Weak Unstarting Flow without Suction (C01)

Schlieren images at five different ROIs are concatenated and presented in Fig. 3.7 to give an overview of the temporal and spatial evolution of unstarting flow. The corresponding imaging region is highlighted as a red dashed box in the model schematic at the top of the figure. The instant unstart shock locations are denoted as red arrows in each image. Due to the structural issue, sidewalls disabled visualization in a small area near the flameholder cavity, illustrated as black rectangles in each image. Flow is left to right and respective delays relative to the jet injection trigger are presented on the right of the figures. At its early stage of the jet injection Fig. 3.7(a), the flow in the isolator is rather clean. However, near the flameholder cavity, supersonic shear flows just below the cavity (a horizontal black line) and several oblique shockwaves near the close-up ramp are well illustrated seen as evidence of supersonic internal flow. As the jet injection continues, flow choking occurs and a relatively weaker shock near the end of the image appears (Fig. 3.7(b)). This upstream propagation of unstart shock is continued as the jet injection continues to incur a mass imbalance near the choked throat. Furthermore, propagation of the unstart shock is accelerated or decelerated depending on the local pressure gradient (Fig. 3.7(c) – (e)). At 305 ms after the jet injection, the unstart shock reaches the inlet and the schlieren images show no clear flow structure, implying the flow is turned completely subsonic (Fig. 3.7(g)).

To discuss the behavior of the upstream propagation of unstart shockwave in detail, the unstart propagation in each ROI is presented. Although the flow choking is initiated in the near nozzle region, the unstart shock is considerably weak due to the relatively small mass imbalance and small Mach number.

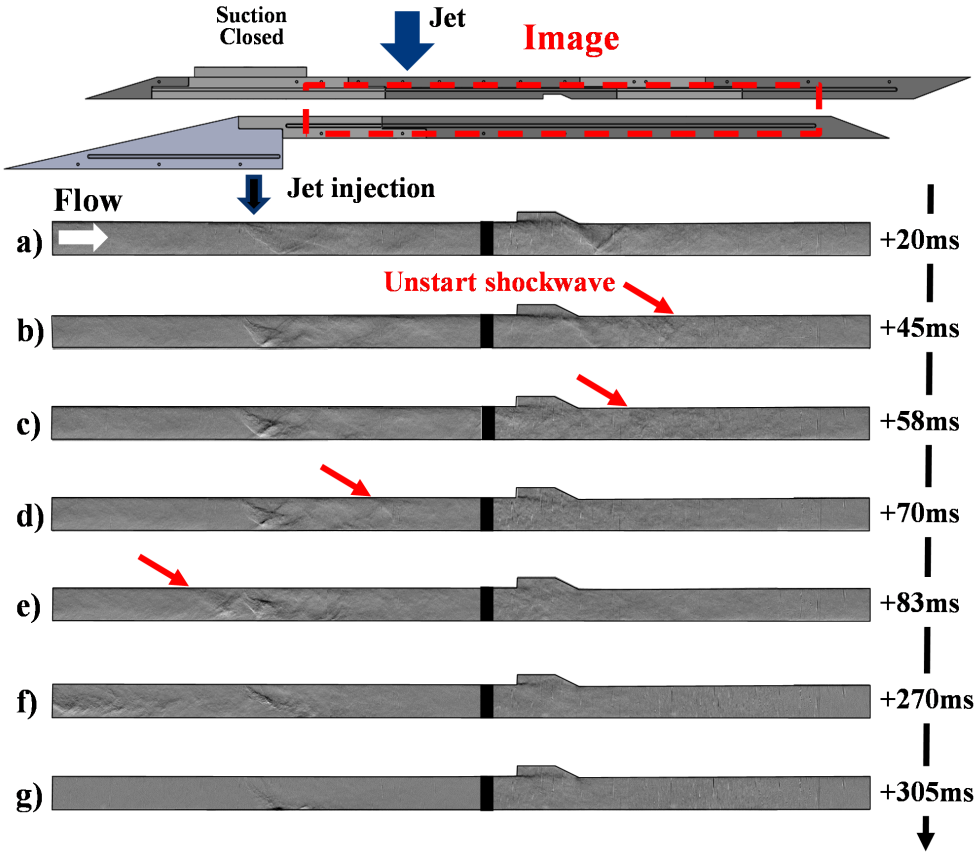

Fig. 3.7 An overview of weak unstart without suction (C01)

Therefore, herein discussions of local flows are presented for four ROIs; near the cavity, near the jet, at the isolator, and at the inlet for Fig. 3.8 – Fig. 3.11, respectively. Firstly, unstart propagation near the cavity is presented in Fig. 3.8. The unstart shock first appears at approximately 35 ms after the jet injection trigger Fig. 3.8(a). Since the unstart shock is located at the end of the current ROI, the upstream portion of the flow remains still supersonic; supersonic shear layer near the backward-facing step and an oblique shock and its reflection near the close-up ramp is clearly visible. The unstart shock is moving at a fairly con-

stant speed at 4 m/s since the unstart shock is under almost zero or very mild favorable pressure gradient (FPG) (Fig. 3.8(b) to (c)). Moreover, the unstart shock becomes more prominent as it approaches the cavity flameholder due to the larger mass-imbalance and higher Mach number. When finally the unstart shock reaches near the close-up ramp, the unstart shock suddenly decelerates and stops for a couple of milliseconds. However, only 2 ms after the unstart shock reaching the downstream end of the cavity, the unstart shock sweeps the cavity with a significantly faster speed at 10 m/s (Fig. 3.8(c) to (d)). This acceleration of upstream motion is due to the adverse pressure gradient (APG) generated by flow separation at the backward-facing step and the oblique shock on the close-up ramp: Since the pressure at the upstream portion is lower, the pressure difference across the unstart shock increases leading to strengthening the unstart shock. After the unstart shock passing the cavity flameholder, supersonic flow structures, such as supersonic shear layers and the oblique shock, indicating the flow is turned to subsonic.

The unstart shock first appears at around t = 55 ms near the jet region as presented in Fig. 3.9(a). Compared to the near cavity case in Fig. 3.8 where the unstart shock moved upstream at a speed of a few m/s, the propagation speed of the unstart shock until reaching the jet injection point is roughly halved, at around 2 m/s (Fig. 3.9(b) to (c)). This is because of the total pressure profile across this region; the total pressure is decreasing in the stream-wise direction mainly due to several reflection shocks from the jet-induced bow shock. In other words, as the unstart shock moves upstream, it encounters flows with higher total pressures which eventually leads to a higher local choked flow rate. Therefore, the propagation of unstart shock is decelerated until reaching the jet injection point. Moreover, the propagation is further decelerated near the jet impingement location since it creates a strong FPG region downstream: due

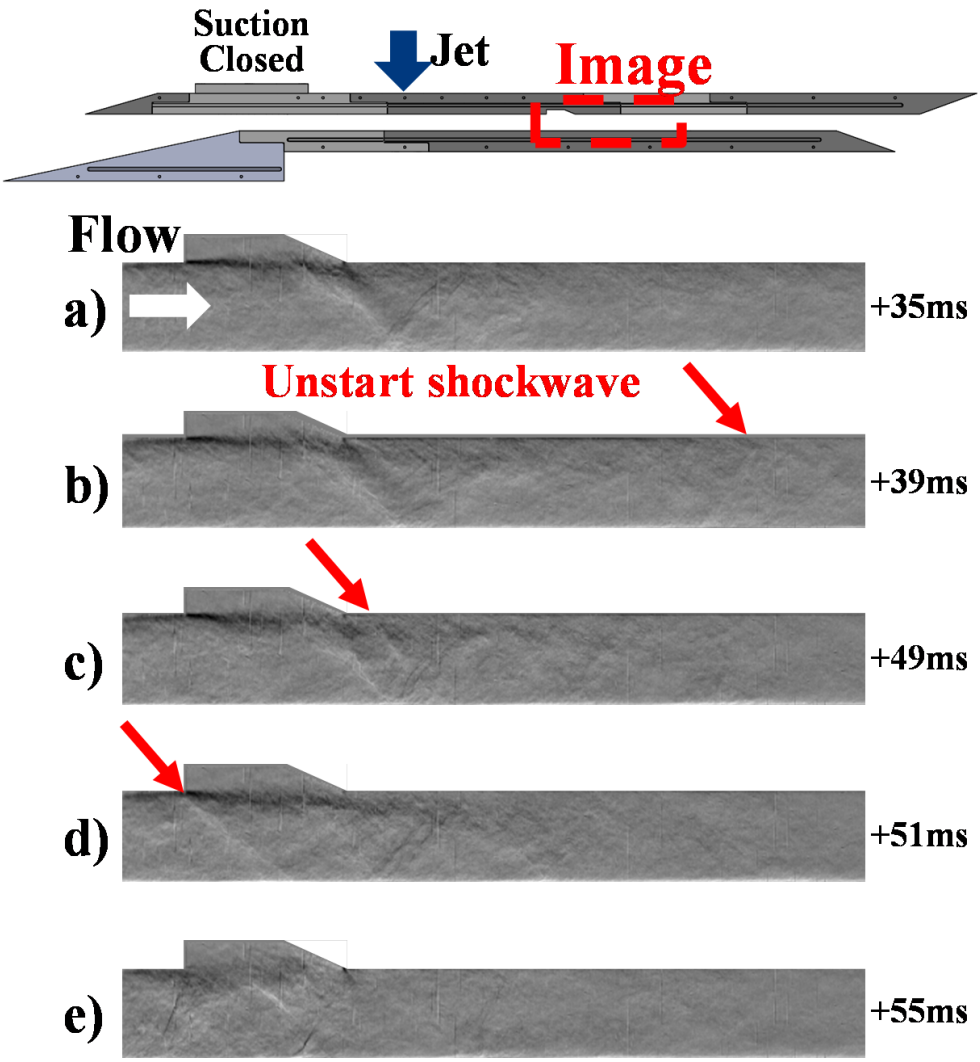

Fig. 3.8 Weak unstart shock propagation without suction near the cavity (C01)

to the higher pressure upstream, the unstart shock needs a larger mass imbalance to overcome (Fig. 3.9(c) to (d)). If the mass imbalance is large enough to overcome the FPG region, another unstart shock system forms upstream of the jet-induced bow shock and moves upstream again, leaving a completely different

structure for the jet (Fig. 3.9(e)).

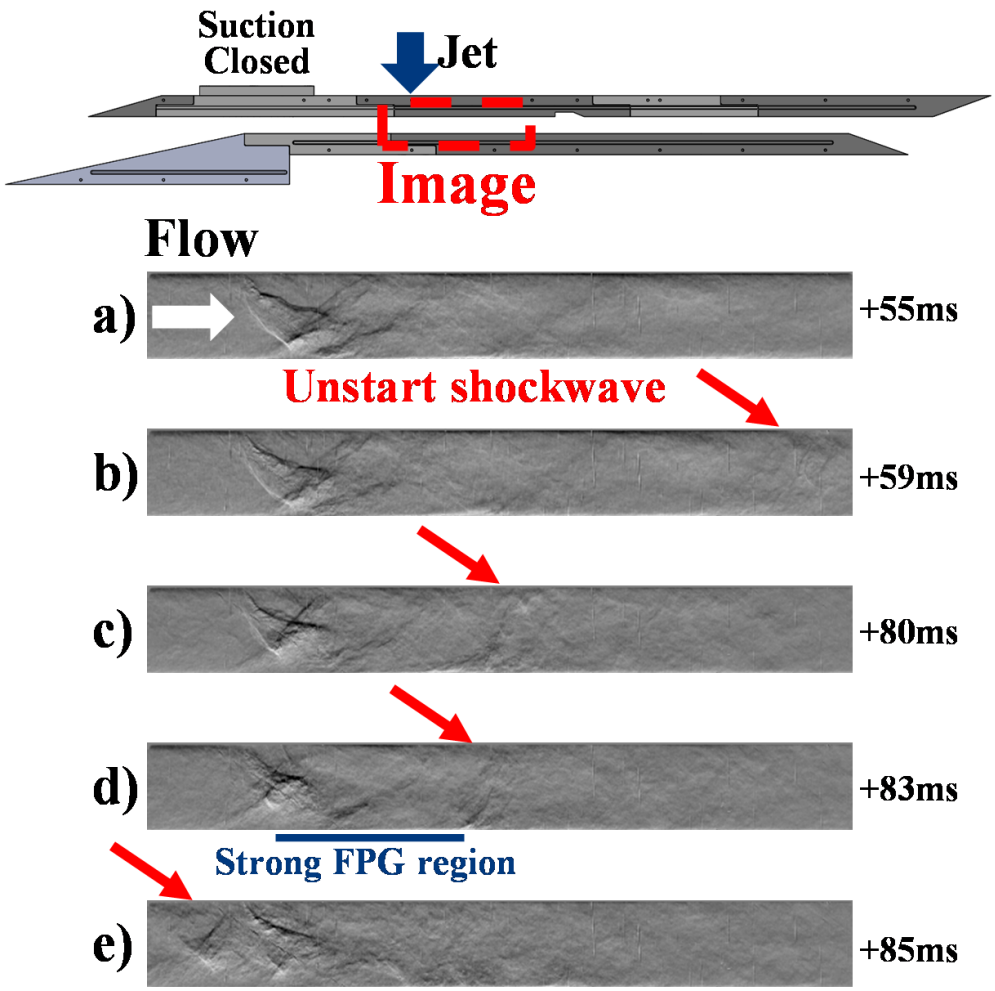

Fig. 3.9 Weak unstart shock propagation without suction near the jet (C01)

The unstart shock is further decelerated in the constant-area isolator region due to the increasing total pressure and thinner boundary-layers moving upstream. The estimated average speed of the unstart shock until reaching the upstream end of the current ROI is approximately 0.5 m/s (Fig. 3.10(b) – (e)),

residing in the isolator for more than 200 ms. Moreover, the propagation becomes even slower and the unstart shock appears almost stopped for a while near the upstream end of the current ROI (Fig. 3.10(e) – (i)). Also, it is noteworthy that the unstart shock structure mainly exists at the lower wall reaching the left end of the current ROI (Fig. 3.10(b) – (i)). However, When it finally reaches the incident shockwave impingement location from the inlet, the high-density gradient region moves from the lower wall to the upper wall (Fig. 3.10(j) to (k)). This is conjectured that the separation from the inlet incident shock and the unstart shock merge and expanded at the upper wall. At around 305 ms after the jet injection trigger, the flow is completely subsonic and no noticeable flow structure can be seen except for the jet impingement point.

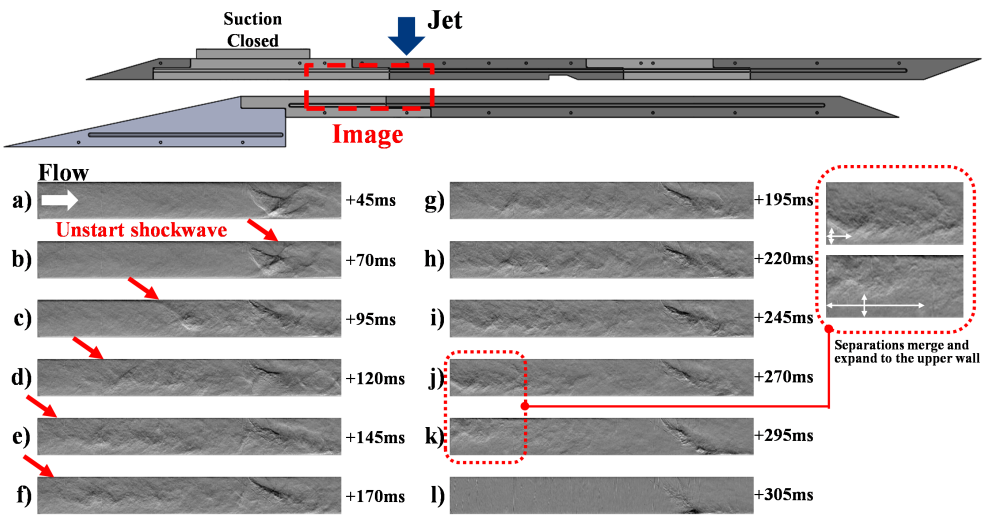

Fig. 3.10 Weak unstart shock propagation without suction at the isolator (C01)

The unstart process at the inlet is presented in Fig. 3.11. Before the unstart shock completely passing through the inlet, multiple quasi-steady shockwave structures in the inlet are well visible and the shockwave from the upper lip is

attached to the cowl (Fig. 3.11(a)). However, as the unstart shock moves upstream with a massive separation, the flow becomes highly transient and chaotic, only taking 10 ms passing the inlet from its first appearance (Fig. 3.11(b) – (e)). This is due to the strong APG by the inlet. While the unstart shock is positioned upstream of the inlet leading edge, the shockwave from the upper lip becomes steeper (Fig. 3.11(c) to (d)) and even a secondary detached shockwave structure is observed (Fig. 3.11(e)). Although the flow structures in- and outside the inlet are highly transient after unstart, inlet buzz phenomenon is not observed.

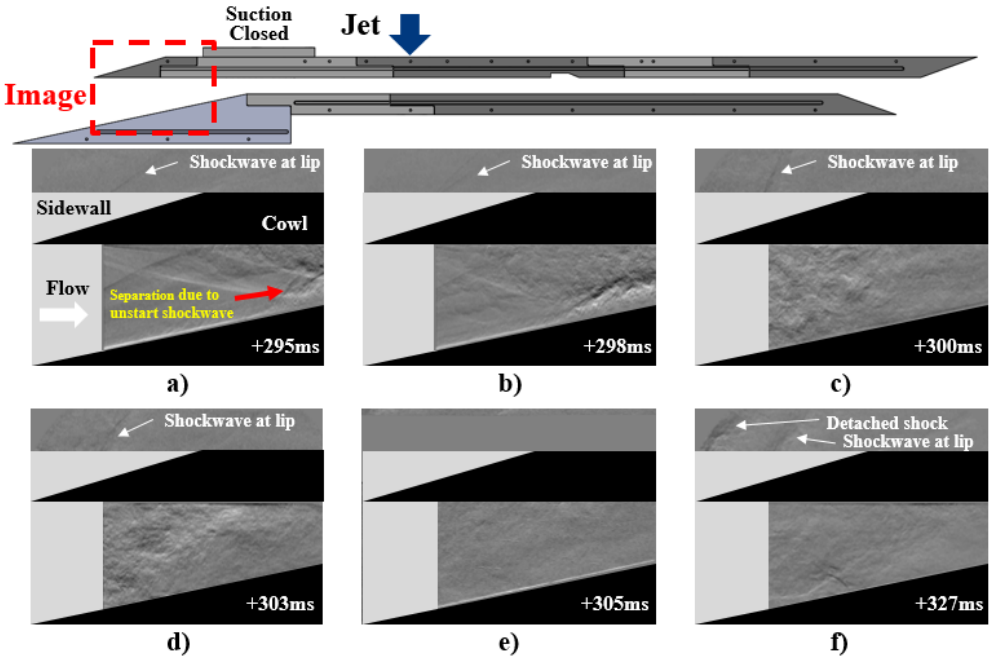

Fig. 3.11 Weak unstart shock propagation without suction at the inlet (C01)

3.2.2 Weak Unstarting Flow with Fast Suction (C02)

In this previous section, the jet injection in the isolator region slowly accumulated mass near the choked throat, leading to unstarting in 305 ms after the jet injection, or namely weak unstart. To elucidate the effect of suction control, boundary-layer suction is activated 10 ms after the jet injection trigger. The overview of the flow behavior in this case (C02) is presented as concatenated schlieren images in Fig. 3.12. The estimated suction flow rate is approximately 1.61 % of the captured mass flow rate at the inlet in the corresponding period. Despite the mass deficit from the boundary-layer suction, the unstart process at its early stage, especially downstream of the jet is remarkably similar (compare Fig. 3.7(a) – (e) to Fig. 3.12(a) – (b)). However, once the unstart reaches the upstream end of the current ROI, the unstart stops moving upstream for roughly 100 ms (Fig. 3.12(c) to (e)). It is noteworthy that the upstream end of the ROI at the isolator region corresponds to the downstream end of the suction device. At approximately 295 ms after the jet injection trigger, the unstart shock slowly moves downstream (Fig. 3.12(f)), and the inlet is remained started over the whole test period (Fig. 3.12).

Since the unstart propagation behavior downstream of the jet was almost identical between non- and fast suction cases, detailed discussion only at the isolator region is presented as in Fig. 3.13. The unstart shock is passing the bow-shock structure at around 70 ms after the jet injection, which is almost unchanged by the suction. Furthermore, the average propagation speed until reaching the upstream end of the current ROI, or the downstream end of the suction device is almost the same (compare Fig. 3.10(b) – (d) and Fig. 3.13(b) – (e)). The remarkable difference that remained the inlet started comes from the period of unstart shocks staying near the suction device. Without boundary-

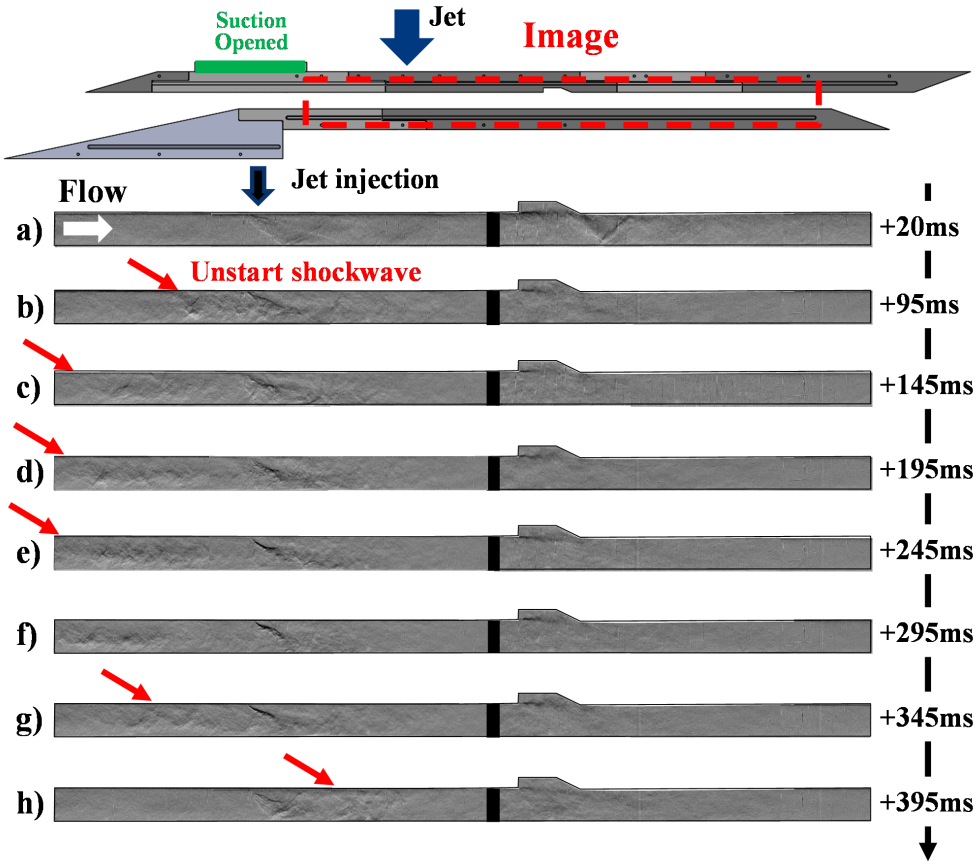

Fig. 3.12 An overview of weak unstart with fast suction (C02)

layer suction in weak unstart for C01, the inlet was eventually unstarted approximately 305 ms after the jet injection trigger. However, in C02, unstart shock moves no further upstream to the suction device or anchored at the location to remain the inlet started. As a result, unstart shock starts to retreat at around 320 ms as the tunnel operation ends. This is because the boundary-layer suction offers an enlarged effective area at the location to increase the local choking flow rate, leading to local mitigation of the mass imbalance from choking to delay the unstart propagation.

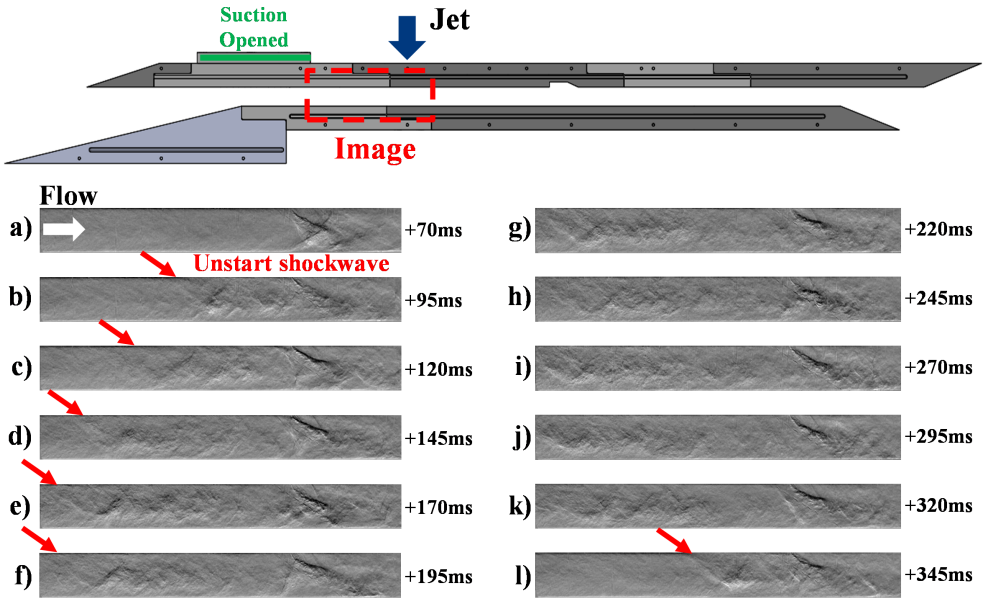

Fig. 3.13 Weak unstart propagation with fast suction at the isolator (C02)

3.2.3 Weak Unstarting Flow with Late Suction (C03)

In the previous section, it was shown that an excessive jet injection just above the unstart threshold without boundary-layer suction leads to marginal, or weak unstart (C01). In contrast, when the suction was triggered 10 ms after the jet injection trigger, inlet unstart was successfully suppressed solely by boundary-layer suction control. In this section, the suction trigger delay is increased by 10 ms more, which is 20 ms after the jet injection trigger to evaluate the effectiveness of the boundary-layer suction control by delayed operations. Other experimental configurations and conditions remain the same. The estimated suction flow rate is 1.81 %.

The overall unstart propagation is illustrated for C03 in Fig. 3.14. Similar to the previous weak unstart cases (C01 and C02), the propagation downstream of the jet is almost identical, unstart shock passing the jet injection point at

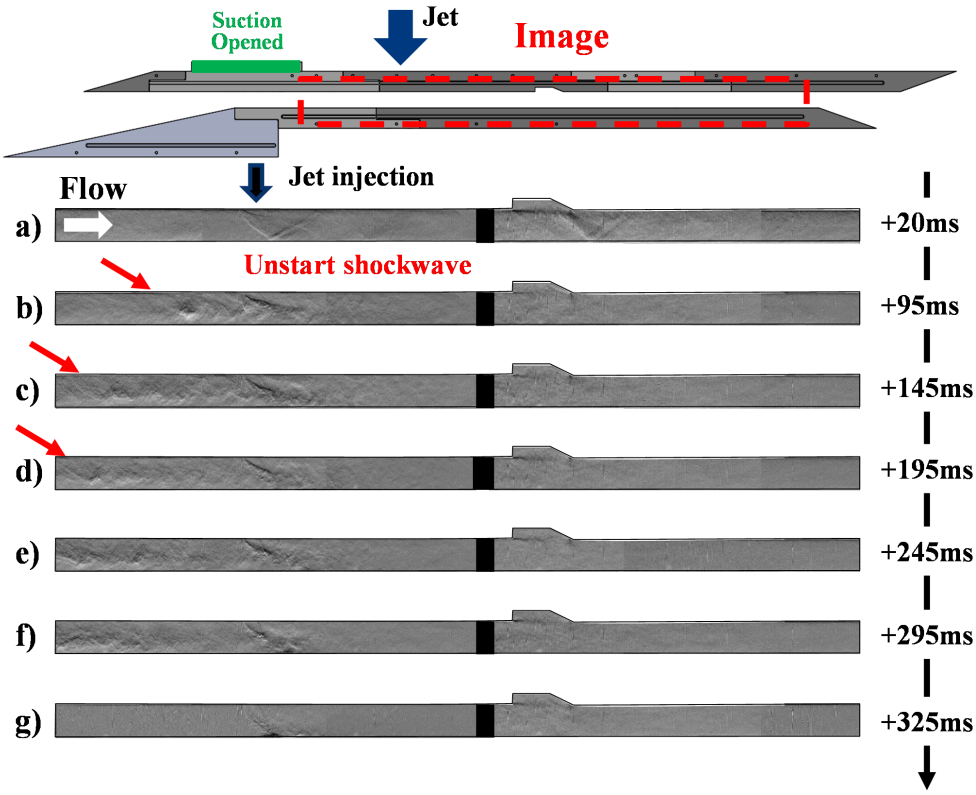

Fig. 3.14 An overview of weak unstart with late suction (C03)

around 95 ms after the jet injection. Moreover, the propagation speed at the isolator remains the same, reaching the perforated plate at approximately 145 ms after the jet injection (see Fig. 3.14(c) to Fig. 3.10(e) and Fig. 3.13(d) for comparison). In the non-suction case (C01), the unstart shock further moved upstream from the perforated plate, unstarting the inlet at 305 ms. In contrast, the unstart shock remained at the point for over 100 ms in the fast suction case, remaining started. When the suction is activated 20 ms after the jet injection as in the current case, the unstart shock does not stop at the perforated plate, moving upstream to unstart the inlet at approximately 325 ms.

To discuss the flow behavior in detail, unstart propagation at the isolator from its first appearance to a complete unstart is depicted in Fig. 3.15. The overall propagation behavior and speed until reaching the perforated plate are almost identical across the weak unstart cases (compare Fig. 3.10(b) – (e), Fig. 3.13(a) – (d), and Fig. 3.15(a) – (d)). However, despite the boundary-layer suction at 1.81 $ of the freestream, the unstart shock keeps moving upstream to eventually unstart the inlet at 325 ms. It is noteworthy that unstart shock was anchored only by 1.61 % of mass extraction from boundary-layers in C01, indicating the working mechanism of boundary-layer suction control. If the mass imbalance was majorly mitigated by the mass extraction, a higher suction rate would have shown higher effectiveness. However, by applying 10 ms more of a delay, the boundary-layer suction control lost its effectiveness. This shows the boundary-layer suction control mainly acts to suppress and thin boundary-layers to increases the local choked flow rate, not directly matching the mass imbalance from the mass extraction. Therefore, 10 ms of further delay allowed the boundary-layer to grow with time leading to a less increase of the local choked flow rate and lesser effectiveness.

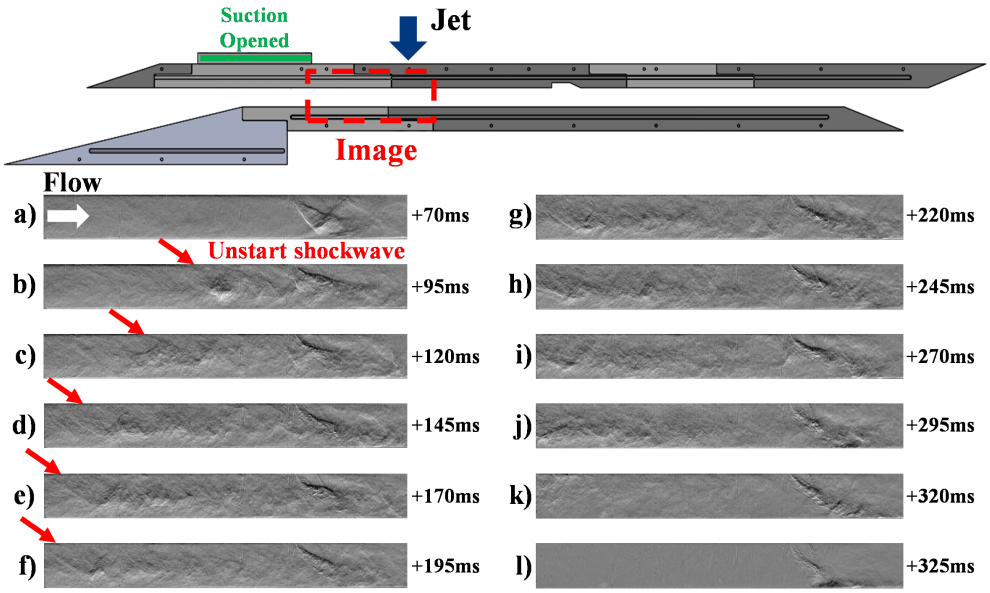

Fig. 3.15 Weak unstart propagation with late suction at the isolator (C03)

3.2.4 Strong Unstarting Flow without Suction (C11)

Unstarting flow is simulated via excessive non-reacting jet injection at the combustor region which leads to flow choking and subsequent mass imbalance to unstart the inlet. Therefore, one could expect a higher mass-loading would induce a stronger unstart shockwave system since it accumulates the imbalanced mass at a higher rate near the choking point. Thus, jet injection pressure was increased by approximately 13 % which results in a roughly 1.7 % increase in terms of *CMR*.

The overall temporal and spatial evolution of strong unstarting flow without boundary-layer suction is illustrated in Fig. 3.16. Despite the higher mass-loading, the overall behavior of the upstream-propagating unstart shock remains the same as the weak unstart cases until reaching the jet injection point (compare Fig. 3.7(a) – (d) and Fig. 3.16(a) – (c)). However, after passing the jet

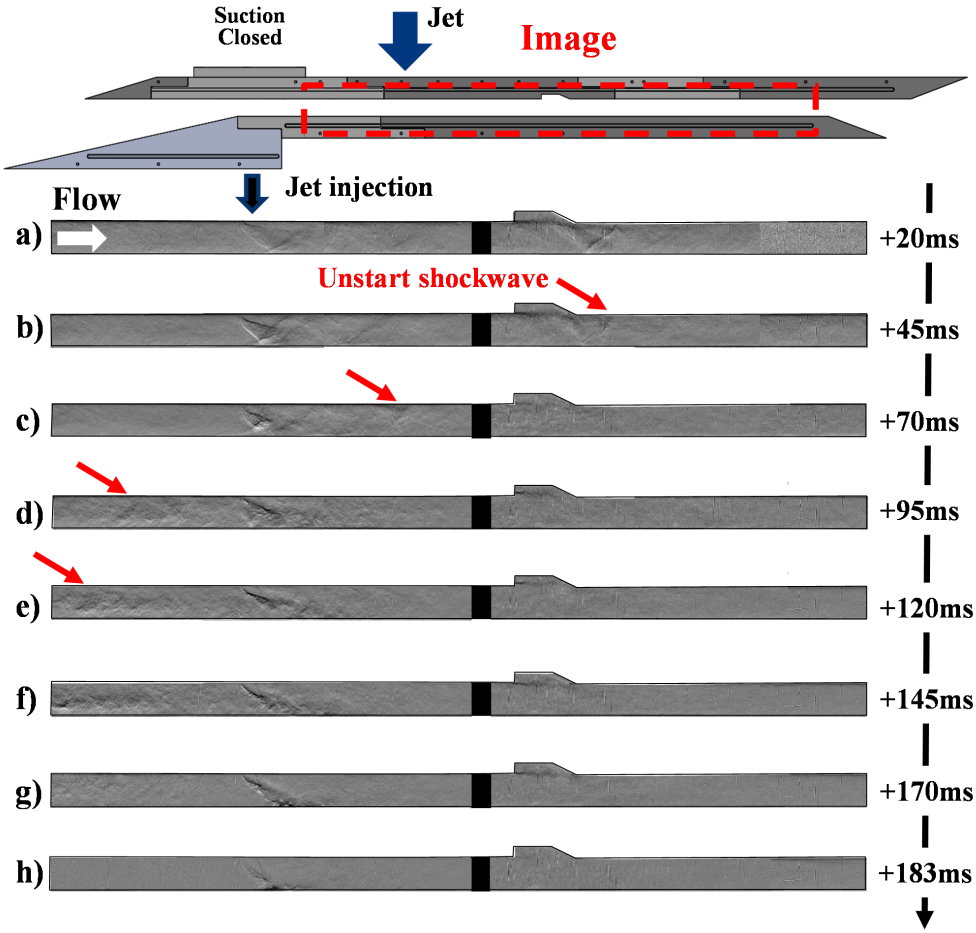

Fig. 3.16 An overview of weak unstart without suction (C11)

injection point, unstart shock moves upstream at a higher speed than that in weak unstart cases, arriving at the perforated plate at around 120 ms after the jet injection trigger. Although the propagation decelerates after reaching the suction device, the propagation speed at the location is still faster than that in weak unstart cases, unstarting the inlet at approximately 183 ms after the jet injection trigger.

To discuss the differences in flow details in weak and strong unstart cases,

unstart propagations at four different ROIs from downstream locations are presented in Fig. 3.17 – Fig. 3.20. Firstly, unstart propagation near the cavity is presented in Fig. 3.17. Although there is 2 ms of the time difference between the weak and strong unstart cases, the differences in overall behavior and propagation speeds are insignificant in weak and strong unstart cases (compare Fig. 3.8 and Fig. 3.17).

Strong unstart propagation near the jet injection point is shown in Fig. 3.18. Similar to the region near the cavity, overall behavior and propagation speed are nearly unchanged (see Fig. 3.18 for comparison), being different only a few milliseconds in time for the processes including a slight deceleration near the strong FPG region behind the jet (Fig. 3.18(c) to (d)).

Since unstart propagation speed and behavior were almost identical for both weak and strong unstart cases, strong unstart shock reaches the isolator at almost the same time as the weak one (Fig. 3.19). For the non-suction weak unstart case (C01) in which it took approximately 75 ms to reach the upstream end of the current ROI from the jet injection point. However for strong unstart, it takes only half the amount of time to reach (Fig. 3.19(b) – (d)), i.e., the propagation speed is twice faster than in C01 (approximately 1 m/s). Moreover, this propagation at a higher speed continues until reaching the inlet, resulting in inlet unstart at 183 ms although flow details remain almost identical for both weak and strong unstart cases (refer to Fig. 3.10). This indicates the main mechanism of the unstarting flows: mass-loading induced choking incurs inlet unstart in the current setup. To increase the mass-loading, the jet injection pressure was increased. This increased jet total pressure not only increases the total mass flow rate in the passage but also increases the local choking flow rate. Therefore, the mass imbalance due to the mass injection was somewhat balanced between the two cases. In contrast, in upstream regions of the jet,

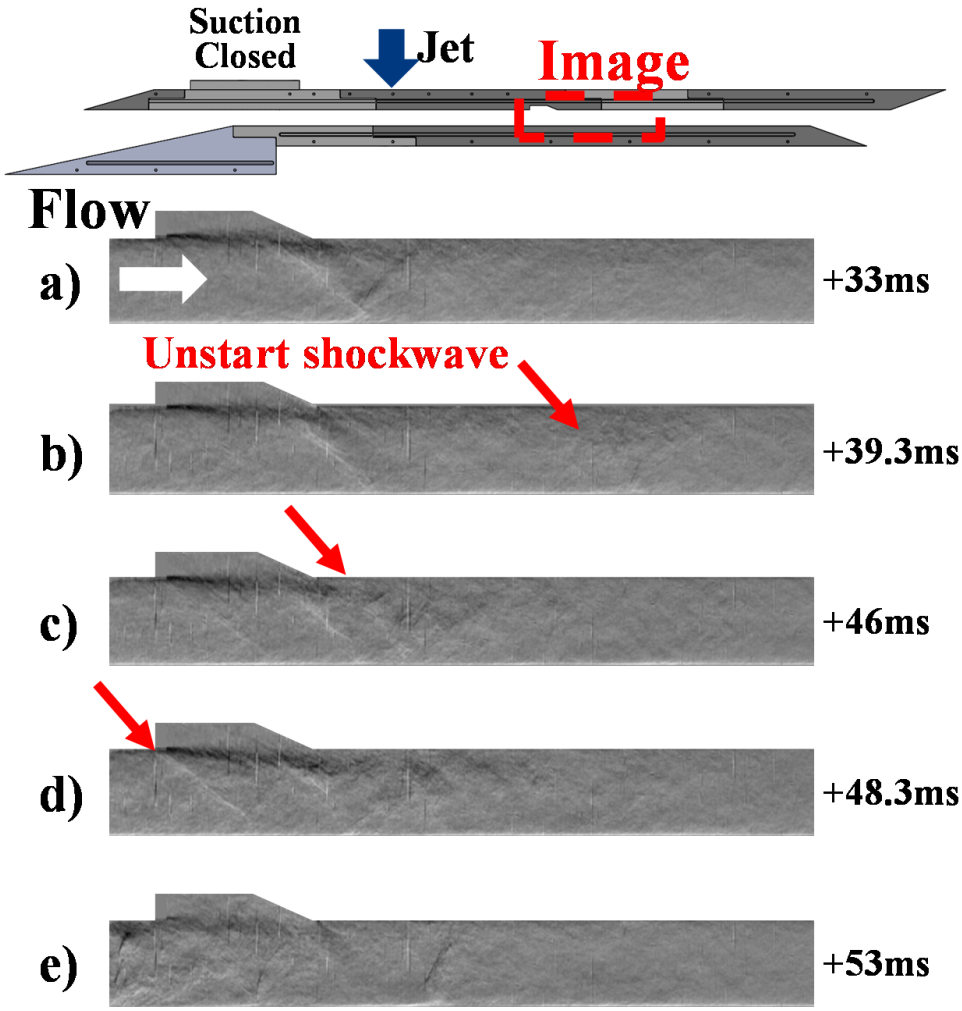

Fig. 3.17 Strong unstart propagation without suction near the cavity (C11)

the increased jet injection pressure does not increase the local choked flow rate, but only increases the mass imbalance and its accumulation rate downstream. Therefore, due to the higher imbalance, the propagation at the isolator region is faster than at a lower jet injection rate.

Since the strong unstart shock moved faster at the isolator region for C11,

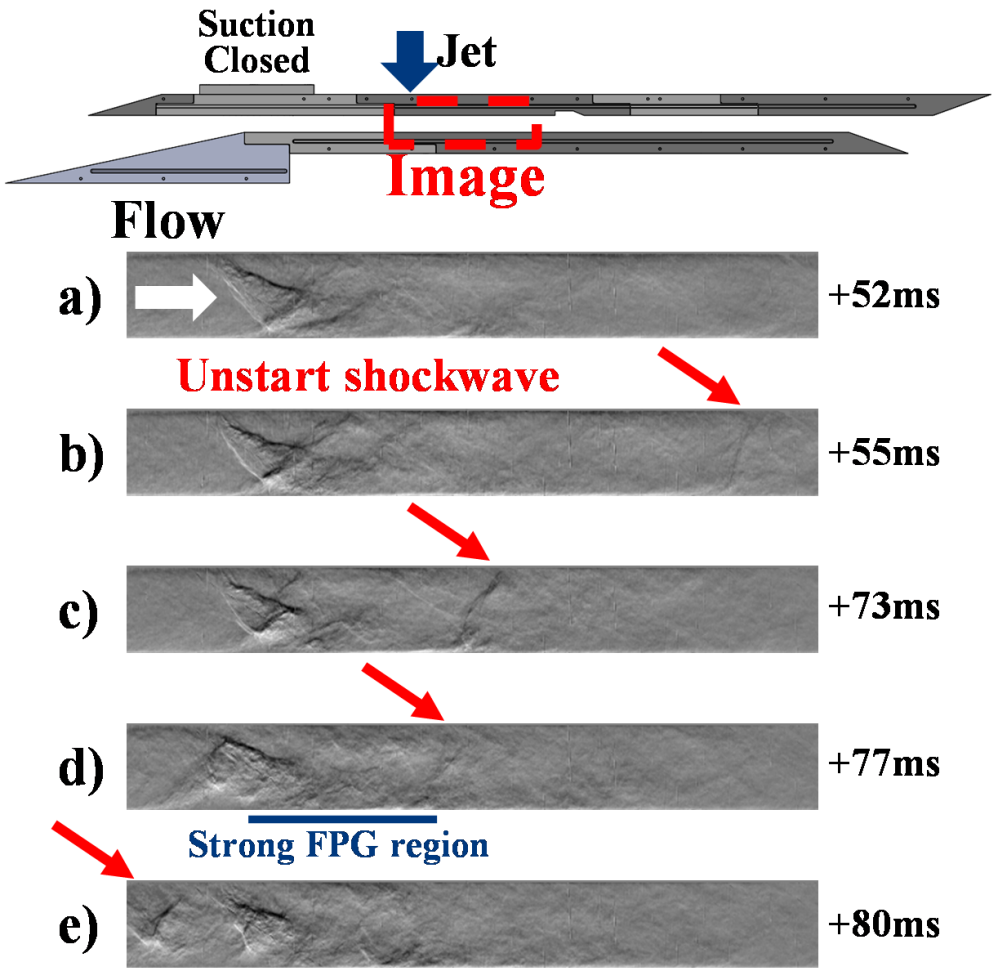

Fig. 3.18 Strong unstart propagation without suction near the jet (C11)

unstart shock arrives at the inlet faster by approximately 120 ms than for weak unstart, C11 (compare Fig. 3.11(a), and Fig. 3.20(a)). Due to the higher mass imbalance downstream, the propagation speed of unstart shock is almost twice faster than for C11, unstarting the inlet in 5 ms (Fig. 3.20(a) – (c)). Again, inlet buzz phenomenon is not observed after unstart.

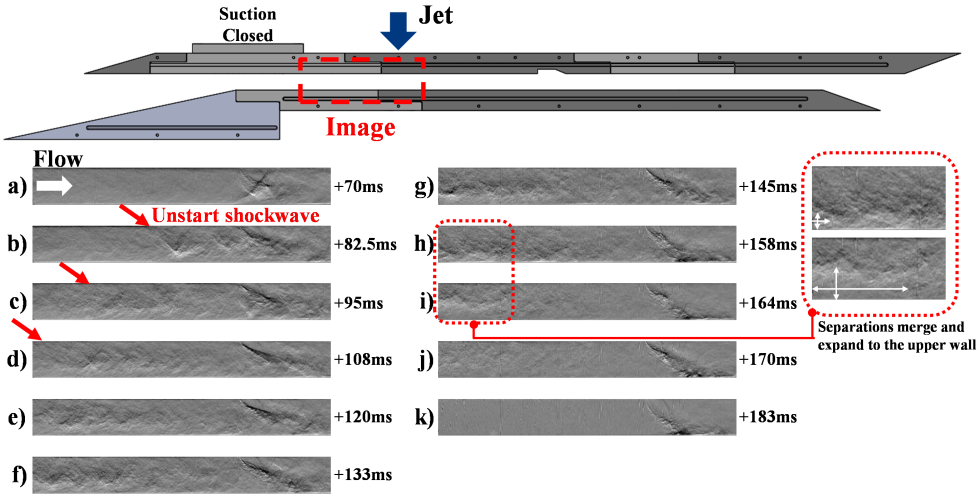

Fig. 3.19 Strong unstart propagation without suction at the isolator (C11)

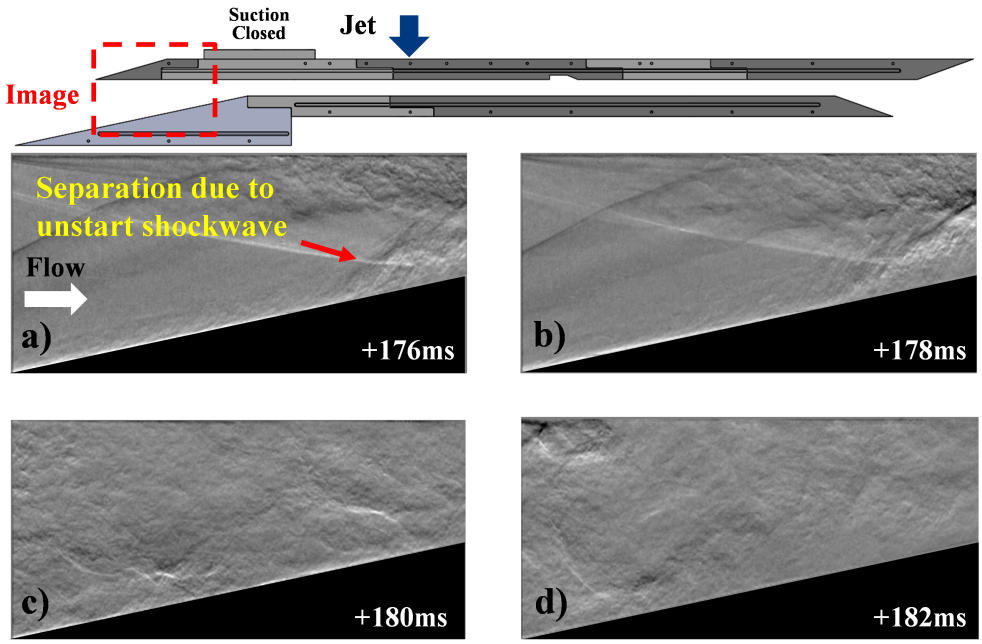

Fig. 3.20 Strong unstart propagation with late suction at the inlet (C11)

3.2.5 Strong Unstarting Flow with Fast Suction (C12)

Boundary-layer suction control is triggered 10 ms after the jet injection trigger to examine its effectiveness under a higher mass-loading, that is, the strong unstart. The test conditions are maintained constant to the equivalent non-suction case (C11) and the estimated suction flow rate is 2.83 % of the freestream flow rate.

The overview of a strong unstart process with fast suction is shown in Fig. 3.21. Similar to the other cases, the overall flow structure and propagation behavior are almost identical downstream of the jet injection point: unstart shock arrives at the cavity at around 50 ms (Fig. 3.21(b)) and reaching the jet injection point at approximately 75 ms (Fig. 3.21(c)). Moreover, the unstart propagation speed at the isolator is 1 m/s, which is consistent with the equivalent non-suction case (C11). However, unlike in the non-suction case, the propagation near the suction device is slightly decelerated, resulting in inlet unstart at 208 ms which is approximately 25 ms later than that in the non-suction case (refer to Fig. 3.16).

As discussed above, the differences in flow behaviors downstream of the jet injection point are marginal. Therefore, a detailed discussion of the isolator region is presented only. Schlieren images illustrating the unstart process at the isolator is presented in Fig. 3.22. The behavior of unstart shock and its propagation speed is still nearly unchanged until reaching the perforated plate (Fig. 3.22(a) – (d)). Although the unstart shock eventually moves upstream, its propagation is slightly decelerated under the suction device, which can be seen as the delayed boundary-layer separations merging by approximately 21 ms (compare Fig. 3.19(i) and Fig. 3.22(k)). Finally, the inlet is unstarted at 208 ms after the jet injection trigger which is 25 ms later than that in the

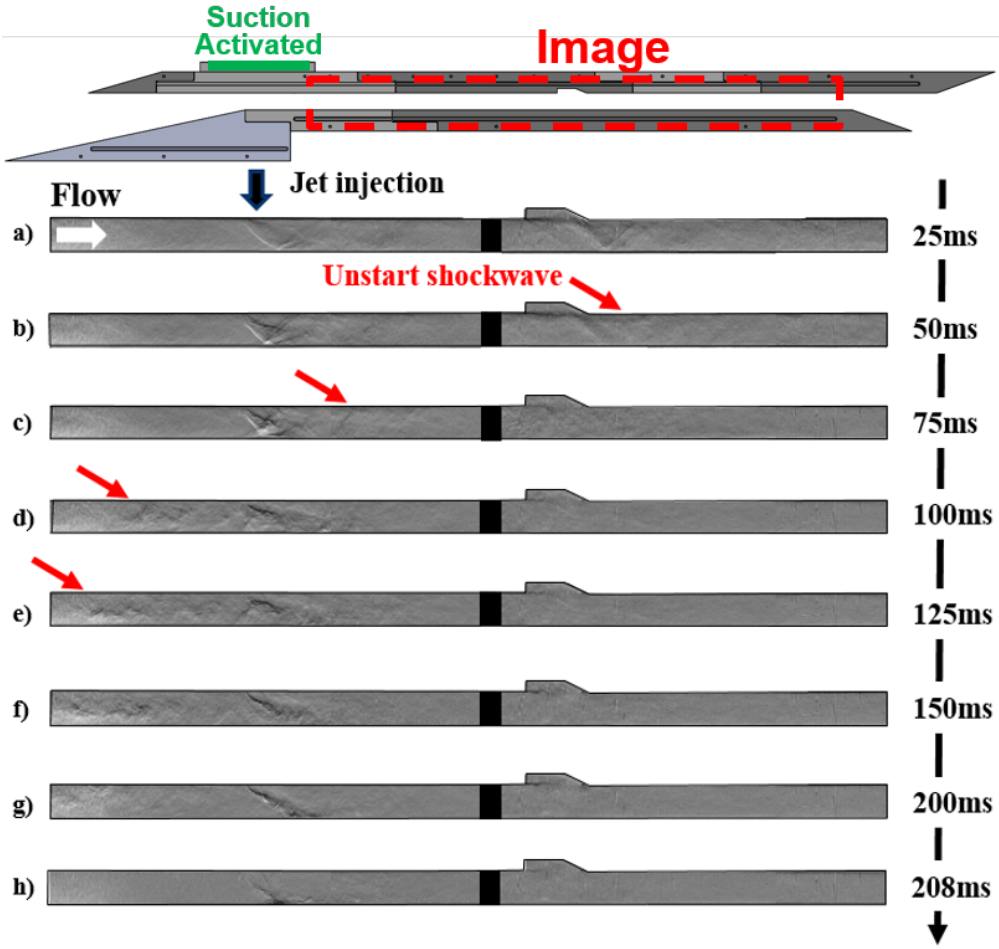

Fig. 3.21 An overview of strong unstart with fast suction (C12)

equivalent non-suction case (C11). The effectiveness of suction control in strong unstart cases can be concluded as follows: since the mass imbalance rate is higher in strong unstarts, the level of boundary-layer suppression offered by 10 ms-delayed-operation could not sufficiently increase the local choking flow rate, eventually leading to inlet unstart. Even so, by boundary-layer suction, inlet unstart is delayed by a couple of tens of milliseconds. Therefore, a higher

suction rate or faster activation is required in higher mass-loadings.

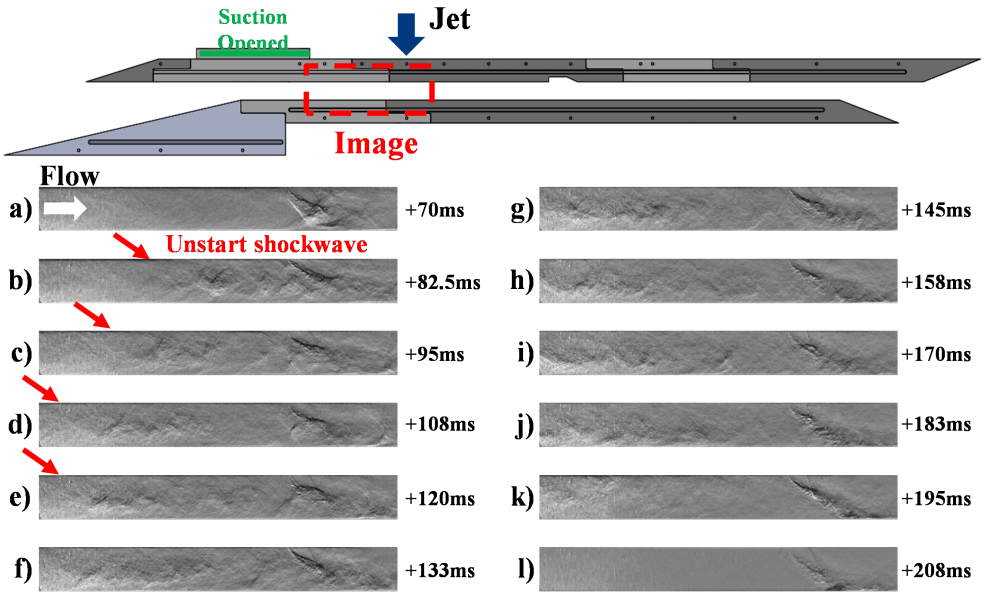

Fig. 3.22 Strong unstart propagation with fast suction at the isolator (C12)

3.3 Summary

Boundary-layer suction control for unstarting flow is examined in this section. An excessive mass injection at the combustor region induced mass flow choking and subsequently inlet unstart. It was found that the unstart process completes faster in higher mass-loadings although the overall flow behavior and structure remain identical. To investigate the effectiveness of the control, boundary-layer suction was activated with delays relative to the jet injection trigger. For weak unstart, fast actuation and a couple of mass extraction were sufficient to solely anchor the unstart shock at the suction device, resulting in avoiding inlet unstart for the whole test period. However, when the delay was further increased (to 20 ms, late actuation), inlet unstart could only be delayed by a few tens of milliseconds. On the other hand, in strong unstart, even the fast actuation of boundary-layer suction control was not enough to stop the unstart shock, eventually leading to inlet unstart. In this case, unstart was also delayed by a few tens of milliseconds. Interestingly, inlet buzz was not observed throughout any case under test. Therefore, it could be concluded that there exists a controllable regime of activation delays of boundary-layer suction control, which also depends on the level of mass-loading.

Chapter 4

Boundary-layer Suction Control in Low-Enthalpy Flows: Unstarted Flows

In the previous section, boundary-layer suction control under low-enthalpy freestream conditions for unstarting flows is examined. In the current section, boundary-layer suction control is applied to unstarted flows to investigate the effectiveness under those conditions.

4.1 Experimental Configuration

4.1.1 Test Model

Inlet buzz phenomenon occurs from momentary mitigation of mass imbalance due to flow choking. In other words, an inlet would experience a higher degree of mass imbalance if inlet buzz is not observed as in Chapter 3. Since the level of control by boundary-layer suction is limited from its mass flow rate in the current setup, the maximum effectiveness of control would be achieved near the marginal conditions; under inlet buzz conditions. Therefore, the geometry of the test model described in Section 3.1.1 is slightly modified to give it a better starting capability. That is, the upper wall of the test model is recessed further by 55 mm, leaving the leading edge from the lower wall and the upper wall by 100 mm whereas other components and dimensions remain the same. This further recession is to provide a thinner boundary-layer at the inlet to increase local choked flow rates, as depicted in Fig. 4.1

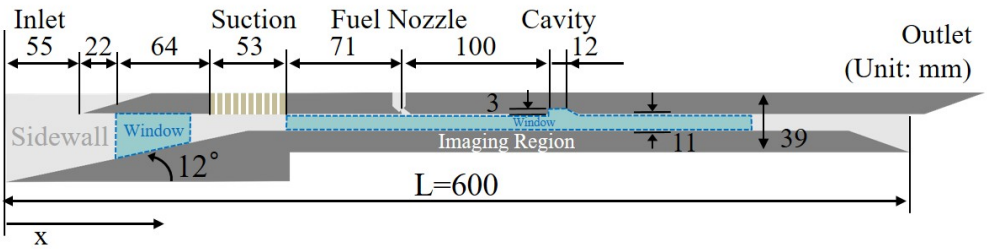

Fig. 4.1 Schematic of the model scramjet for low-enthalpy unstarted flows

4.1.2 Test rig and Instrumental Setups

Again, a supersonic/hypersonic wind tunnel ACT-1 was used for the investigations. The test rig configuration and instrumental setups are almost identical to that is described in Section 3.1 except for the jet injection. Critical tunnel operation parameters for the current investigation are plotted in Fig. 4.2 for the freestream total pressure (plenum), jet total pressure (jet), and suction pressure (suction) which are normalized by its time-average, maximum, and the nominal freestream static pressure, respectively. Two different pressure levels are used in the current study to simulate fuel-cut after unstart to re-start the inlet. The pressure is sharply changed at around 255 ms after the jet injection trigger by switching the openings of two pure nitrogen storage tanks at different pressures. Since the test time is limited to approximately 0.5 seconds, the higher pressure level injects additional mass into the combustor region 5 ms before the freestream to unstart the inlet as fast as possible. The lower pressure level represents the pressure level used to re-start the inlet. If boundary-layer suction is activated, the suction is triggered concurrently with the pressure cut-off. The high-speed schlieren technique is also adopted but only at the inlet region.

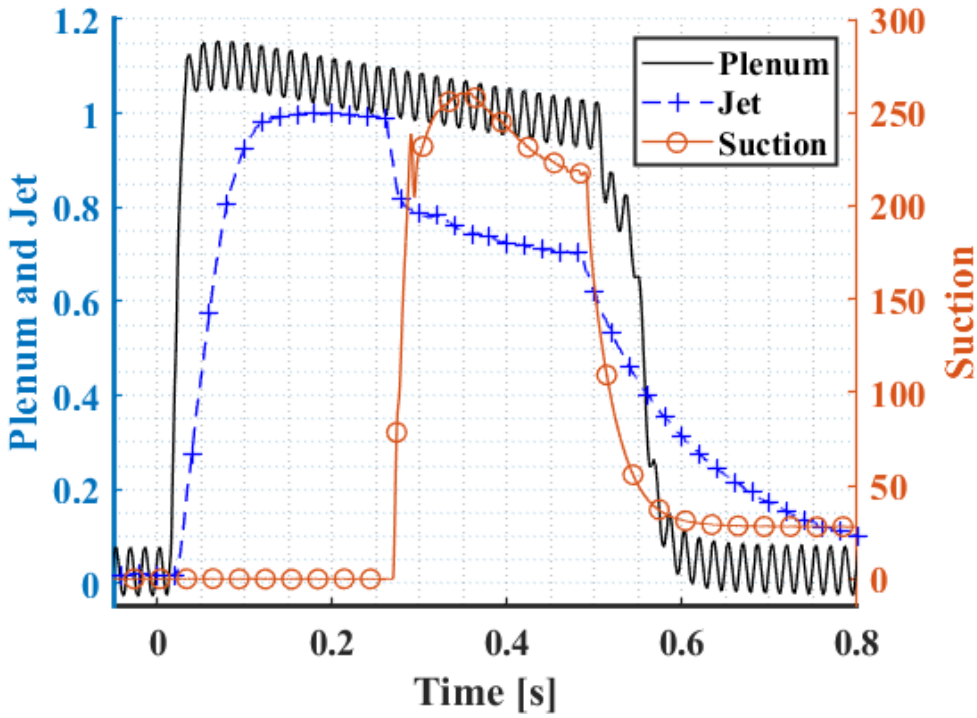

Fig. 4.2 Critical tunnel operation parameters for unstarted flows

4.1.3 Experimental Conditions

Experimental investigations are performed under low-enthalpy Mach 6 conditions. The freestream total pressure is again fixed at 300 kPa which is tabulated with errors in a 95 % confidence interval in the third column of Table 4.1, P_{0f}. To simulate a fuel jet cut-off after unstart, two pressure levels are used, which are denoted as "High" and "Low" under the jet total pressure column, P_{0j}. Those two pressure levels are switched 255 ms after the jet injection trigger. B01 is the reference case in which only fuel jet cut-off is executed without boundary-layer suction. In B02, boundary-layer suction is activated concurrently with the jet cut-off at 255 ms.

Table 4.1 Test matrix for unstarted flows

Case	Ma	P_{0f}, kPa	P_{0j}, kPa		dtS, ms[1]
			High	Low	
B01	6	301 ± 2.01	779	544	N/A [2]
B02	6	301 ± 2.01	779	547	+255

[1] Suction trigger relative to the jet injection trigger.

[2] N/A denotes "not applicable".

4.2 Test Results

4.2.1 Unstarted Flows without Suction

To investigate the effectiveness of the boundary-layer suction control on unstarted flows, unstarted flow is first induced by excessive jet injection. As a result, the inlet is unstarted within a few tens of milliseconds. After being unstart, the flow at the inlet shows an oscillatory flow motion, repeating started and unstarted state which is captured by fast schlieren imaging. An example of a periodic flow motion of one cycle before fuel jet cut-off is depicted in Fig. 4.3. The time instance at the bottom right of each image is a time delay to the first image presented here (Fig. 4.3(a)). This periodic cycle of flow motion starts with an upstream motion of unstart shock due to higher mass imbalances downstream (Fig. 4.3(a) to (b)). Unstart shock impinges on the upper wall cowl ((Fig. 4.3(b)), and moves further upstream (Fig. 4.3(c)). However, if the unstart shock is located too far from the upper wall cowl, supersonic flow turnings from the oblique unstart shock induce flow spillages near the cowl, decreasing the capture flow rate. This temporarily and directly mitigates the downstream mass imbalance, leading to re-swallowing of the unstart shock ((Fig. 4.3(c) to (d)). Nevertheless, the unstart shock moves upstream again when the mass imbalance is large enough by the continued jet injection (Fig. 4.3(f)), which closes a whole cyclic motion. This one cyclic motion takes 12.5 ms which corresponds to 80 Hz.

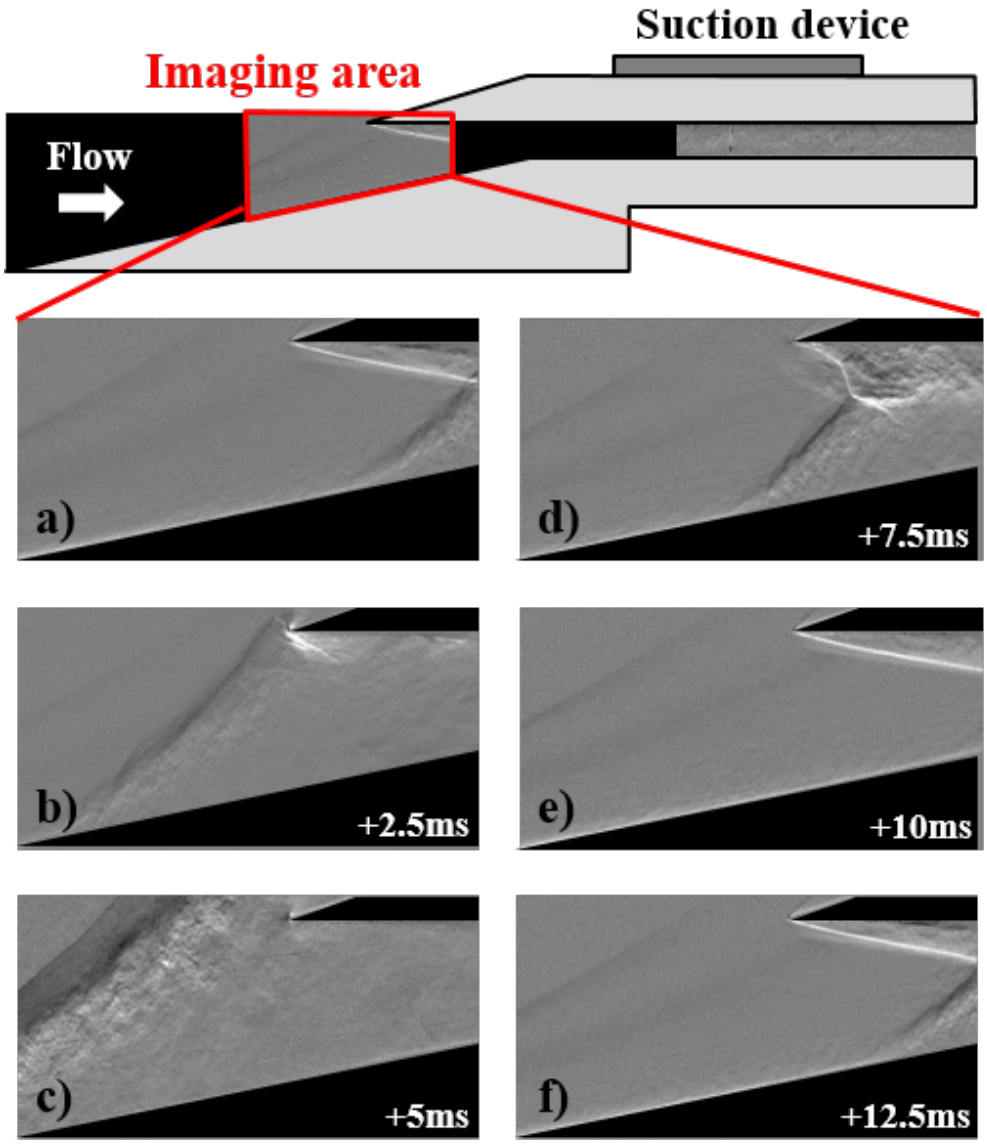

Fig. 4.3 Oscillatory flow motion after unstart: inlet buzz

In Fig. 4.3(b), the schlieren intensity surges at the leading edge of the upper wall cowl when the unstart shock impinges on it since the sharp flow turning flow the shock and the cowl. Therefore, the intensity at the leading edge of the

cowl in an arbitrary unit is traced in time to locate the unstart shock as in Fig. 4.4. The abscissa is the time delay from the freestream trigger (t = 0), and the black dashed line indicates the time when the unstart disgorged out of the inlet. Two red dashed lines represent the timings of pressure level switching and tunnel operation end, respectively. After unstart, inlet buzz phenomenon can be seen which is depicted as pixel intensity peaks between t = 0.1 s and t = 0.255 s. The peaks are two points with close gaps because the unstart shock impinges onto the leading edge twice when traveling in and out of the inlet. The gap between those two peaks is within a few milliseconds, indicating that the unstart shock is not located too far away from the leading edge. At t = 255 ms, the jet injection pressure is changed to the lower level. Note that the lower pressure level is below the unstart threshold observed in Chapter 3. Thus, even at the reduced mass injection rate, the mass imbalance is not immediately mitigated, resulting in unstable inlet buzz but at decreasing frequencies in time.

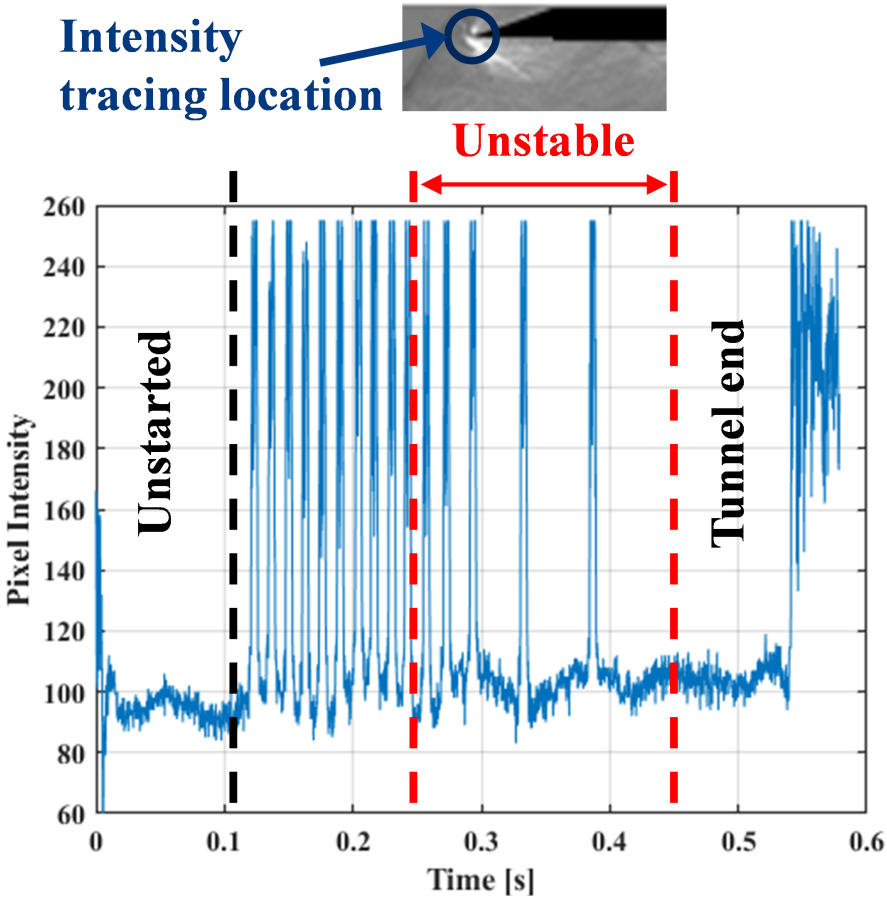

Fig. 4.4 Oscillatory flow motion after unstart: inlet buzz

4.2.2 Unstarted Flows with Suction

Once an inlet is unstarted, the mass imbalance is not immediately resolved since the accumulated mass still resides in the flow path. As a consequence, the inlet is not re-started soon even though the mass injection rate is still lower than the unstart threshold. Since unstart inlets cannot produce any thrust but increase drag resulting in dire problems in vehicle control, unstart inlets must be re-started as soon as possible. Therefore, the hysteresis phenomenon in the

re-starting procedure indicates the fueling rate must be much lower than the unstart threshold to re-start the inlet without the aid of active control.

To investigate the effectiveness of boundary-layer suction control for unstarted flows, suction is activated concurrently with the pressure level switching at 255 ms. Without boundary-layer suction, an oscillatory flow was still observed until around t = 400 ms. However, with the suction flow, the inlet is restarted at approximately t = 300 ms (green dashed line in Fig. 4.5) and remains started until the end of the tunnel operation.

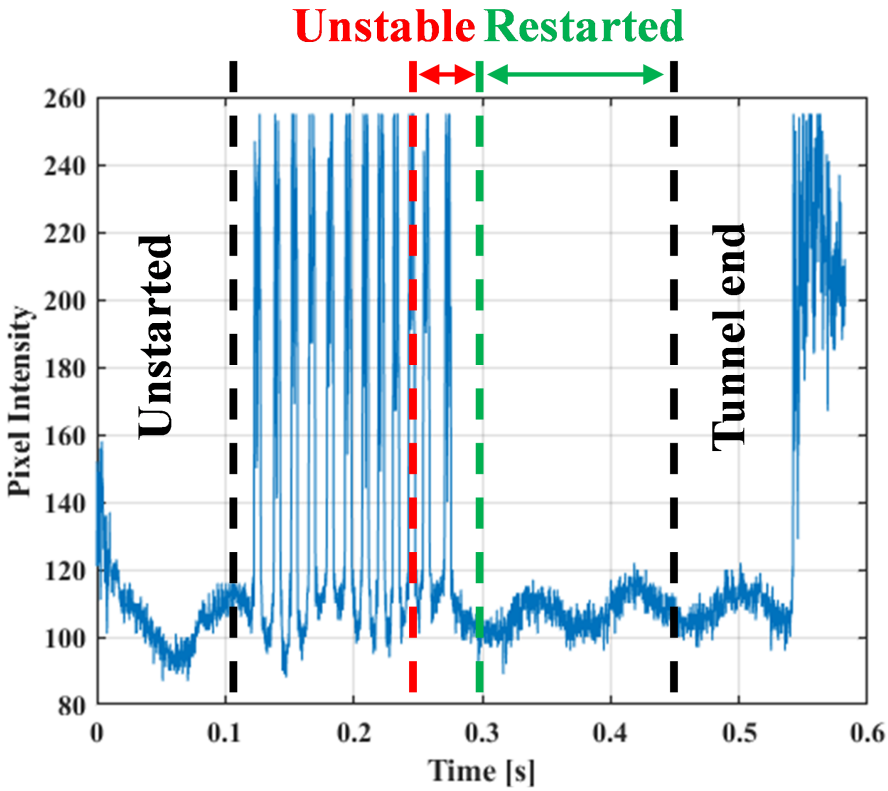

Fig. 4.5 Reduced inlet buzz frequency with boundary-layer suction control

4.3 Summary

Boundary-layer suction control for unstarted flow has been investigated. By an excessive jet injection, the inlet was almost immediately unstarted within a hundred milliseconds, showing an oscillatory flow motion at approximately 80 Hz after being unstarted. To simulate the re-starting process by fuel injection cut-off, the jet injection was cut to roughly 40 % of the unstarted value. Even though this pressure was below the unstart threshold, the inlet remains unstarted yet the buzz frequency was decreased. To evaluate the effectiveness of boundary-layer suction control, suction was triggered concurrently with the jet injection cut-off. It was turned out that the number of repetitions of the oscillatory motion after unstart was significantly reduced by suction, resulting in a faster re-start. Therefore, it could be concluded that boundary-layer suction is effective for re-starting the inlet.

Chapter 5

Boundary-layer Suction Control in High-Enthalpy Flows

In the previous sections of Chapter 3 and Chapter 4, it was found that boundary-layer suction control was effective for suppressing and delaying inlet unstart under low-enthalpy freestream flow conditions. Nevertheless, the mechanisms that trigger inlet unstart under cold conditions lack one of the key mechanisms: thermal choking under combustion environments. Therefore, the effectiveness of boundary-layer suction control is now investigated under high-enthalpy freestreams with fuel injections to provide more realistic unstarting conditions in this chapter. The key objective is to evaluate the effectiveness of the control in terms of delaying inlet unstart.

5.1 Experimental Configuration

5.1.1 Test Model

The test model used for the current investigations has the identical geometrical features shown in Chapter 3 (refer to Fig. 3.1). However, one of the quartz windows at the side of the inlet is replaced with another perforated plate to examine the effectiveness of boundary-layer suction control at a higher suction rate. The perforated plate installed at the side of the inlet has the identical hole distribution and size to the upper one (see Fig. 3.2). Although the size and the spacing of the holes are identical, the perforated plate for the sidewall has one more column (13 in a row, 7 in a column), the total number of the holes being 91. The first hole on the perforated plate at the upper wall is at x/L = 0.235. The first column of the holes on the side plate starts at x/L = 0.128. Because the perforated plate at the sidewall is installed on the side of the inlet ramp, 13 holes at the bottom are partially or completely blocked by the inlet ramp.

The cases are designated as "single-suction" when only the perforated plate at the upper wall in the isolator is used for driving suction flows. When two perforated plates are activated concurrently, the cases are designated as "double-suction" which extracts approximately double the suction rate than in the single-suction cases.

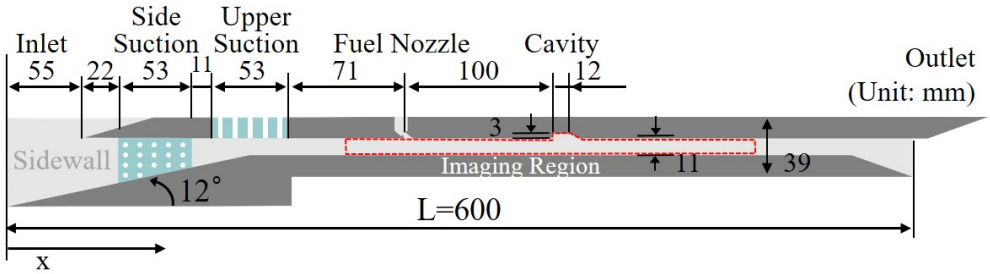

Fig. 5.1 Schematic of the model scramjet for high-enthalpy flows

5.1.2 Test rig

Experimental investigations are performed using an arc-heater wind tunnel ACT-1 in the university of Notre Dame to examine the effectiveness of boundary-layer suction control under high-enthalpy flow conditions. To provide more realistic flow conditions for the combusting environment, the arc-heater is turned on targeting the freestream total temperature to be around 2,400 K. Pure nitrogen goes through the arc-heater and then mixed with the nitrogen-oxygen mixture to provide a mixture of 80 % nitrogen and 20 % oxygen. This bypassing technique is utilized to minimize NOx generation from the arc-plasma. This mixture is then supplied to a plenum and a convergent/divergent (C/D) nozzle. The C/D nozzle used in this study has a diameter of 60.5 mm, aiming for uniform and clean Mach 4.5 freestream flows. Note that the freestream Mach number is decreased from 6 (for cold flow) to 4.5 in the current section to facilitate mode transition to inlet unstart mode. The total pressure of freestream flow is monitored by a high-temperature pressure transducer (Kulite, XTEL-190(M)) and the total temperature is estimated using ideally-choked relations at the throat of the C/D nozzle with known mass flow rates from the supply tank. Ethylene at room temperature (assumed to be constant at 294.15 K) is injected into the

combustor region to shock-induced ignition and subsequent combustion reactions, which would incur thermal choking when the ethylene injection rate is high enough. A vacuum tank of 2.1 L is installed for driving suction flows whose pressure is monitored by a miniature pressure transducer (Kulite, XCE-062). The openings of ethylene jet flow and suction flow are controlled by fast-acting solenoid valves (Parker 7121KBN2NF00) and the total pressure of the ethylene jet is monitored using a heavy-duty pressure transducer (Honeywell PX2).

Quartz windows are installed at both sides of the wind tunnel which enabled optical access to the internal flow. Therefore, fast CH* chemiluminescence imaging is performed to capture the behavior of flames under unstarting conditions. A narrow bandpass filter centered at 430 nm (Edmund Optics, filter BP 430NM X 10 nm OD4 50 mm) is installed in front of a high-speed camera (Photron FASTCAM SA4) to capture the flame dynamics at 12,000 frames per second.

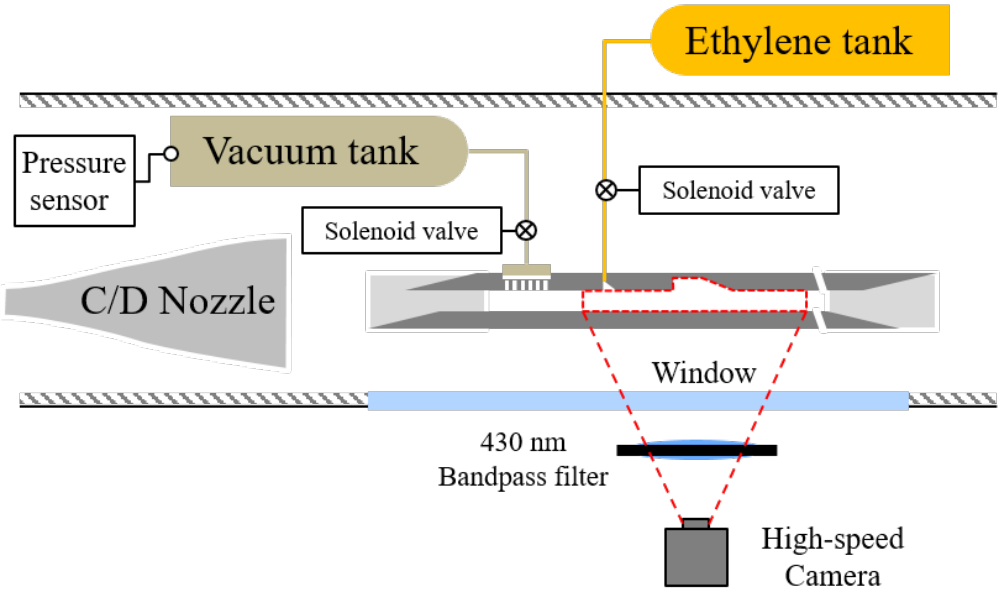

Fig. 5.2 Schematic of the model scramjet for high-enthalpy flows

One of the primary goals of the research is to identify any precursor to inlet unstart. The precursor should be related to measurable flow variables and detected as early as possible to delay or suppress inlet unstart. Thus, wall pressures are recorded along with the CH* imaging since accurate and high-sampling pressure measurements can be achieved relatively easily with minimal disturbance to the flow. Four at the upper wall and six at the lower wall, a total of ten pressure transducers (Kulite, XCE-062) are recess-mounted at the center-span of both the upper and the lower walls, as depicted in Fig. 5.3. The sensors are denoted either as "U" or "L" if they are located at the upper wall or lower wall, respectively, with their orders in their stream-wise distances from the leading edge of each wall.

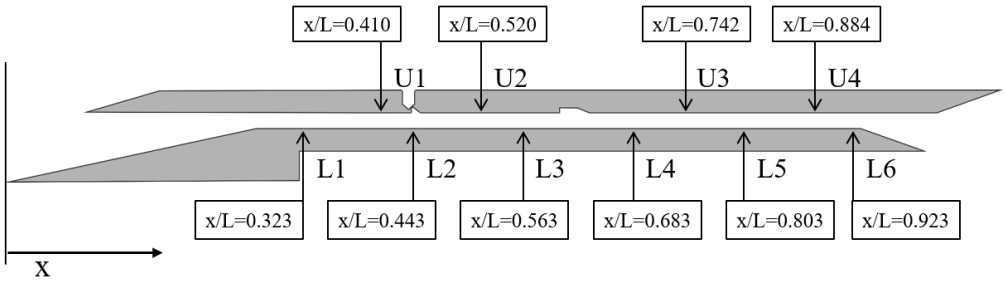

Fig. 5.3 Pressure sensor locations

Critical tunnel operation parameters for the current setup are presented in Fig. 5.4. The horizontal axis represents the time after the freestream trigger. The fuel jet is injected approximately 80 ms after the freestream trigger. All the profiles are normalized by their respective time averages in the interval of 0.12 s – 0.48 s when every curve shows a plateau.

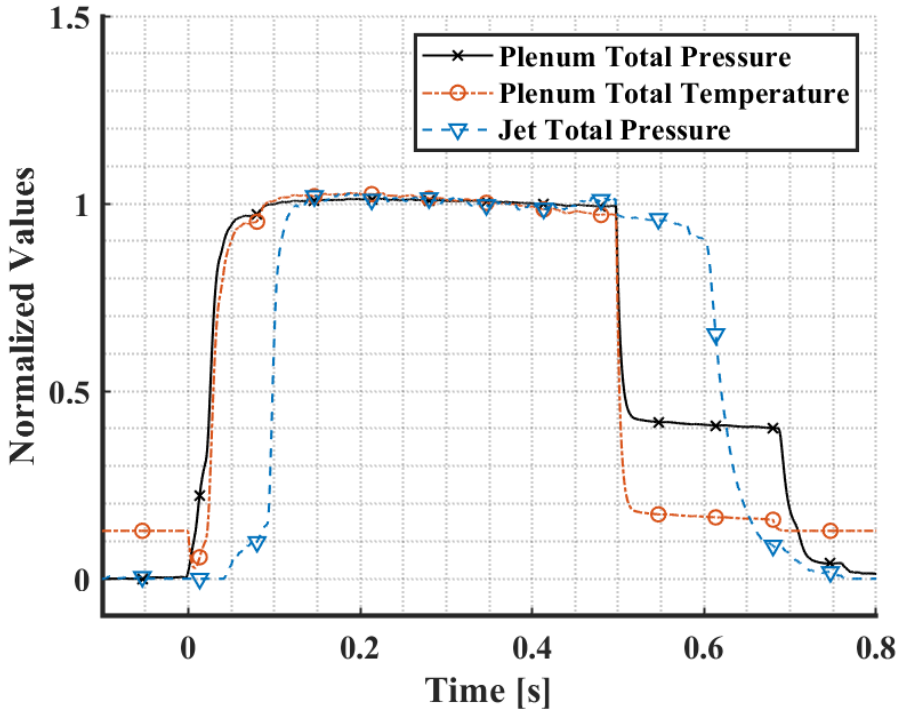

Fig. 5.4 Critical tunnel parameters for high-enthalpy flows

5.1.3 Experimental Conditions

Five sets of experiments are conducted in this study. The first set is the reference cases to investigate the operational mode of the model dual-mode scramjet, which is denoted as "R" in their designations (R01 – R07). At low overall equivalence ratios (ϕ), the model scramjet was operating in ram mode. However, when the ϕ was increased enough, a mode transition from ram-mode to unstart mode was observed, which will be shown in the following section. It was found that this transition, or the unstart threshold equivalence ratio is around 0.39 in the current setup. The second set, which is denoted as "N", is non-suction cases at slightly (approximately 10%) higher equivalence ratios

than the unstart ϕ-threshold, being at 0.45 (N01) and 0.49 (N02), respectively. The third and the fourth set of experiments are single- and double-suction cases with different activation delays as opposed to the reference non-suction cases, denoted as "S" (S01 and S02) and "D" (D01 – D03), respectively. The final set of the experiment is non- (N11), single- (S11), and double-suction (D11) cases at a higher ϕ (approximately 70 % higher than the unstart ϕ-threshold) to examine the effectiveness of boundary-layer suction control at higher mass imbalance rate.

The corresponding test matrix is presented in Table 5.1. The freestream total pressure and total temperature are averaged over the time intervals of 0.12 – 0.48 and presented along with errors in the 95 % confidence interval. The overall equivalence ratio (ϕ) and MCR are estimated with instantaneous freestream mass flow rate and jet mass flow rate which are again time-averaged over the aforementioned interval. Because of the uncertainties in tunnel operation parameters, ϕ has an uncertainty of approximately $\pm$ 2.5 %, varying $\pm$ 0.011 on average.

Boundary-layer suction is triggered relative to the jet trigger signal as tabulated in the last column of Table 5.1, "dtS"; for example, + 5 indicates boundary-layer suction was triggered 5 ms after the jet injection trigger. For those suction activated cases, the pressure traces of suction pressure is presented in Fig. 5.5. The suction pressures are non-dimensionalized with the freestream static pressure, the nominal freestream specific heat ratio ($\gamma = 1.4$), and the nominal freestream Mach number. The suction activation delay is defined as the period for suction pressure to reach twice the initial pressure level, which is 30 ms on average over the cases.

The suction mass flow rate is estimated via the ideal gas law, assuming constant temperature in the vacuum tank, which is then normalized by the captured

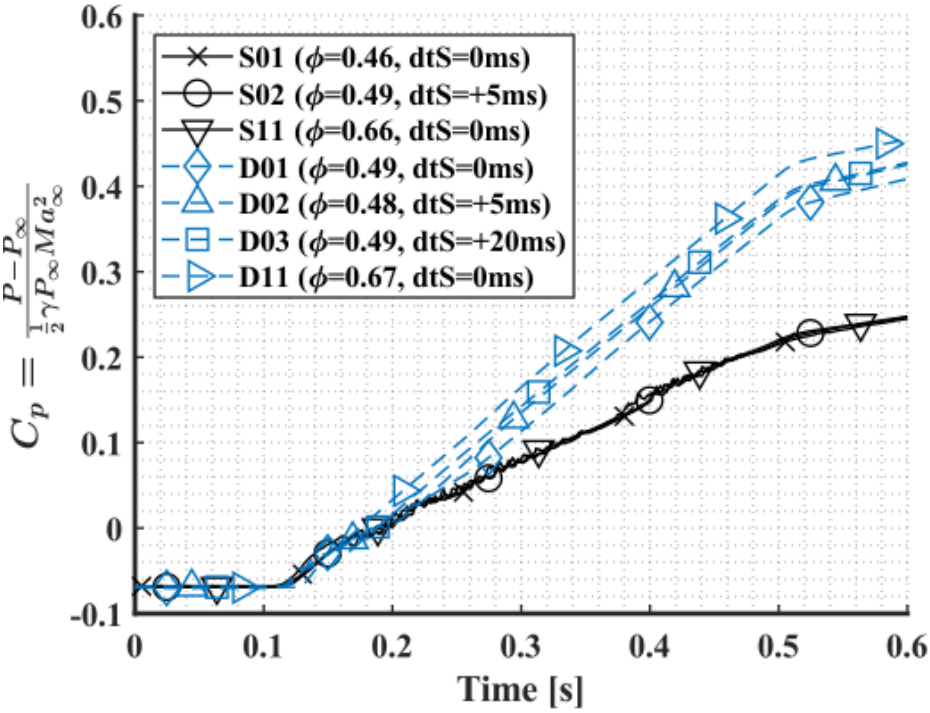

Fig. 5.5 Suction pressure traces

flow rate at the inlet to obtain "Suction Mass" in Table 5.2. The suction masses are fairly constant in both single- and double-suction cases at around 1.2 % and 1.9 %, respectively, regardless of the overall equivalence ratio. Furthermore, the pressure traces in Fig. 5.5 show almost linear profiles throughout the cases, showing that the vacuum tank of 2.1 L is big enough to maintain the pressure inside unchanged to drive suction flow at a nearly constant rate. Moreover, it could also imply that the holes in the perforated plates are choked to result in a constant suction rate.

Table 5.1 Test matrix for high-enthalpy flows

Designation	Freestream properties			ϕ	MCR	dtS, ms[1]
	Ma	P_{0f}, kPa	T_0, K			
R01	4.5	94.6 ± 0.58	2360 ± 32	0.00	1.063	N/A [2]
R02	4.5	94.6 ± 0.58	2360 ± 32	0.14	1.072	N/A
R03	4.5	94.6 ± 0.58	2360 ± 32	0.18	1.076	N/A
R04	4.5	94.6 ± 0.58	2360 ± 32	0.28	1.082	N/A
R05	4.5	94.6 ± 0.58	2360 ± 32	0.38	1.089	N/A
R06	4.5	94.6 ± 0.58	2360 ± 32	0.39	1.090	N/A
R07	4.5	94.6 ± 0.58	2360 ± 32	0.40	1.090	N/A
N01	4.5	94.6 ± 0.58	2360 ± 32	0.45	1.094	N/A
N02	4.5	94.6 ± 0.58	2360 ± 32	0.49	1.096	N/A
S01	4.5	94.6 ± 0.58	2360 ± 32	0.46	1.094	0
S02	4.5	94.6 ± 0.58	2360 ± 32	0.49	1.097	+5
D01	4.5	94.6 ± 0.58	2360 ± 32	0.49	1.096	0
D02	4.5	94.6 ± 0.58	2360 ± 32	0.49	1.095	+5
D03	4.5	94.6 ± 0.58	2360 ± 32	0.48	1.096	+20
N11	4.5	94.6 ± 0.58	2360 ± 32	0.67	1.108	0
S11	4.5	94.6 ± 0.58	2360 ± 32	0.66	1.108	0
D11	4.5	94.6 ± 0.58	2360 ± 32	0.67	1.108	0

[1] Suction trigger relative to the jet injection trigger.

[2] N/A denotes "not applicable".

Table 5.2 Suction mass flow rate ratios

Case	S01	S02	S11	D01	D02	D03	D11
Suction Mass, %	1.2	1.2	1.2	1.8	1.9	1.9	2.0

5.2 Test Results

5.2.1 Ramjet Mode

The structure of the pre-combustion shock train (PCST) in a dual-mode scramjet varies depending on the backpressure level inside the combustor. If the mass injection rate and the pressure rise from the combustion reaction are sufficiently smaller for the core flow to overcome, the PCST is weak and the internal flow remains supersonic to operate the combustor as scramjet mode. If the mass injection rate and backpressure rise increases, the PCST becomes stronger to compensate for the pressure rise, eventually leading to a strong normal shock in the isolator region. Under this operational mode, the flow downstream at the combustor is subsonic and the combustor must operate in ramjet mode. When the mass injection rate and the backpressure rise further increase, another strong shock system is formed to unstart the whole internal field; this is called unstart mode.

Since the fueling rate is closely related to the operational mode in a dual-mode scramjet, the overall equivalence ratio is increased from 0 (R01) to around 0.38 (R05) to identify the operational modes. Typical pressure distribution along the stream-wise direction for R01 – R05 is plotted in Fig. 5.6. The horizontal axis represents the distance from the leading edge of the lower wall (x/L). The vertical axis represents pressure coefficients estimated with the nominal specific heat ratio of the freestream ($\gamma = 1.4$), freestream static pressure (P_∞), and the nominal freestream Mach number ($Ma_\infty = 4.5$). Two vertical black dashed lines show the locations of the jet and the flameholder cavity, respectively. Typical errors associated with measurement uncertainties are denoted as error bars at each point; the average of uncertainties was roughly 3.7 %. The corresponding sensor locations are represented in the schematic of the model dual-mode

scramjet at the top of the figure. When the jet is not injected (R01), the pressure distribution shows a relatively gradual increase until reaching L3, which slightly falls afterward. It is noteworthy that a pressure coefficient of approximately 1.6 corresponds to a pressure level downstream of a strong normal shock at Mach 4.5. Since the pressure coefficients in all locations are smaller than 1.6 in R01, it could be concluded that the internal flow remains supersonic in this case.

However, as the fuel is injected (R02), the pressure coefficient near the jet injection point (near U1 and L2) increases significantly, exceeding 1.6 to reach maximum although the pressure level at L1 stays almost constant. This implies that the high mass injection rate and subsequent combustion reaction incur a stronger PCST system, forming a stronger shock system to turn the internal flow subsonic. The pressure coefficients downstream of the jet injection points slowly decrease in the stream-wise direction, indicating the flow is accelerating under subsonic combustion: this inverted "V" shape pressure profile is typical in ram-mode operation.

If the overall equivalence ratio is further increases (R03 – R05), even the pressure level at L1 increases as well, remaining an inverted "V" shape profile. This pressure increase at L1 shows the strong shock system is now located further upstream of L1 due to a higher backpressure level from a higher fueling rate: the higher the backpressure level, the further the shock moves upstream to compensate for the pressure rise.

CH* chemiluminescence imaging is conducted to investigate the behavior of the flame corresponding to the changes in the pressure profile changes seen in Fig. 5.6. CH* is an intermittent species that only exists for a short time in the reaction zone which makes CH* a good indicator for identifying the combustion zone. Nevertheless, the flame and the flow show highly fluctuating both in time and space. Thus, the CH* images obtained from 100 ms to 125 ms are aver-

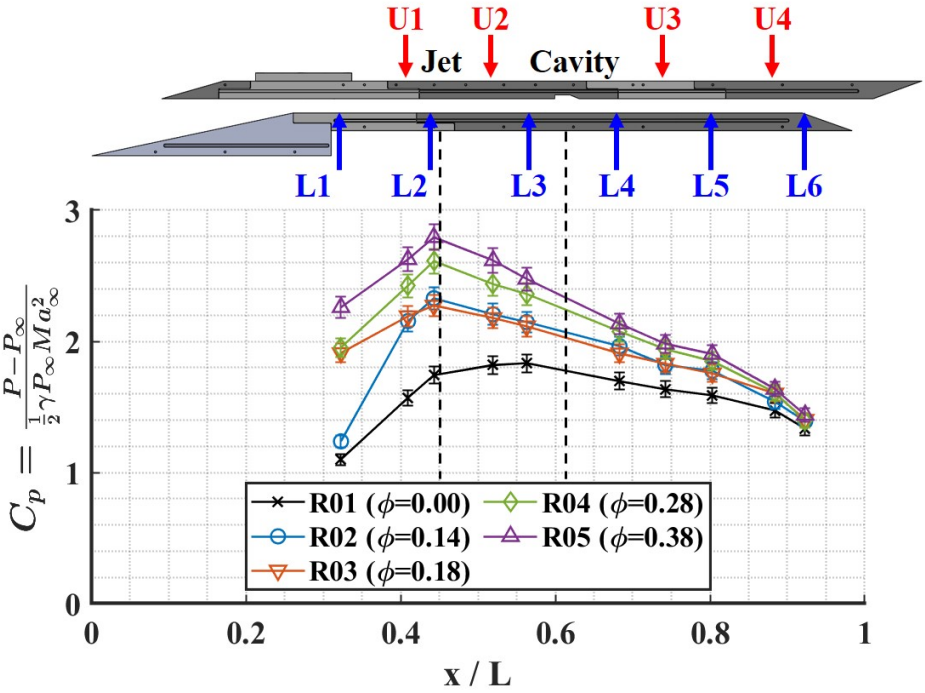

Fig. 5.6 Wall pressure traces for the reference cases at t=100ms

aged to show more general behavior of the flame. For R02 00 R05, the mean and the standard deviation of CH* intensity within the interval of 100 – 125 ms are presented in Fig. 5.7. Vertical grey arrows indicate the location of the jet injection point. The blacked regions between the jet injection point and the flameholder cavity are due to a structure that blocked the chemiluminescence. The averaged mean and the standard deviation are normalized by their respective maximum values throughout the cases and presented in an arbitrary unit (A.U.). When the overall equivalence ratio is low, the flame is relatively short and terminated near the flameholder cavity. As the equivalence ratio increases, the flame is further stretched to the downstream regions of the cavity in terms of both mean and standard deviation of the CH* images. However, the region of

maximum mean intensity does not agree with the region of maximum standard deviation. This implies that as the combustion rate increases, the fluctuation level increases as well, which is from flow mixing and acceleration from subsonic combustion. Therefore, it could be concluded that the operational mode until around $\phi = 0.38$ is a ramjet mode.

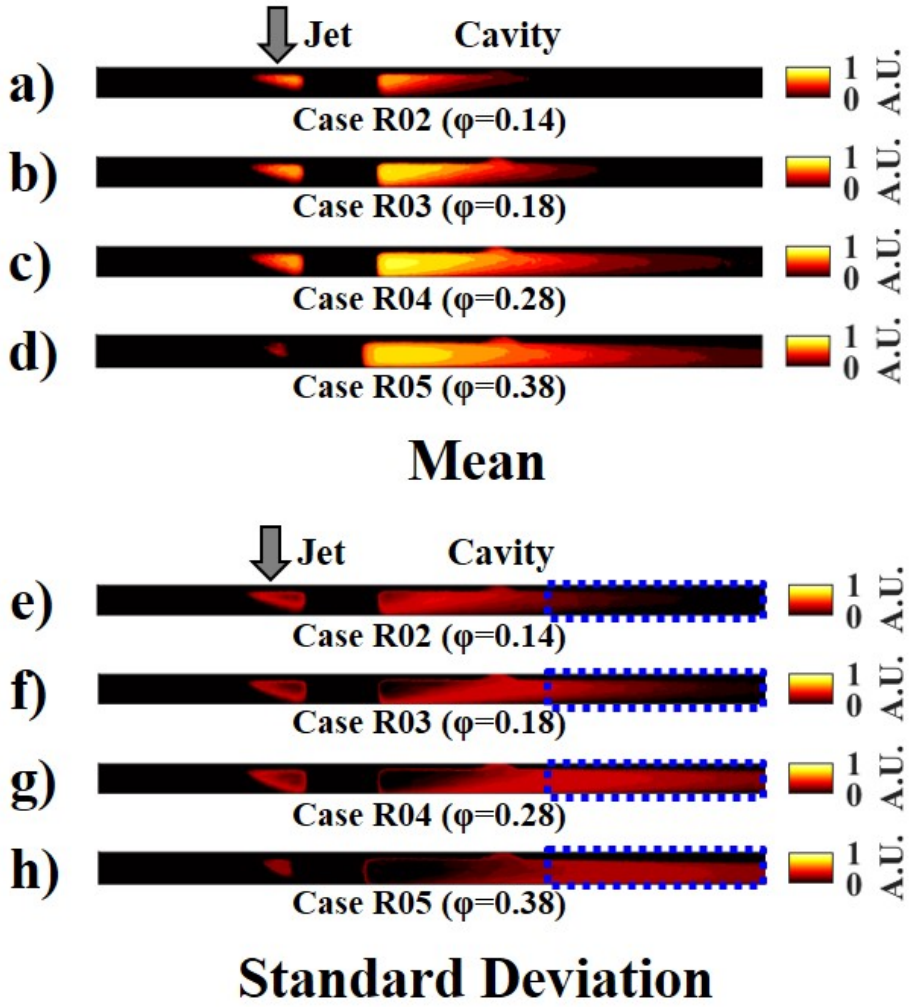

Fig. 5.7 Mean (top) and standard deviation (bottom) of CH* imaging intensities in R02 – R05

5.2.2 Unstart Mode

It was observed that the model dual-mode scramjet operates as ramjet-mode until around $\phi = 0.38$. To investigate the threshold of mode transition to unstart mode, the overall equivalence ratio is further increased to 0.4. The

pressure traces at sensor locations of U1, U2, L1, and L2 are plotted for reference cases in Fig. 5.8. R02 and R04 are excluded since those cases merely display half the pressure level between the adjacent ϕ cases, making them less meaningful than other cases. The abscissa represents the time after the freestream trigger whereas the order represents the pressure coefficient in Fig. 5.8. A low-pass filter of 50 Hz is applied to all pressure signals to illustrate more general behaviors in time where R01 being the reference case without the fuel injection. When the fuel is not injected (R01), pressures steeply rise around from 0 to 50 ms period after the freestream trigger and sustain the pressure level until the end of the tunnel operation at approximately 500 ms. The fuel jet is injected around 100 ms after the freestream trigger, which is illustrated sharp pressure increases in all locations. Moreover, pressures for R05 rise slightly steeper than for those in R03 to reach different pressure levels at the same time around 120 ms. If the overall equivalence ratio is further increased as in R06, the pressure rise around 100 ms, and the pressure level followed by this pressure rise is almost identical to those in R05. However, the pressures suddenly drop at approximately 450 ms just before the tunnel operation ends. Although there are a few milliseconds gap amongst different sensor locations, this drop is seen in all pressure sensor locations although not presented here. If the equivalence ratio is even further increased to 0.4 as in R07, this pressure drop is seen significantly earlier at around 180 ms after the freestream trigger.

The traces of the pressure sensors at the upper wall of the model (U1 – U4) is presented in Fig. 5.9 to investigate the transient flow behavior of unstarting flow in detail. Before the fuel jet injection (0 – 0.1 s period), U1 shows the lowest pressure level whereas U2 shows the highest. This is due to a strong PCST system existing in the isolator to compress the flow near U2. The flow is then accelerated via subsonic flow choking downstream of U2, shown as slight

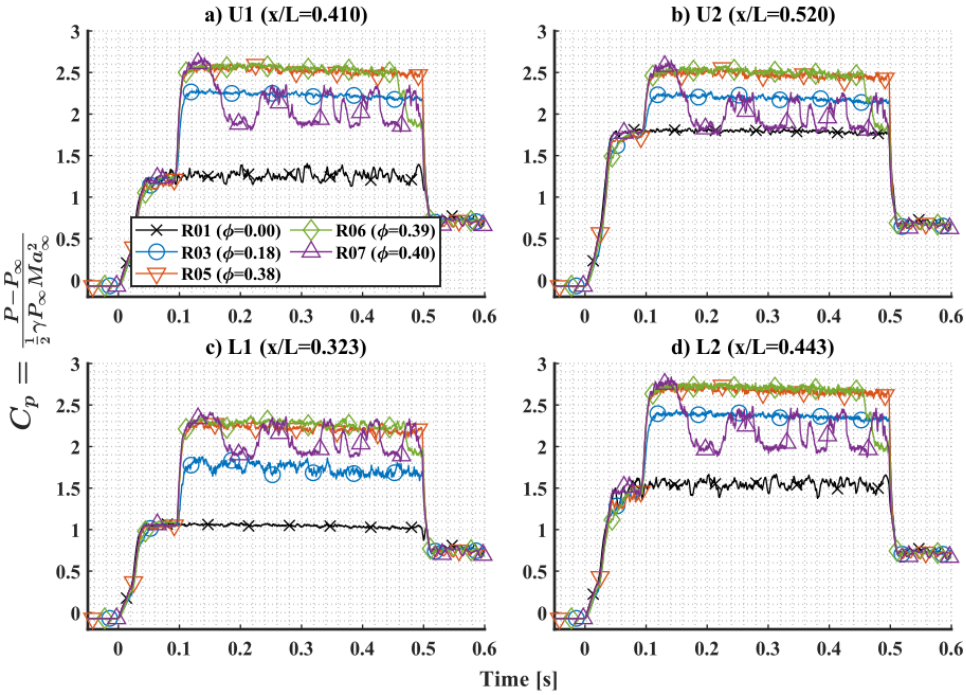

Fig. 5.8 Pressure traces at U1, U2, L1, and L2 in the reference cases

decreases in pressure coefficients at U3 and U4. When the fuel jet is injected, the pressures at U1 and U2 increase significantly and reach a comparable pressure coefficient at around 2.5. The similar pressure levels exceeding 1.6 at U1 and U2 indicate a strong shock system is now upstream of U1 (and also U2) to operate the model dual-mode scramjet in a ramjet mode. As a consequence of subsonic combustion and subsequent flow acceleration, pressure coefficients at U3 and U4 are smaller than those at U1 and U2. The pressures are almost held constant until around 450 ms for all locations. However, at around 454 ms, pressures at all locations suddenly start to fall. This decrease of pressures indicates the upstream propagation of the PCST system due to the mass imbalance. Then, the pressures momentarily surge within 10 ms, highlighted as a red vertical

arrow. It is conjectured that this surge corresponds to the arrival of unstart shock at the throat of the inlet, merging with the pre-existing shock systems to further decelerate the flow. After this surge, the pressures continue to drop until approximately 480 ms.

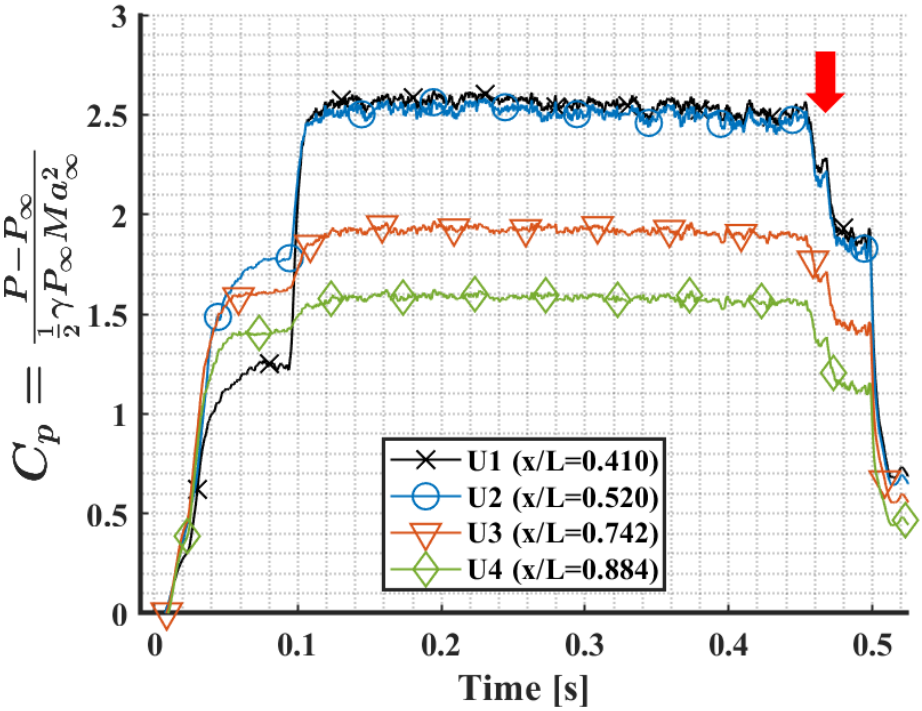

Fig. 5.9 Upper wall pressure traces in R06

Lower wall pressure traces are collected and presented in the same manner in Fig. 5.10. Before the jet injection, the pressure at L1, which is located the most upstream, exhibits the lowest pressure level whereas L3 shows the highest. L2 is around half-way between L1 and L3. The sensors downstream of L3 (L4 – L6) shows gradually decreasing pressure coefficients along the stream-wise direction. These behaviors (C_p being maximum at around x/L = 0.5, slightly decreasing

downstream) are consistent with the upper wall's results presented in Fig. 5.9. After the ethylene jet is injected, the pressure at L2 increases the steepest and reaches the highest pressure coefficient level amongst all the locations at around 2.8. This is because L2 is located almost the right opposite side of the jet, undergoing the most significant pressure rises from supersonic bow shock, mixing, and combustion due to the jet injection. Moreover, it is noteworthy that the pressure coefficient at L1 is even greater than 1.6 (subsonic pressure level). This implies that a strong shock system exists upstream of the L1 (near the throat of the inlet). The pressures downstream of L3, L4 – L6 show decreasing profiles along the stream-wise direction owing to the flow acceleration from subsonic frictional/thermal choking. Furthermore, the pressure coefficient at L6 is smaller than 1.6, indicating there exists a fluid choked throat between the locations of L5 and L6. As seen in the upper wall case, the pressure levels are maintained until around 450 ms but start to drop abruptly. Again, simultaneous pressure surges over all the sensor locations are observed at around 460 ms, denoted as a red vertical arrow.

The pressure profiles in R06 at different time instances are presented in Fig. 5.11 to better illustrate the temporal and spatial evolution of the flow during the ram-to-unstart mode transition. The five-time instances correspond to i) just prior to the pressure drop (t = 450 ms), ii) right after the pressure drop (t = 456 ms), iii) during the first pressure dropping period (t = 462), iv) at the pressure surge moment (t = 468 ms), and v) near the end of the second pressure dropping period (t = 475 ms), respectively. Before the pressure drop (t = 450 ms), the pressures show a clear inverted "V" shaped profile as seen in other reference cases with lower ϕ (refer to Fig. 5.6). However, as the jet injection continues, the pressures start to decrease at around 456 ms except for at L1. Note that the pressure at L1 is nearly unchanged from t = 450 ms to t =

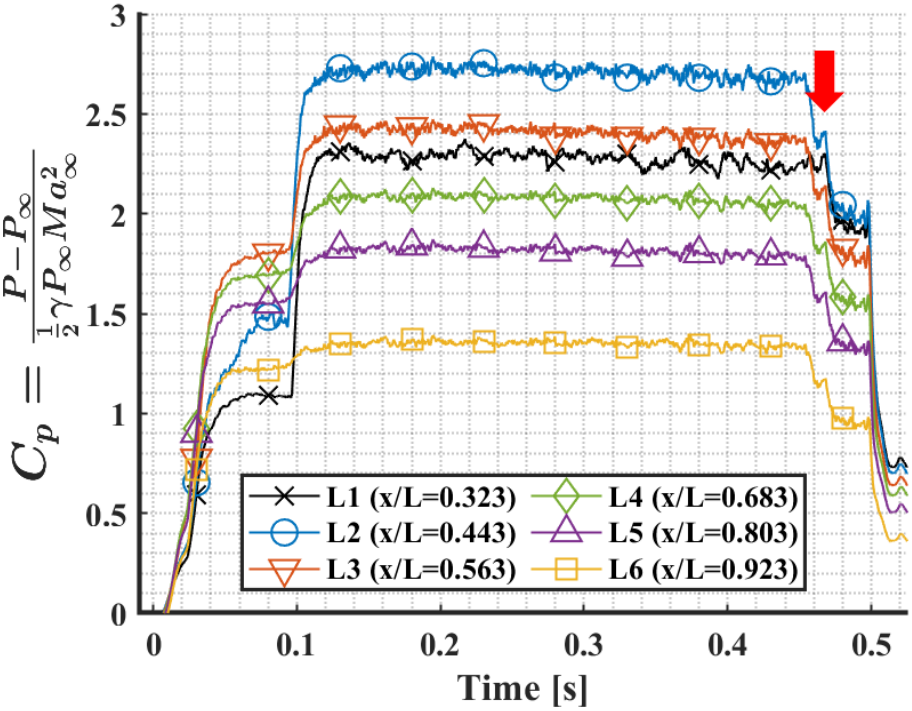

Fig. 5.10 Lower wall pressure traces in R06

462 ms, where pressures at other locations continue to fall, making the profile flatter across L1, U1, and L2. When at t = 468 ms, pressures at all locations, including L1, slightly increase depicted as momentarily surges in Fig. 5.9 or Fig. 5.10, which could be from the arrival of unstart shock system to the inlet's throat. After the completion of inlet unstart, pressures are at significantly lower levels before unstarted. Moreover, The profiles across L1, U1, and L2 remain almost flat indicating the flow is subsonic. However, the jet injection is continued to conduct subsonic combustion at some degree downstream of L2, showing a decreasing pressure pattern along the stream-wise direction.

Short-time Fourier transform (STFT) is performed for pressure traces in

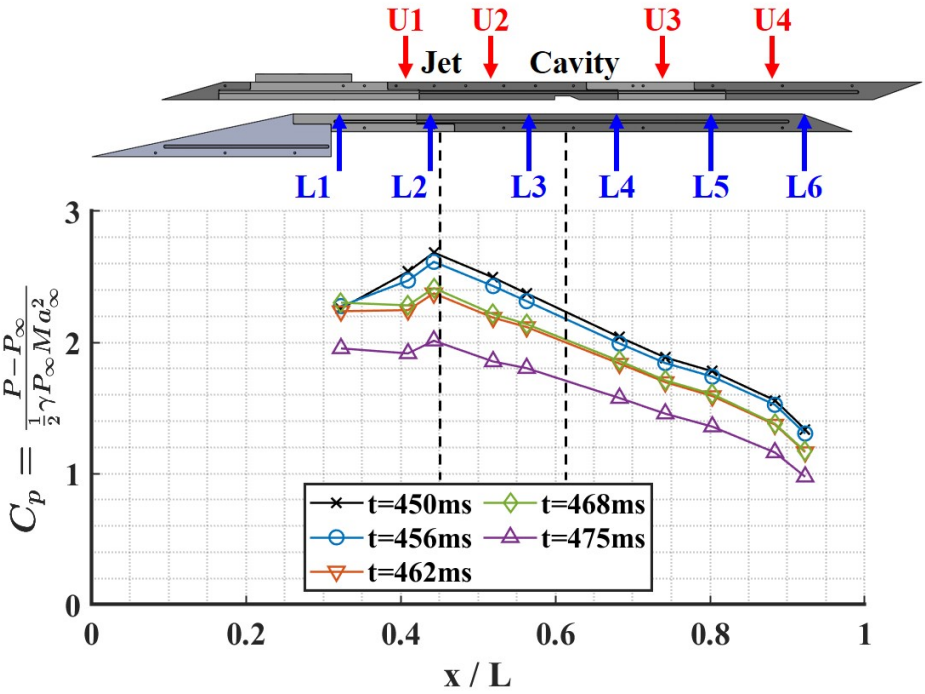

Fig. 5.11 Wall pressure distributions in R06 from t = 450 – 475 ms

reference cases to investigate and capture the changes in the frequency domain depending on the operational mode. A Hamming window of 385 points is used and 192 adjacent samples are overlapped. The x-axis of each figure represents the time relative to the freestream trigger, while the y-axis is each frequency component. The contour level denotes power spectrum density (PSD), normalized by own frequency.

Firstly, the STFT spectrogram at L1 is presented in Fig. 5.13 which is located the most upstream. The spectrogram for R04 is omitted here since it displays behaviors merely half-way between R03 and R05. R01 is the reference case without the fuel jet injection and shows only strong low-frequency components below 5 Hz (Fig. 5.13(a)). As the jet is injected, higher frequency components start

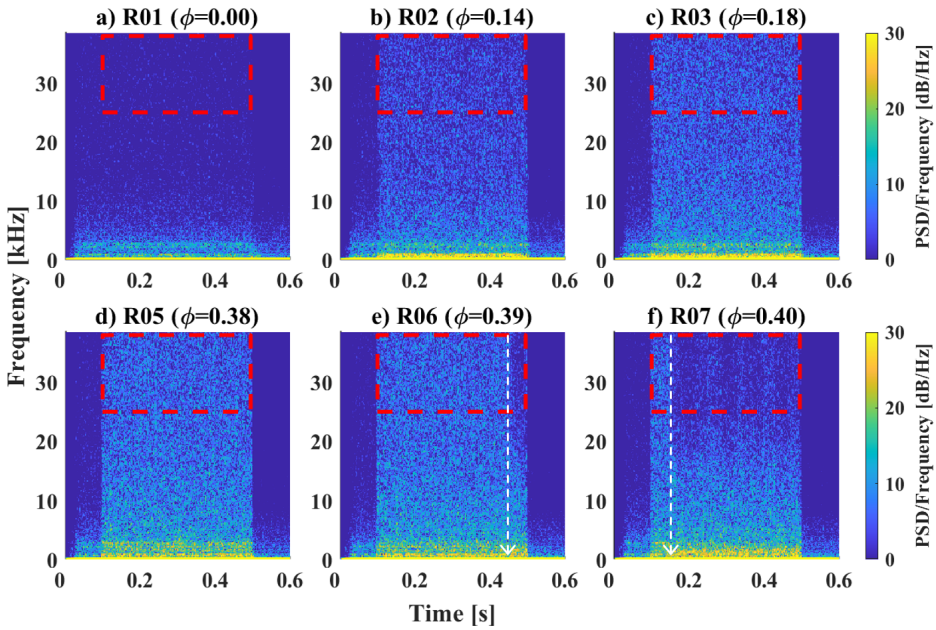

Fig. 5.12 STFT spectrogram at L1 (x/L=0.323) for reference cases

to appear, and the power becomes stronger with higher equivalence ratios until $\phi = 0.38$ (see Fig. 5.13(b) – (d)). However, at $\phi = 0.39$ (R06), high-frequency components suddenly start to become weaker, denoted as a white vertical arrow in Fig. 5.13(e). The diminish is more drastic in the frequency components above 20 kHz, as highlighted as dashed red boxes in each figure. Moreover, this timing of power reduction in the frequency domain is coincident with the pressure drops seen in Fig. 5.9 and Fig. 5.10. If the equivalence ratio is slightly increased to $\phi = 0.4$ as in R07, this diminishment is observed significantly earlier at around 160 ms, which also agrees with the pressure drop in this case (refer to the pressure drop in Fig. 5.8).

In the same manner, the STFT spectrogram at L2 is presented in Fig. 5.14 for reference cases. Even though that the general trend is almost the same as

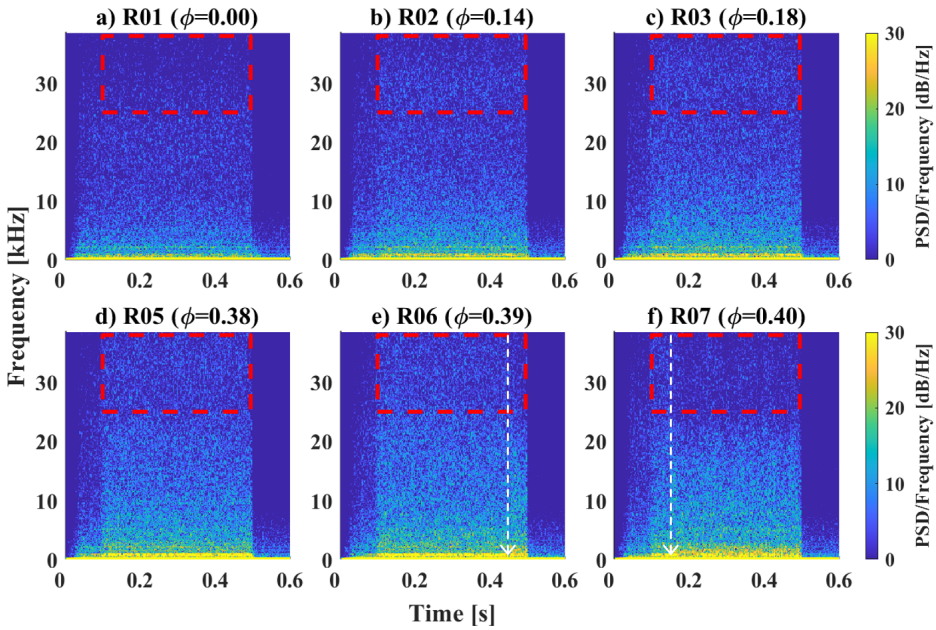

Fig. 5.13 STFT spectrogram at L2 (x/L=0.443) for reference cases

observed at L1, the mean power of the jet-induced frequency components ($>$ 5 Hz) is weaker whereas the low-frequency component remains comparable ($<$ 5 Hz). Moreover, although not presented here, STFT results at other locations (L3 – L6, and U1 – U4) show even weaker PSDs and less prominent changes after the unstart. This is because boundary-layers become thicker traveling downstream, acting as a buffer region for pressure fluctuations. Nevertheless, it could be concluded that pressure measurements reveal that an abrupt drop of pressure magnitude and high-frequency fluctuation PSD can be regarded as the precursor or the sign of the unstart process.

To investigate the flame behavior related to the pressure measurement results, CH* chemiluminescence imaging is performed for R05 in Fig. 5.15. The instantaneous images are averaged over a 25 ms of interval and four-time in-

stances are selected; i) t = 100 ms, ii) t = 200 ms, iii) t = 300 ms, and iv) t = 400 ms to illustrate the temporal and spatial evolution of the flame. R05 is the highest equivalence ratio case without inlet unstart. As a result, a stable subsonic ramjet mode combustion is shown: the flame is stretched long downstream and the mean CH* intensities are almost constant over time. Interestingly, the standard deviations of CH* images are very high just downstream of the flameholder cavity, as highlighted as blue dashed boxes (Fig. 5.14(e) – (h)).

Similarly, CH* chemiluminescence images for R07 over the aforementioned time interval are presented in Fig. 5.15. R07 is the case where the inlet is unstarted almost immediately after the jet injection, at around 160 ms. Therefore, at t = 100 ms, CH* images show the same features of stable ramjet operation as seen in R05, although the magnitudes of the mean and standard deviation of CH* intensities are slightly increased (compare Fig. 5.14(a), (e) and Fig. 5.15(a), (e)). However, after being unstarted, the mean and the standard deviation of the CH* intensities decrease (Fig. 5.14(b) and (f), respectively). The reduction of magnitudes in terms of the standard deviation is more significant especially downstream of the cavity (Fig. 5.14(f), blue dashed box), and it agrees with the diminish of high-frequency components after unstart. It is interesting to note that the mean and the standard deviation increase back to the pre-unstart level at around 400 ms. This is due to inlet buzz phenomenon that temporarily starts the inlet to some extent (refer to Fig. 5.8).

In summary, ram-to-unstart mode transition was presented in this section. Pressure measurements at the walls and flame visualization were conducted to investigate and quantify the behavior of unstarting flows. It was confirmed that inlet unstart is a highly transient and abrupt phenomenon. The start of unstarting flow was displayed as a sharp drop in pressure magnitudes, a diminish of high-frequency component pressure fluctuations, and less variations in CH* con-

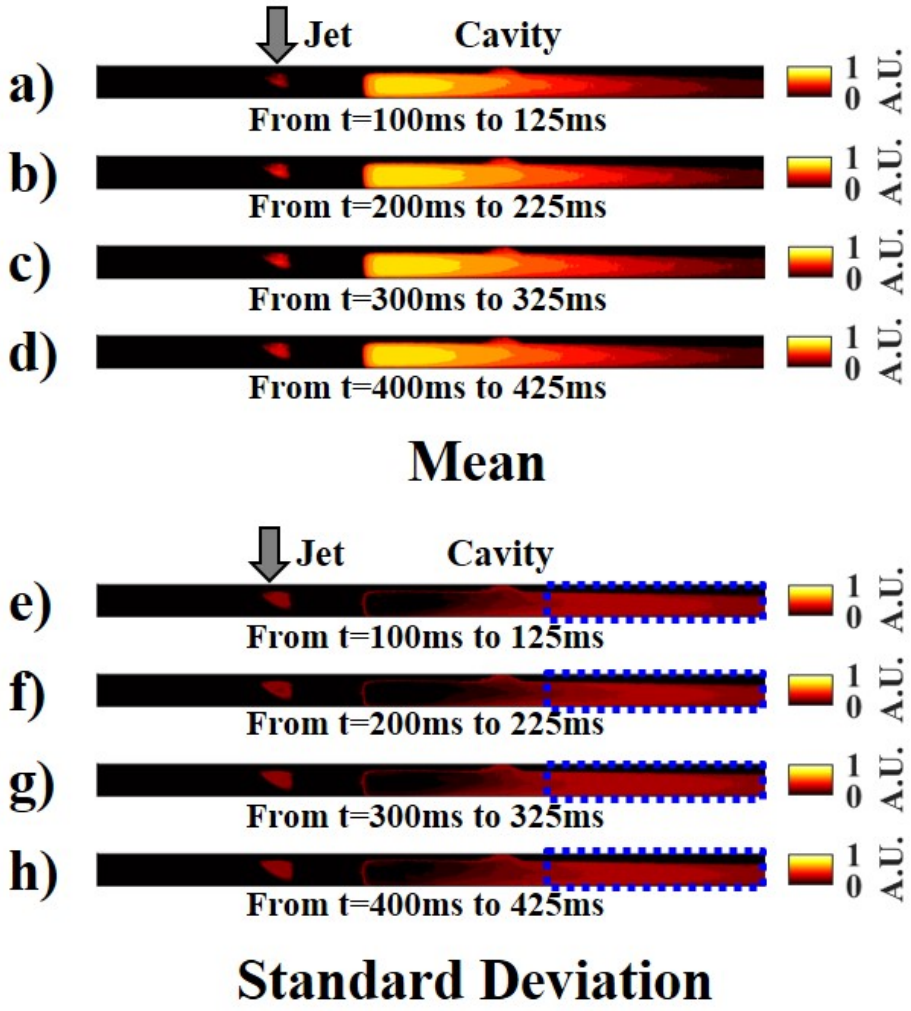

Fig. 5.14 Mean (a – d) and standard deviation (e – h) of CH* images in R05

centration. This change was a very abrupt one, taking only a few milliseconds. Therefore, it could be concluded that the initiation and the termination are important parameters to quantitatively characterize and to understand unstarting flows. Thus, two unstart indicators are selected and used in the following chapters: an abrupt pressure drop at L2 and high-frequency pressure fluctuations at

L1. The termination or the completion of the inlet unstart process is conjectured to be at or around the pressure surge point after the first abrupt pressure drop (see Fig. 5.9 and Fig. 5.10). Furthermore, the threshold of inlet unstart in terms of the overall equivalence ratio (unstart ϕ-threshold) is assumed to be between 0.38 and 0.39, as an abrupt pressure drop was first seen in this regime (refer to Fig. 5.8).

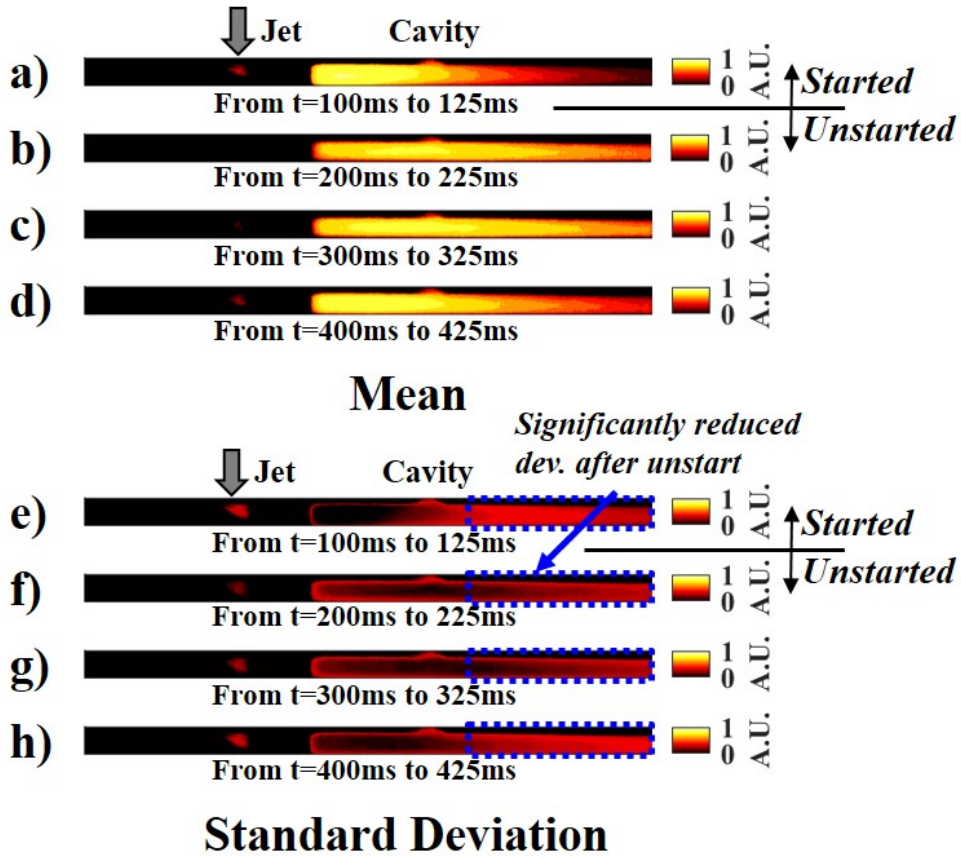

Fig. 5.15 Mean (a – d) and standard deviation (e – h) of CH* images in R07

5.2.3 Non- and Single-Suction Cases

In the previous section, the unstart ϕ-threshold was assumed to be around 0.39. The overall equivalence ratio is increased by approximately 15 – 25 % than the ϕ-threshold to simulate more realistic unstarting conditions for the model. Two non-suction cases at different equivalence ratios at ϕ = 0.45 (N01) and ϕ = 0.49 (N02) are selected as the comparative cases for the suction cases. Single-suction, that is, activating only the perforated plate at the upper wall in the isolator is tested in this section. Consequently, suction flow at approximately 1.2 % of the corresponding freestream flow rate could be removed from the boundary-layer. Two single-suction cases at two overall equivalence ratios at ϕ = 0.46 (S01), and ϕ = 0.49 (S02) are selected and compared to the equivalence non-suction cases correspondingly in terms of ϕ. For S01, suction is triggered concurrently with the jet injection whereas for S02 the activation is delayed by 5 ms.

The pressure traces at L2 for non- and single-suction cases are plotted in Fig. 5.16. The abscissa is the time after the freestream trigger. The order represents the pressure coefficient after 50 Hz low-pass filtering. R07 is also included as an illustrative example of the near-threshold unstarting flow. Due to the exceedingly higher equivalence ratio than the threshold, the initiations of unstart are seen at around 121 ms and 110 ms for N01 and N02, respectively. This is markedly earlier than 150 ms in R07. Inlet unstart takes approximately 17 ms for N01 and 12 ms for N02, respectively, and hence completion being at around 138 ms and 133 ms for N01 and N02, respectively. After the unstart completion, pressures in both N01 and N02 show periodic repeats between two pressure levels which is inlet buzz. The estimated buzz frequency is approximately 18 Hz for both cases.

To investigate the effectiveness of the boundary-layer suction, suction is first activated simultaneously with the jet injection trigger. When the suction is triggered in this manner as in S01, the unstart initiation is observed at roughly 156 ms, which is approximately 34 ms later than that in the equivalent non-suction case (N01). However, inlet unstart takes place faster with the suction, taking only 12 ms in this case. Moreover, the inlet buzz frequency is significantly reduced to 8.8 Hz, which is approximately half of that for N01 (Fig. 5.16(a)).

Suction is triggered 5 ms after the jet injection trigger to examine the effectiveness of the boundary-layer suction control with delays. The suction mass is kept constant at approximately 1.2 % of the freestream. Despite the suction flow, however, the pressure trace at L2 for the single-suction case (S02) is almost identical to the equivalent non-suction case (N02), its initiation being at around 114 ms: only 4 ms delay than in N02. The completion is at around 127 ms, taking 13 ms. Moreover, the buzz frequency after being unstart is estimated to be around 18 Hz, which is identical to that without the suction.

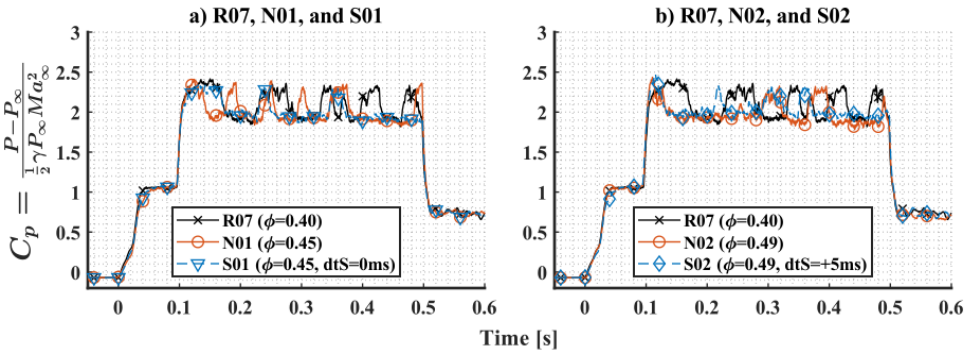

Fig. 5.16 Pressure traces at L2 for reference, non-, and single-suction cases

The differences between S01 and S02 cases imply the working mechanism of boundary-layer suction control. Boundary-layer suction extracts the mass from the low-speed region of the flow, enlarging the effective area. This could affect

two different aspects of flow choking. one is a direct mass addition/extraction that directly changes the incoming flow rate. The other is the local choked flow rate which is a function of the effective area of the flow. In other words, the mechanism of the boundary-layer suction control in unstarting flows can be from either or both or direct mass balancing and an increased choked flow rate. However, it is shown that the suction mass flow rates are the same for S01 and S02, and hence the direct mass balancing effect will be at a similar degree. If the control of unstarting flow relies on direct mass balancing, two cases must have shown similar effectiveness. Therefore, it could be concluded that the boundary-layer suppression effect from the suction flow has a greater influence. For S01, the boundary-layer suction was activated fast enough and the suction rate was large enough to increase the local choked flow rate, leading to a delayed unstart by a few tens of milliseconds. However, for S02, the activation delay of 5 ms allowed the boundary-layer to grow in time, resulting in an insufficient effective area to delay inlet unstart.

Lower wall pressure traces in S01 is collected and presented in Fig. 5.17. The general behavior is similar to that observed in R06 (see Fig. 5.10). The pressures are significantly increased after the fuel jet injection at around 100 ms. The unstart initiation (the first pressure drop) is seen at around 156 ms after the freestream trigger and the pressure surge shortly follows by 12 ms. After being unstarted, the pressures show a repeated pattern over two different pressure levels at a frequency of roughly 8.8 Hz, which is inlet buzz.

To elucidate the effect of boundary-layer suction control in frequency domains, STFT is performed at L1 for R05, N01, S01, and S02 and presented in Fig. 5.18 where R05 exhibits an example of a stable ramjet mode operation. Compared to R05 that shows highly fluctuating high-frequency components above 20 kHz (red dashed boxes) throughout the test period (Fig. 5.18(a)), this

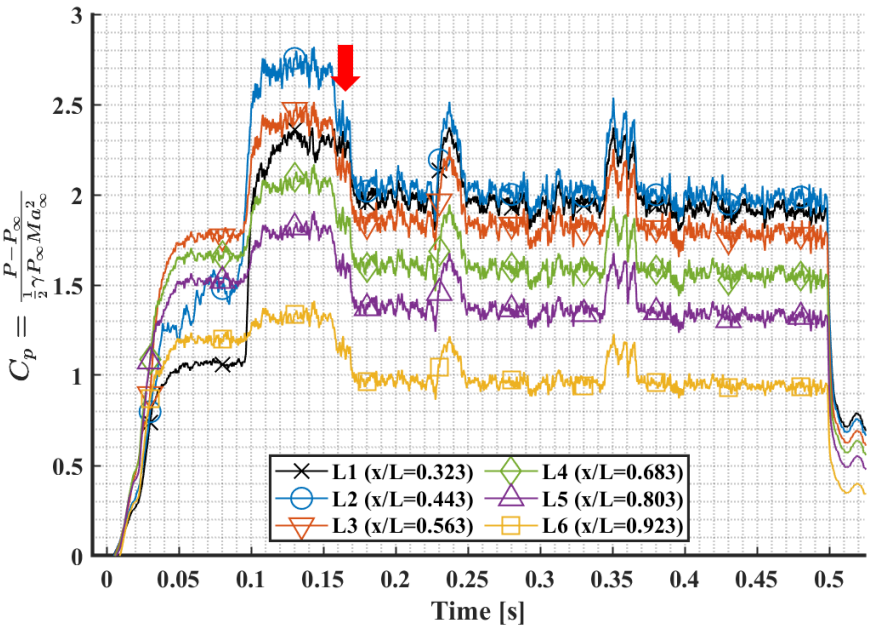

Fig. 5.17 Lower wall pressure traces in S01

high-frequency pressure fluctuation for N01 abruptly diminishes at around 120 ms after the freestream trigger (see the white vertical arrow in Fig. 5.18(b)). However, for S01, the weakening of high-frequency component fluctuation is delayed to around 150 ms, implying that a stable ramjet operation is extended in time. On the other hand, S02 shows almost the same behavior as that for N01. This confirms that the pressure drop after unstart initiation is strongly correlated to the level and the frequency of pressure fluctuation.

CH* chemiluminescence imaging is performed for N01 and S01 to investigate the effect of boundary-layer suction control in terms of flame behaviors. Four-time steps of an interval of 100 ms are presented as in Fig. 5.19 where a sub-interval of 25 ms is used for estimating the means and the standard deviations of CH* intensities in each time step. Both cases show similar behaviors

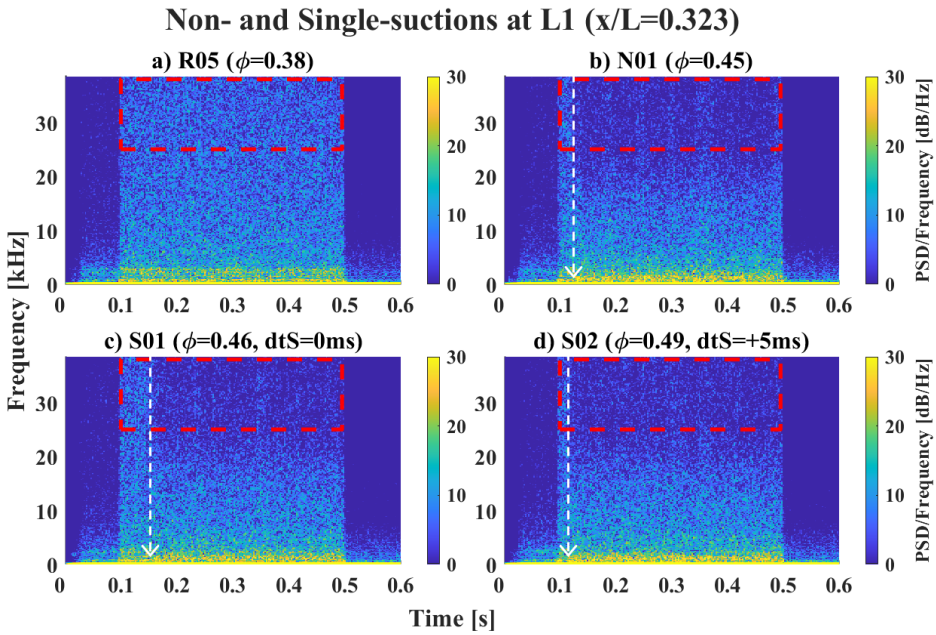

Fig. 5.18 STFT spectrogram at L1 (x/L=0.323) in reference, non-, and single-suction cases

to that in R05 before being unstarted: high mean intensity just upstream of the cavity, a high standard deviation of intensity downstream of the cavity (compare Fig. 5.19(a) and Fig. 5.19(i) – (j) to Fig. 5.14). After unstart, the standard deviation of CH* intensities in both cases significantly reduced (see Fig. 5.19(e) – (f) and (n) – (o)). Therefore, it could be concluded that the fluctuation level of CH* intensities is strongly correlated to the pressure behaviors.

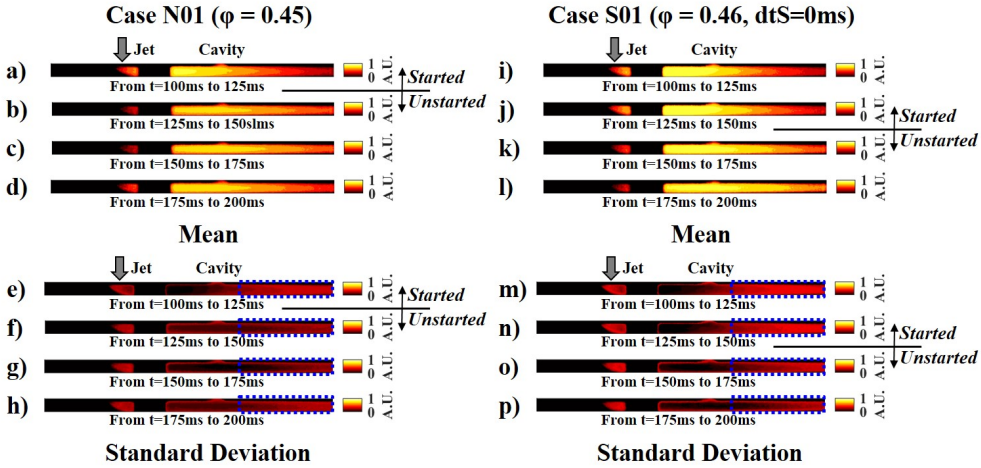

Fig. 5.19 Mean and standard deviation for CH* images from N01 (left) and S01 (right)

5.2.4 Non- and Double-Suction Cases

Single-suction in the previous section showed it could delay inlet unstart by a few tens of milliseconds only if it was triggered simultaneously with the fuel jet injection. In this section, another perforated at the side of the inlet is also activated concurrently to drive suction flow at a higher rate, i.e., double-suction. The estimated suction rate of double-suction configuration is 1.9 % on average, which is slightly smaller than twice the single-suction rate (1.2 %), presumably smaller pressure differences across the suction device due to fewer shock-compressions. The examined activation trigger delays of double-suction cases are 0 (no delay), +5, and +20 ms after the fuel jet injection trigger, which are designated D01, D02, and D03, respectively.

The pressure traces at L2 in double-suction cases along with the one in the equivalent non-suction case are presented in Fig. 5.20. R07 is also included to illustrate the behavior of unstarting flows at marginal conditions. Each double-

suction case with the reference (R07) and non-suction cases (N02) are plotted in different sub-figures (Fig. 5.20(a) to (c)), the final sub-figure collecting only the double-suction cases (Fig. 5.20(d)).

The double-suction with no trigger delay (D01) case shows started level pressure at around $C_p = 2.8$ until approximately 249 ms, which is 139 ms and 99 ms later than for N02 and R07, respectively (Fig. 5.20(a)). However, the unstart process is faster, taking only 10 ms for the pressure surge peak. When a trigger delay of 5 ms is applied (D02), the unstart initiation is seen at around 183 ms, which is still 73 ms later than for N02. When the trigger delay is further increased to 20 ms as for D03, the pressure trace at L2 shows an almost identical profile for that in N02 and the unstart initiation is observed at around 109 ms. Interestingly, inlet buzz phenomenon is only observed for D03, and the buzz frequency is approximately 12.7 Hz, which is about 71 % of that for the equivalent non-suction case (N02).

Moreover, an abnormal operation mode is observed in D02. To analyze the pressure traces in detail, lower wall pressure traces in D02 is collected and presented in Fig. 5.21. The pressure is first seen at around 183 ms, but the pressure surge is observed around 200 ms. However, unlike other cases in which pressures decreased again to unstart the inlet, the pressures are maintained approximately half-way between the started and unstarted levels except for L1: the pressure at L1 is fully recovered to the previous level (see the blue vertical arrow in Fig. 5.21). This implies that the unstart shock once traveled upstream of L1 to unstart the inlet but eventually traveled back and is anchored in between L1 and U1 due to insufficient mass imbalance. Therefore, this abnormal operation is a marginally unstarting condition created by the suction flow. This operation is sustained until around 274 ms when finally pressures are decreased to an unstarted level without pressure surges (red vertical arrow).

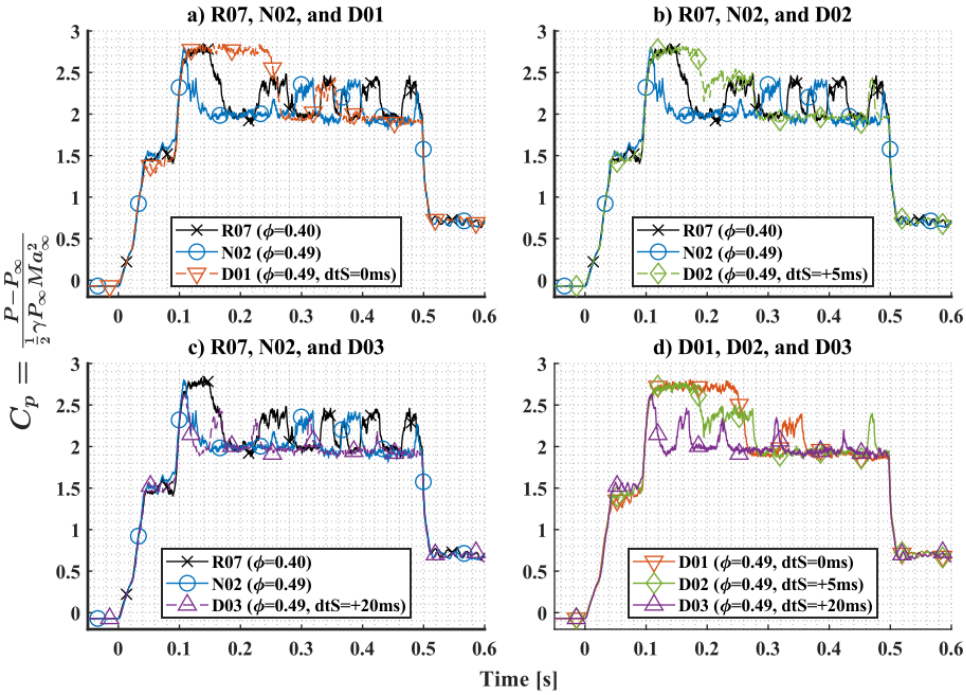

Fig. 5.20 Pressure traces at L2 in R07, N02, D01, D02, and D03

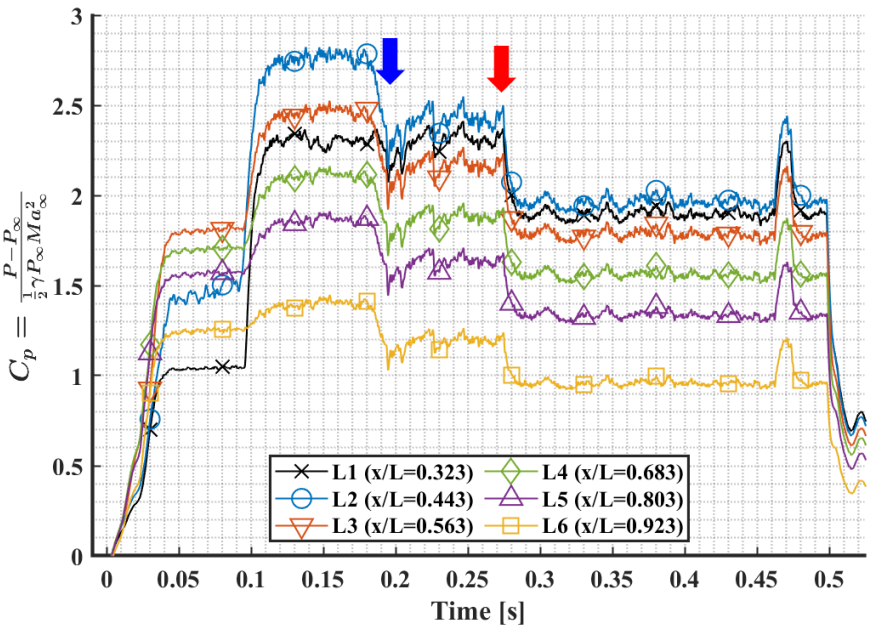

Fig. 5.21 Lower wall pressure traces in D02

5.2.5 Suction Control at Higher-ϕ

Boundary-layer suction is examined under higher equivalence ratio conditions to examine the effectiveness of the control. The equivalence ratio is set to be around $\phi = 0.67$, which is 72 % higher than the unstart ϕ-threshold. Single- and double-suction are both examined here but only without delays: suction is triggered synchronously with the jet injection trigger for both cases.

The unstart initiation for N11 case is observed almost immediately after the fuel jet injection, at around 104 ms. The inlet buzz frequency is approximately 23.7 Hz. However, unlike the previous cases in which single- and double-suction could delay inlet unstart by tens of milliseconds, the unstart is only delayed less than ten milliseconds. It is noteworthy that this 72 % increase in the equivalence ratio corresponds to only a 2 % increase in terms of the pure mass-loading (MCR). Therefore, it could be concluded that flow choking incurring inlet unstart in the current setup majorly relies on thermal choking effect, not the direct mass addition from the fuel jet: This higher degree of thermal choking leads to insufficient boundary-layer suppression, disabling control. On the other hand, there is only a single pressure peak each after the inlet unstart for both S11 and D11, suggesting that the buzz frequencies are significantly reduced by the suction.

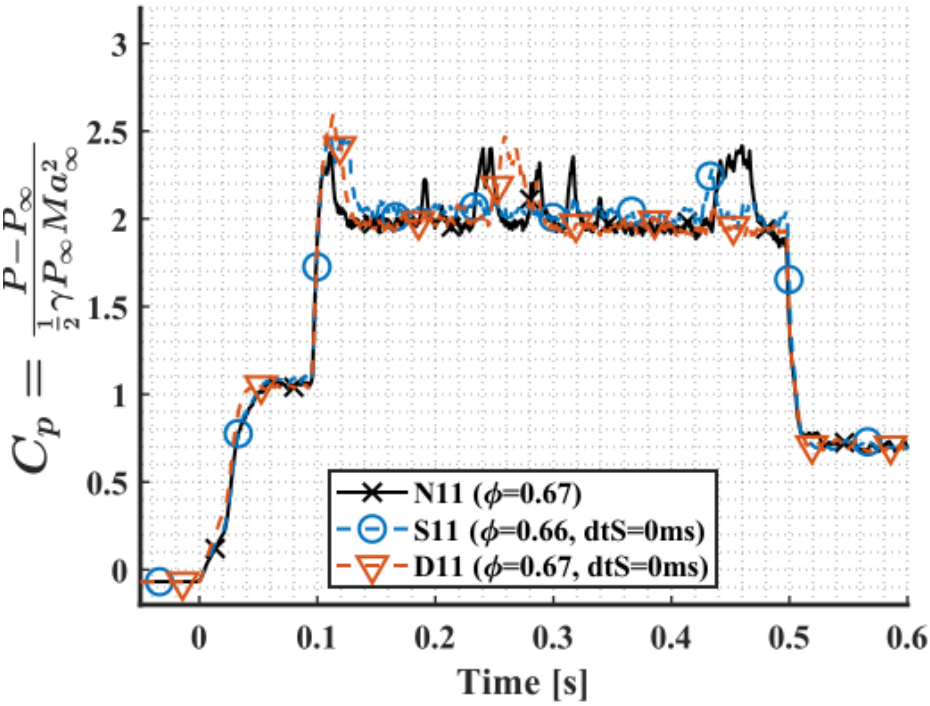

Fig. 5.22 Pressure traces at L2 in higher ϕ cases

5.3 Summary

The test results of boundary-layer suction control are summarized in Table 5.3. The actual activation time of suction control relative to a virtual unstart initiation is estimated and tabulated as in the third column in Table 5.3, "$dtS2$" (jet trigger timing + dtS + suction activation delay - the unstart initiation in the equivalent non-suction case). For example, $dtS2$ of 12 ms for S01 represents the suction control was activated 12 ms before the unstart initiation for the equivalent non-suction case (N01). The last column of Table 5.3, "Unstart Delay", is the unstart initiation in the suction case relative to the unstart initiation in the non-suction case.

In summary, boundary-layer suction control was examined to control inlet unstart under high-enthalpy freestream conditions. To trigger inlet unstart more realistically, an ethylene fuel jet was injected in the isolator region to incur thermal choking, leading to forming an unstart shock system. When ϕ was sufficiently low, the model was operated in a stable ram-mode under Mach 4.5 freestream conditions. When the overall equivalence ratio exceeded around 0.39, an abrupt pressure drop at all the sensor locations was observed accompanied by a reduction in power of high-frequency pressure fluctuations and lower variations of CH* concentration in time.

At moderately high-ϕ cases (roughly 20 % higher than the ϕ-threshold of unstart), both single- and double-suction were effective when they were activated fast enough, delaying inlet unstart by more than a few tens of milliseconds. Double-suction was turned out to be more effective in delaying inlet unstart since it extracted approximately 50 % more suction flow than that in single-suction cases. Furthermore, double-suction with a delayed trigger of 5 ms also showed higher effectiveness than single-suction without a trigger delay, thus, it

could be concluded that the suction rate is the most important parameter to control unstarting flows. In cases with exceedingly higher equivalence ratios at around 0.67, both single- and double-suction were ineffective.

Table 5.3 Test results for unstarting flow with suction

Case	ϕ	$dtS2$, ms	Suction Mass, %	Unstart Delay, ms
S01	0.46	-12	1.2	+ 34.4
S02	0.49	+6	1.2	+ 3.9
D01	0.49	+1	1.8	+ 138.8
D02	0.49	+6	1.9	+ 61.6
D03	0.48	+18	1.9	- 1.3
S11	0.66	+8	1.2	+ 5.9
D11	0.67	+5	2.0	+ 8.9

Chapter 6

Conclusion

Firstly, boundary-layer suction in a dual-mode scramjet isolator was modeled to estimate the performance under different operating conditions. The internal flow was assumed to be a two-dimensional compressible laminar flow in a constant-area channel. Similarity solutions for velocity and temperature are obtained for compressible laminar flows which, in turn, provided detailed flow dynamics with and without boundary-layer suction. It was turned out that boundary-layer suction could increase the choking flow rate significantly especially under large confinement parameters. Furthermore, mass-loading was decreased considerably primarily due to steeper velocity/temperature profiles. Also, characteristic time-scale analyses showed that boundary-layer suction at typical operating conditions for scramjet isolators requires a few milliseconds of execution delay.

Then, boundary-layer suction control on unstarting and unstarted flows were experimentally examined. Two sets of experiments for low- and high-enthalpy conditions were conducted using an arc-heated supersonic wind tunnel. Suction

flows were designed to extract approximately $1 \sim 2$ % of the freestream flow rate to minimize thrust loss from the suction. Various trigger delays were tested to investigate the effect of trigger delays and the feasibility of control under more realistic scenarios combined with inlet unstart precursor detections.

Under low-enthalpy conditions, the dynamics and the detailed processes of unstarting and unstarted flows were investigated. In this case, the threshold of inlet unstart was around $CMR = 0.85$. This implies that the primary mechanism of flow choking is frictional choking, which reduces the total pressure of the internal flow leading to a decrease in the local choked flow rate at downstream positions. As a result, unstart shock was first observed at the downstream end of the imaging area, propagating upstream to reach the inlet. It was confirmed that the propagation behaviors and speeds of unstart shock could be highly dependent on the flow's local static/total pressure gradient: Under FPGs, the propagation decelerated while accelerated under APGs. When boundary-layer suction was activated in unstarting flows, inlet unstart could only be avoided solely via suction by fast actuation (no delay to the jet injection trigger) near the threshold. In other cases, inlet unstart was delayed, not suppressed. Meanwhile, when boundary-layer suction was performed in unstarted flows, it could help inlet starting faster.

In high-enthalpy freestream flows, the aim was to find the precursor with quantitative measurements and to inlet unstart and subsequent activation of control to control unstarting flows. Three precursors were found in this study: i) pressure magnitude drops, ii) diminishing high-frequency pressure fluctuation, and iii) less variation of CH* intensities near cavity flameholder. The threshold of inlet unstart was observed around $CMR = 1.1$. Moreover, an abrupt pressure drop, which was one of the inlet unstart indicators, was observed earliest near the jet positions. Therefore, it could be concluded that flow choking under the high-

enthalpy and combustion environment was incurred near the jet injection point. When boundary-layer suction was activated in high-enthalpy flows near the inlet unstart threshold, the effectiveness was larger at higher suction flow rates and faster triggers: the higher suction flow rate and the faster the trigger, inlet unstart could be delayed longer. However, inlet unstart could not be avoided solely via boundary-layer suction under these conditions. Meanwhile, the effect of boundary-layer suction at higher equivalence ratios than the inlet unstart threshold, thus, a higher level of choking, was almost negligible.

In summary, it was shown that fast-acting boundary-layer suction is capable of suppressing or delaying inlet unstart. The effectiveness of the control was higher at a higher suction rate. Moreover, delayed suction was still effective under higher suction rates. Therefore, systematic consideration of suction location, unstart detection, and execution logic to perform boundary-layer suction is needed to determine the minimum suction rate.

Bibliography

[1] L. Foster, J. Saunders, B. Sanders, and L. Weir, "Highlights from a mach 4 experimental demonstration of inlet mode transition for turbine-based combined cycle hypersonic propulsion," in *48th AIAA/ASME/SAE/ASEE Joint Propulsion Conference & Exhibit.*

[2] W. GreyTrafalgar, "The compression, combustion, and expansion regions of: (a) turbojet, (b) ramjet, and (c) scramjet engines.," 2 July 2010. [Online; accessed 20-September-2020].

[3] F. S. Billig, "Research on supersonic combustion," *Journal of Propulsion and Power*, vol. 9, no. 4, pp. 499–514, 1993.

[4] M. Smart, "Optimization of two-dimensional scramjet inlets," *Journal of Aircraft*, vol. 36, no. 2, pp. 430–433, 1999.

[5] M. Smart and E. Ruf, "Free-jet testing of a rest scramjet at off-design conditions," in *25th AIAA aerodynamic Measurement technology and ground testing Conference*, p. 2955.

[6] E. T. Curran and S. N. B. Murthy, *Scramjet propulsion.* Progress in astronautics and aeronautics, Reston, Va.: American Institute of Aeronautics and Astronautics, 2000.

[7] G. DiCristina, K. Kang, S. J. Song, J. H. Choi, H. Do, and S.-k. Im, "Visualization of streamline tracing inlet-isolator flows using a planar laser rayleigh scattering imaging technique," *Journal of Visualization*, vol. 22, no. 2, pp. 359–369, 2019.

[8] K. Matsuo, Y. Miyazato, and H.-D. Kim, "Shock train and pseudo-shock phenomena in internal gas flows," *Progress in aerospace sciences*, vol. 35, no. 1, pp. 33–100, 1999.

[9] M. V. Suraweera and M. K. Smart, "Shock-tunnel experiments with a mach 12 rectangular-to-elliptical shape-transition scramjet at offdesign conditions," *Journal of Propulsion and Power*, vol. 25, no. 3, pp. 555–564, 2009.

[10] C. Zhang, Q. Yang, J. Chang, J. Tang, and W. Bao, "Nonlinear characteristics and detection of combustion modes for a hydrocarbon fueled scramjet," *Acta Astronautica*, vol. 110, pp. 89–98, 2015.

[11] F. M. White, *Fluid mechanics.* Mcgraw-Hill series in mechanical engineering, New York, NY: McGraw-Hill, 7th ed., 2011.

[12] J. Fike, K. Duraisamy, J. Alonso, H. Do, S.-k. Im, and M. Cappelli, "Experimental and computational investigation of mass injection induced unstart," in *29th AIAA Applied Aerodynamics Conference*, p. 3192.

[13] H.-j. Tan, L.-g. Li, Y.-f. Wen, and Q.-f. Zhang, "Experimental investigation of the unstart process of a generic hypersonic inlet," *AIAA Journal*, vol. 49, no. 2, pp. 279–288, 2011.

[14] J. L. Wagner, K. B. Yuceil, A. Valdivia, N. T. Clemens, and D. S. Dolling,

"Experimental investigation of unstart in an inlet/isolator model in mach 5 flow," *AIAA Journal*, vol. 47, no. 6, pp. 1528–1542, 2009.

[15] J. Wagner, K. Yuceil, A. Valdivia, N. Clemens, and D. Dolling, "Piv measurements of the unstart process in a supersonic inlet/isolator," in *38th Fluid Dynamics Conference and Exhibit*, p. 3849.

[16] H. Do, S.-k. Im, M. G. Mungal, and M. A. Cappelli, "The influence of boundary layers on supersonic inlet flow unstart induced by mass injection," *Experiments in fluids*, vol. 51, no. 3, p. 679, 2011.

[17] S. Im, D. Baccarella, B. McGann, Q. Liu, L. Wermer, and H. Do, "Unstart phenomena induced by mass addition and heat release in a model scramjet," *Journal of Fluid Mechanics*, vol. 797, pp. 604–629, 2016.

[18] H. Babinsky, Y. Li, and C. W. Pitt Ford, "Microramp control of supersonic oblique shock-wave/boundary-layer interactions," *AIAA Journal*, vol. 47, no. 3, pp. 668–675, 2009.

[19] D. Herrmann and A. Gülhan, "Experimental analyses of inlet characteristics of an airbreathing missile with boundary-layer bleed," *Journal of Propulsion and Power*, vol. 31, no. 1, pp. 170–179, 2015.

[20] S. Im, H. Do, and M. A. Cappelli, "Dielectric barrier discharge control of a turbulent boundary layer in a supersonic flow," *Applied Physics Letters*, vol. 97, no. 4, 2010.

[21] A. Valdivia, K. B. Yuceil, J. L. Wagner, N. T. Clemens, and D. S. Dolling, "Control of supersonic inlet-isolator unstart using active and passive vortex generators," *AIAA Journal*, vol. 52, no. 6, pp. 1207–1218, 2014.

[22] Y. Wang, Y. Li, L. Xiao, B. Zhang, and Y. Li, "Similarity-solution-based improvement of γ-re model for hypersonic transition prediction," *International Journal of Heat and Mass Transfer*, vol. 124, pp. 491–503, 2018.

[23] F. E. Udwadia and A. Farahani, "Accelerated runge-kutta methods," *Discrete Dynamics in Nature and Society*, vol. 2008, pp. 1–38, 2008.

[24] P. M. Allison, K. Frederickson, J. W. Kirik, R. D. Rockwell, W. R. Lempert, and J. A. Sutton, "Investigation of supersonic combustion dynamics via 50 khz ch* chemiluminescence imaging," *Proceedings of the Combustion Institute*, vol. 36, no. 2, pp. 2849–2856, 2017.

[25] F. Billig and G. Dugger, "The interaction of shock waves and heat addition in the design of supersonic combustors," in *Symposium (International) on Combustion*, vol. 12, pp. 1125–1139, Elsevier.

[26] R. R. Boyce, A. Paull, and R. J. Stalker, "Unstarted inlet for direct-connect combustor experiments in a shock tunnel," *Journal of Propulsion and Power*, vol. 16, no. 4, pp. 718–720, 2000.

[27] Z. Cai, Y. Yang, M. Sun, and Z. Wang, "Experimental investigation on ignition schemes of a supersonic combustor with the rearwall-expansion cavity," *Acta Astronautica*, vol. 123, pp. 181–187, 2016.

[28] E. T. Curran, W. H. Heiser, and D. T. Pratt, "Fluid phenomena in scramjet combustion systems," *Annual Review of Fluid Mechanics*, vol. 28, no. 1, pp. 323–360, 1996.

[29] Z. J. Denman, W. Y. Chan, S. Brieschenk, A. Veeraragavan, V. Wheatley, and M. K. Smart, "Ignition experiments of hydrocarbons in a mach 8

shape-transitioning scramjet engine," *Journal of Propulsion and Power*, vol. 32, no. 6, pp. 1462–1471, 2016.

[30] H. Do, M. A. Cappelli, and M. G. Mungal, "Plasma assisted cavity flame ignition in supersonic flows," *Combustion and Flame*, vol. 157, no. 9, pp. 1783–1794, 2010.

[31] H. Do, S.-k. Im, M. G. Mungal, and M. A. Cappelli, "Visualizing supersonic inlet duct unstart using planar laser rayleigh scattering," *Experiments in Fluids*, vol. 50, no. 6, pp. 1651–1657, 2010.

[32] J. Donbar, G. Linn, and M. Akella, "High-frequency pressure measurements for unstart detection in scramjet isolators," in *46th AIAA/ASME/SAE/ASEE Joint Propulsion Conference & Exhibit*, p. 6557.

[33] W. E. Eagle and J. F. Driscoll, "Shock wave–boundary layer interactions in rectangular inlets: three-dimensional separation topology and critical points," *Journal of Fluid Mechanics*, vol. 756, pp. 328–353, 2014.

[34] J. S. Geerts and K. H. Yu, "Shock train/boundary-layer interaction in rectangular isolators," *AIAA Journal*, vol. 54, no. 11, pp. 3450–3464, 2016.

[35] F. Gnani, H. Zare-Behtash, and K. Kontis, "Pseudo-shock waves and their interactions in high-speed intakes," *Progress in Aerospace Sciences*, vol. 82, pp. 36–56, 2016.

[36] R. J. Gollan and M. K. Smart, "Design of modular shape-transition inlets for a conical hypersonic vehicle," *Journal of Propulsion and Power*, vol. 29, no. 4, pp. 832–838, 2013.

[37] C. P. Goyne, J. C. McDaniel, R. H. Krauss, and W. B. Whitehurst,

"Test gas vitiation effects in a dual-mode scramjet combustor," *Journal of Propulsion and Power*, vol. 23, no. 3, pp. 559–565, 2007.

[38] M. R. Gruber, J. M. Donbar, C. D. Carter, and K.-Y. Hsu, "Mixing and combustion studies using cavity-based flameholders in a supersonic flow," *Journal of Propulsion and Power*, vol. 20, no. 5, pp. 769–778, 2004.

[39] T. Gu, S. Zhang, and Y. Zheng, "Performance of a jaws inlet under off-design conditions," *Proceedings of the Institution of Mechanical Engineers, Part G: Journal of Aerospace Engineering*, vol. 231, no. 2, pp. 294–305, 2016.

[40] J. Häberle and A. Gülhan, "Experimental investigation of a two-dimensional and a three-dimensional scramjet inlet at mach 7," *Journal of Propulsion and Power*, vol. 24, no. 5, pp. 1023–1034, 2008.

[41] J. Häberle and A. Gülhan, "Investigation of two-dimensional scramjet inlet flowfield at mach 7," *Journal of Propulsion and Power*, vol. 24, no. 3, pp. 446–459, 2008.

[42] T. C. Hoeger, "Cfd transient simulation of an isolator shock train in a scramjet engine," 2012.

[43] W. Huang, Z. G. Wang, L. Jin, and J. Liu, "Effect of cavity location on combustion flow field of integrated hypersonic vehicle in near space," *Journal of Visualization*, vol. 14, no. 4, pp. 339–351, 2011.

[44] M. Kodera, T. Sunami, and K. Nakahashi, "Numerical analysis of scramjet combusting flows by unstructured hybrid grid method," in *38th Aerospace Sciences Meeting and Exhibit*, p. 886.

[45] M. Kodera, T. Sunami, and K. Nakahasi, "Numerical study of mixing and combustion process of a scramjet engine model," in *10th AIAA/NAL-NASDA-ISAS International Space Planes and Hypersonic Systems and Technologies Conference*, p. 1868.

[46] J. Larsson, "Large eddy simulation of the hyshot ii scramjet combustor using a supersonic flamelet model," in *48th AIAA/ASME/SAE/ASEE joint propulsion conference & exhibit*, p. 4261.

[47] J. Larsson, S. Laurence, I. Bermejo-Moreno, J. Bodart, S. Karl, and R. Vicquelin, "Incipient thermal choking and stable shock-train formation in the heat-release region of a scramjet combustor. part ii: Large eddy simulations," *Combustion and Flame*, vol. 162, no. 4, pp. 907–920, 2015.

[48] S. Laurence, J. Martinez Schramm, S. Karl, and K. Hannemann, "An experimental investigation of steady and unsteady combustion phenomena in the hyshot ii combustor," in *17th AIAA International Space Planes and Hypersonic Systems and Technologies Conference*, p. 2310.

[49] D. B. Le, C. P. Goyne, R. H. Krauss, and J. C. McDaniel, "Experimental study of a dual-mode scramjet isolator," *Journal of Propulsion and Power*, vol. 24, no. 5, pp. 1050–1057, 2008.

[50] K.-C. Lin, C.-J. Tam, K. Jackson, D. Eklund, and T. Jackson, "Characterization of shock train structures inside constant-area isolators of model scramjet combustors," in *44th AIAA Aerospace Sciences Meeting and Exhibit*, p. 816.

[51] T. Mathur, M. Gruber, K. Jackson, J. Donbar, W. Donaldson, T. Jackson, and F. Billig, "Supersonic combustion experiments with a cavity-based fuel

injector," *Journal of Propulsion and Power*, vol. 17, no. 6, pp. 1305–1312, 2001.

[52] T. Mitani, N. Chinzei, and T. Kanda, "Reaction and mixing-controlled combustion in scramjet engines," *Journal of Propulsion and Power*, vol. 17, no. 2, pp. 308–314, 2001.

[53] B. Morgan, K. Duraisamy, and S. K. Lele, "Large-eddy simulations of a normal shock train in a constant-area isolator," *AIAA Journal*, vol. 52, no. 3, pp. 539–558, 2014.

[54] H. Ouyang, W. Liu, and M. Sun, "Numerical investigation of the influence of injection scheme on the ethylene supersonic combustion," *Advances in Mechanical Engineering*, vol. 6, 2015.

[55] R. Pecnik, V. E. Terrapon, F. Ham, G. Iaccarino, and H. Pitsch, "Reynolds-averaged navier-stokes simulations of the hyshot ii scramjet," *AIAA Journal*, vol. 50, no. 8, pp. 1717–1732, 2012.

[56] B. Qin, J. Chang, X. Jiao, W. Bao, and D. Yu, "Numerical investigation of the impact of asymmetric fuel injection on shock train characteristics," *Acta Astronautica*, vol. 105, no. 1, pp. 66–74, 2014.

[57] N. O. P. Raj and K. Venkatasubbaiah, "A new approach for the design of hypersonic scramjet inlets," *Physics of Fluids*, vol. 24, no. 8, 2012.

[58] M. K. Smart, "Design of three-dimensional hypersonic inlets with rectangular-to-elliptical shape transition," *Journal of Propulsion and Power*, vol. 15, no. 3, pp. 408–416, 1999.

[59] M. K. Smart, "Experimental testing of a hypersonic inlet with rectangular-

to-elliptical shape transition," *Journal of Propulsion and Power*, vol. 17, no. 2, pp. 276–283, 2001.

[60] M. K. Smart and C. A. Trexler, "Mach 4 performance of hypersonic inlet with rectangular-to-elliptical shape transition," *Journal of Propulsion and Power*, vol. 20, no. 2, pp. 288–293, 2004.

[61] M. R. Soltani, A. Daliri, and J. S. Younsi, "Effects of shock wave/boundary-layer interaction on performance and stability of a mixed-compression inlet," *Scientia Iranica. Transaction B, Mechanical Engineering*, vol. 23, no. 4, p. 1811, 2016.

[62] R. Starkey, "Off-design performance characterization of a variable geometry scramjet," in *41st AIAA/ASME/SAE/ASEE Joint Propulsion Conference & Exhibit*, p. 3711.

[63] C.-J. Tam and M. Hagenmaier, "Unsteady analysis of scramjet inlet flowfields using numerical simulations," in *37th Aerospace Sciences Meeting and Exhibit*, p. 613.

[64] C. Trexler, "Inlet starting predictions for sidewall-compression scramjet inlets," in *24th Joint Propulsion Conference*.

[65] Z. P. Wang, F. Li, H. B. Gu, X. L. Yu, and X. Y. Zhang, "Experimental study on the effect of combustor configuration on the performance of dual-mode combustor," *Aerospace Science and Technology*, vol. 42, pp. 169–175, 2015.

[66] Y. K. Wilson Chan, S. A. Razzaqi, D. J. Wise, and M. Smart, "Freejet testing of the 75%-scale hifire 7 rest scramjet engine," in *19th AIAA In-*

ternational Space Planes and Hypersonic Systems and Technologies Conference.

[67] W.-z. Xie, G.-f. Ma, R.-w. Guo, H. Chen, Y.-f. Wen, and S. Guo, "Flow-based prediction for self-starting limit of two-dimensional hypersonic inlets," *Journal of Propulsion and Power*, vol. 32, no. 2, pp. 463–471, 2016.

[68] F. Xing, C. Ruan, Y. Huang, X. Fang, and Y. Yao, "Numerical investigation on shock train control and applications in a scramjet engine," *Aerospace Science and Technology*, vol. 60, pp. 162–171, 2017.

[69] T. Zhang, J. Wang, X. Fan, and P. Zhang, "Combustion of vaporized kerosene in supersonic model combustors with dislocated dual cavities," *Journal of Propulsion and Power*, vol. 30, no. 5, pp. 1152–1160, 2014.

[70] V. Zimont and V. Ostras, "Calculation of pseudo-shocks in a cylindrical duct(transitional supersonic-subsonic flow)," *Fluid Mechanics-Soviet Research*, vol. 5, pp. 78–87, 1976.

[71] P. J. Waltrup and F. S. Billig, "Prediction of precombustion wall pressure distributions in scramjet engines," *Journal of Spacecraft and Rockets*, vol. 10, no. 9, pp. 620–622, 1973.

[72] R. Baurle and D. Eklund, "Analysis of dual-mode hydrocarbon scramjet operation at mach 4-6.5," *Journal of Propulsion and Power*, vol. 18, no. 5, pp. 990–1002, 2002.

[73] S. Emami, C. A. Trexler, A. H. Auslender, and J. P. Weidner, "Experimental investigation of inlet-combustor isolators for a dual-mode scramjet at a mach number of 4," 1995.

[74] W. H. Heiser and D. T. Pratt, *Hypersonic airbreathing propulsion*, pp. xx, 587 p. Washington, D.C.: American Institute of Aeronautics and Astronautics, 1994.

[75] W. Huang, L. Yan, and J.-g. Tan, "Survey on the mode transition technique in combined cycle propulsion systems," *Aerospace Science and Technology*, vol. 39, pp. 685–691, 2014.

[76] D. B. Le, C. P. Goyne, and R. H. Krauss, "Shock train leading-edge detection in a dual-mode scramjet," *Journal of Propulsion and Power*, vol. 24, no. 5, pp. 1035–1041, 2008.

[77] J. C. McDaniel, "Dual-mode scramjet operation at a mach 5 flight enthalpy in a clean air test facility," in *AIP Conference Proceedings*, pp. 1277–1282.

[78] D. PRATT and W. HEISER, "Isolator-combustor interaction in a dual-mode scramjet engine," in *31st Aerospace Sciences Meeting*, p. 358.

[79] D. Riggins, R. Tackett, T. Taylor, and A. Auslender, "Thermodynamic analysis of dual-mode scramjet engine operation and performance," in *14th AIAA/AHI space planes and hypersonic systems and technologies conference*, p. 8059.

[80] L. Tian, L.-H. Chen, Q. Chen, F.-Q. Zhong, and X.-Y. Chang, "Engine performance analysis and optimization of a dual-mode scramjet with varied inlet conditions," *Acta Mechanica Sinica*, vol. 32, no. 1, pp. 75–82, 2015.

[81] R. J. Yentsch and D. V. Gaitonde, "Numerical investigation of dual-mode operation in a rectangular scramjet flowpath," *Journal of Propulsion and Power*, vol. 30, no. 2, pp. 474–489, 2014.

[82] S. Torrez, N. Scholten, D. Micka, J. Driscoll, M. Bolender, D. Doman, and M. Oppenheimer, "A scramjet engine model including effects of precombustion shocks and dissociation," in *44th AIAA/ASME/SAE/ASEE Joint Propulsion Conference & Exhibit.*

[83] M. Brocanelli, Y. Gunbatar, A. Serrani, and M. Bolender, "Robust control for unstart recovery in hypersonic vehicles," in *AIAA Guidance, Navigation, and Control Conference*, p. 4698.

[84] R. Cao, J. Chang, J. Tang, W. Bao, D. Yu, and Z. Wang, "Switching control of thrust regulation and inlet unstart protection for scramjet engine based on strategy of integral initial values resetting," *Aerospace Science and Technology*, vol. 45, pp. 484–489, 2015.

[85] W. Hawkins and E. Marquart, *Two-dimensional generic inlet unstart detection at Mach 2.5-5.0*, p. 6019. 1995.

[86] X. Hao, J. Chang, W. Bao, and Z. Zhang, "A model of mode transition logic in dual-mode scramjet engines," *Aerospace Science and Technology*, vol. 49, pp. 173–184, 2016.

[87] H.-J. Tan, S. Sun, and Z.-L. Yin, "Oscillatory flows of rectangular hypersonic inlet unstart caused by downstream mass-flow choking," *Journal of Propulsion and Power*, vol. 25, no. 1, pp. 138–147, 2009.

[88] W. Yi, L. Jian-han, F. Xiao-qiang, L. Wei-dong, and W. Zhen-guo, "Investigation on the unstarted flowfield of a three-dimensional sidewall compression hypersonic inlet," in *16th AIAA/DLR/DGLR International Space Planes and Hypersonic Systems and Technologies Conference*, p. 7404.

[89] Q.-F. Zhang, H.-J. Tan, H. Chen, Y.-Q. Yuan, and Y.-C. Zhang, "Unstart process of a rectangular hypersonic inlet at different mach numbers," *AIAA Journal*, vol. 54, no. 12, pp. 3681–3691, 2016.

[90] Q. F. Zhang, H. J. Tan, S. Sun, H. X. Bu, and C. Y. Rao, "Unstart of a hypersonic inlet with side compression caused by downstream choking," *AIAA Journal*, vol. 54, no. 1, pp. 28–38, 2016.

[91] K. J. Ryu, S. Lim, and D. J. Song, "A computational study of the effect of angles of attack on a double-cone type supersonic inlet with a bleeding system," *Computers & fluids*, vol. 50, no. 1, pp. 72–80, 2011.

[92] M. R. Soltani, A. Daliri, J. S. Younsi, and M. Farahani, "Effects of bleed position on the stability of a supersonic inlet," *Journal of Propulsion and Power*, vol. 32, no. 5, pp. 1153–1166, 2016.

[93] M. A. Bolender, B. Dauby, J. A. Muse, and D. Adamczak, "Hifire 6: Overview and status update 2014," in *20th AIAA International Space Planes and Hypersonic Systems and Technologies Conference*.

[94] A. H. Shapiro, *The dynamics and thermodynamics of compressible fluid flow*. John Wiley & Sons, 1953.

[95] T. Cui, Z. Lv, and D. Yu, "Multistability and complex routes of supersonic inlet start/unstart," *Journal of Propulsion and Power*, vol. 27, no. 6, pp. 1204–1217, 2011.

[96] T. Cui and S. Tang, "Geometry rule of combustor–inlet interaction in ramjet engines," *Journal of Propulsion and Power*, vol. 30, no. 2, pp. 449–460, 2014.

[97] K. Kang, L. Wermer, S. Im, S. J. Song, and H. Do, "Fast-acting boundary-layer suction to control unstarting and unstarted flows," *Aiaa Journal*, vol. 58, no. 6, pp. 2475–2485, 2020.

[98] T. Kojima, T. Sato, S. Sawai, and N. Tanatsugu, "Experimental study on restart control of a supersonic air-breathing engine," *Journal of Propulsion and Power*, vol. 20, no. 2, pp. 273–279, 2004.

[99] A. Kantrowitz, "Preliminary investigation of supersonic diffusers," report, NATIONAL AERONAUTICS AND SPACE ADMIN LANGLEY RESEARCH CENTER HAMPTON VA, 1945.

[100] A. K. Flock and A. Gülhan, "Experimental investigation of the starting behavior of a three-dimensional scramjet intake," *AIAA Journal*, vol. 53, no. 9, pp. 2686–2693, 2015.

[101] J. Chang, Y. Fan, W. Bao, D. Yu, and Y. Shen, "Unstart margin control of hypersonic inlets," *Acta Astronautica*, vol. 66, no. 1-2, pp. 78–87, 2010.

[102] B. Qin, J. Chang, X. Jiao, and W. Bao, "Unstart margin characterization method of scramjet considering isolator–combustor interactions," *AIAA Journal*, vol. 53, no. 2, pp. 493–500, 2015.

[103] E. J. Stephen, S. R. Hoenisch, C. J. Riggs, M. L. Waddel, M. A. Bolender, and T. E. McLaughlin, "Hifire-6 unstart conditions at off-design mach numbers," in *53rd AIAA Aerospace Sciences Meeting*.

[104] C. Tao, Y. Daren, C. Juntao, and B. Wen, "Catastrophe model for supersonic inlet start/unstart," *Journal of Aircraft*, vol. 46, no. 4, pp. 1160–1166, 2009.

[105] S. K. Im and H. Do, "Unstart phenomena induced by flow choking in scramjet inlet-isolators," *Progress in Aerospace Sciences*, vol. 97, pp. 1–21, 2018.

[106] S. Mashio, K. Kurashina, T. Bamba, S. Okimoto, and S. Kaji, "Unstart phenomenon due to thermal choke in scramjet module," in *10th AIAA/NAL-NASDA-ISAS International Space Planes and Hypersonic Systems and Technologies Conference*, p. 1887.

[107] K. McDaniel and J. Edwards, "Simulation of thermal choking in a model scramjet combustor," in *30th Fluid Dynamics Conference*, p. 3411.

[108] K. McDaniel and J. Edwards, "Three-dimensional simulation of thermal choking in a model scramjet combustor," in *39th Aerospace Sciences Meeting and Exhibit*.

[109] T. Mitani, K. Tani, and H. Miyajima, "Flow choking by drag and combustion in supersonic engine testing," *Journal of Propulsion and Power*, vol. 23, no. 6, pp. 1177–1184, 2007.

[110] Z. Qifan, T. Huijun, and B. Huanxian, "Investigation of a movable slot-plate control method for hypersonic inlet unstart caused by downstream mass-flow choking," in *50th AIAA/ASME/SAE/ASEE Joint Propulsion Conference*, p. 3847.

[111] L. Sun, H. Sugiyama, K. Mizobata, R. Minato, and A. Tojo, "Numerical and experimental investigations on mach 2 and 4 pseudo-shock waves in a square duct," *Transactions of the Japan Society for Aeronautical and Space Sciences*, vol. 47, no. 156, pp. 124–130, 2004.

[112] L. Q. Sun, H. Sugiyama, K. Mizobata, and K. Fukuda, "Numerical and

experimental investigations on the mach 2 pseudo-shock wave in a square duct," *Journal of Visualization*, vol. 6, no. 4, pp. 363–370, 2003.

[113] T. Ikui, K. Matsuo, and M. NAGAI, "The mechanism of pseudo-shock waves," *Bulletin of JSME*, vol. 17, no. 108, pp. 731–739, 1974.

[114] T. IKUI, K. MATSUO, and K. SASAGUCHI, "Modified diffusion model of pseudo-shock waves considering upstream boundary layers," *Bulletin of JSME*, vol. 24, no. 197, pp. 1920–1927, 1981.

[115] H. Do, A. Passaro, and D. Baccarella, "Inlet unstart of an ethylene-fueled model scramjet with a mach 4.5 freestream flow," in *18th AIAA/3AF International Space Planes and Hypersonic Systems and Technologies Conference*, p. 5929.

[116] H. Do, A. Passaro, T. Lee, and D. Baccarella, "Ethylene flame dynamics in an arc-heated hypersonic wind tunnel," in *51st AIAA Aerospace Sciences Meeting Including the New Horizons Forum and Aerospace Exposition*, p. 700.

[117] Q. Liu, A. Passaro, D. Baccarella, and H. Do, "Ethylene flame dynamics and inlet unstart in a model scramjet," *Journal of Propulsion and Power*, vol. 30, no. 6, pp. 1577–1585, 2014.

[118] J. Chang, N. Li, K. Xu, W. Bao, and D. Yu, "Recent research progress on unstart mechanism, detection and control of hypersonic inlet," *Progress in Aerospace Sciences*, vol. 89, pp. 1–22, 2017.

[119] J. Chang, L. Wang, B. Qin, W. Bao, and D. Yu, "Real-time unstart prediction and detection of hypersonic inlet based on recursive fourier trans-

form," *Proceedings of the Institution of Mechanical Engineers, Part G: Journal of Aerospace Engineering*, vol. 229, no. 4, pp. 772–778, 2014.

[120] J. Chang, D. Yu, W. Bao, Z. Xie, and Y. Fan, "A cfd assessment of classifications for hypersonic inlet start/unstart phenomena," *The Aeronautical Journal*, vol. 113, no. 1142, pp. 263–271, 2016.

[121] J. Chang, R. Zheng, L. Wang, W. Bao, and D. Yu, "Backpressure unstart detection for a scramjet inlet based on information fusion," *Acta Astronautica*, vol. 95, pp. 1–14, 2014.

[122] R. Deng, Y. Jin, and H. D. Kim, "Numerical simulation of the unstart process of dual-mode scramjet," *International Journal of Heat and Mass Transfer*, vol. 105, pp. 394–400, 2017.

[123] A. Galli, B. Corbel, and R. Bur, "Control of forced shock-wave oscillations and separated boundary layer interaction," *Aerospace science and technology*, vol. 9, no. 8, pp. 653–660, 2005.

[124] H. Hexia, T. Huijun, S. Shu, and N. Le, "A fluidic control method of shock train in hypersonic inlet/isolator," in *50th AIAA/ASME/SAE/ASEE Joint Propulsion Conference*, p. 3846.

[125] S. D. Holland, "Wind-tunnel blockage and actuation systems test of a two-dimensional scramjet inlet unstart model at mach 6," 1994.

[126] K. Hutchins, M. Akella, N. Clemens, and J. Donbar, "Detection and transient dynamics modeling of experimental hypersonic inlet unstart," in *6th AIAA Flow Control Conference*, p. 2808.

[127] K. E. Hutchins, M. R. Akella, N. T. Clemens, J. M. Donbar, and S. Gogineni, "Experimental identification of transient dynamics for supersonic

inlet unstart," *Journal of Propulsion and Power*, vol. 30, no. 6, pp. 1605–1612, 2014.

[128] S. Karl, J. Martinez Schramm, K. Hannemann, and S. Laurence, "Cfd analysis of unstart characteristics of the hyshot-ii scramjet configuration in the heg shock tunnel," in *17th AIAA International Space Planes and Hypersonic Systems and Technologies Conference*, p. 2309.

[129] Z. Li, W. Gao, H. Jiang, and J. Yang, "Unsteady behaviors of a hypersonic inlet caused by throttling in shock tunnel," *AIAA Journal*, vol. 51, no. 10, pp. 2485–2492, 2013.

[130] D. W. Mayer and G. C. Paynter, "Prediction of supersonic inlet unstart caused by freestream disturbances," *AIAA Journal*, vol. 33, no. 2, pp. 266–275, 1995.

[131] M. Neaves, D. McRae, and J. Edwards, "High-speed inlet unstart calculations using an implicit solution adaptive mesh algorithm," in *39th Aerospace Sciences Meeting and Exhibit*, p. 825.

[132] R. W. Newsome, "Numerical simulation of near-critical and unsteady, subcritical inlet flow," *AIAA Journal*, vol. 22, no. 10, pp. 1375–1379, 1984.

[133] S. Pettinari, M. L. Corradini, and A. Serrani, "Detection of scramjet unstart in a hypersonic vehicle model," in *2012 American Control Conference (ACC)*, pp. 2509–2514.

[134] P. E. Rodi, S. Emami, and C. A. Trexler, "Unsteady pressure behavior in a ramjet/scramjet inlet," *Journal of Propulsion and Power*, vol. 12, no. 3, pp. 486–493, 1996.

[135] T. Shimura, T. Mitani, N. Sakuranaka, and M. Izumikawa, "Load oscillations caused by unstart of hypersonic wind tunnels and engines," *Journal of Propulsion and Power*, vol. 14, no. 3, pp. 348–353, 1998.

[136] S. Srikant, J. L. Wagner, A. Valdivia, M. R. Akella, and N. Clemens, "Unstart detection in a simplified-geometry hypersonic inlet-isolator flow," *Journal of Propulsion and Power*, vol. 26, no. 5, pp. 1059–1071, 2010.

[137] W.-Y. Su and K.-Y. Zhang, "Back-pressure effects on the hypersonic inlet-isolator pseudoshock motions," *Journal of Propulsion and Power*, vol. 29, no. 6, pp. 1391–1399, 2013.

[138] H.-J. Tan and R.-W. Guo, "Experimental study of the unstable-unstarted condition of a hypersonic inlet at mach 6," *Journal of Propulsion and Power*, vol. 23, no. 4, pp. 783–788, 2007.

[139] S. Trapier, S. Deck, P. Duveau, and P. Sagaut, "Time-frequency analysis and detection of supersonic inlet buzz," *AIAA Journal*, vol. 45, no. 9, pp. 2273–2284, 2007.

[140] J. L. Wagner, K. B. Yuceil, and N. T. Clemens, "Velocimetry measurements of unstart of an inlet-isolator model in mach 5 flow," *AIAA Journal*, vol. 48, no. 9, pp. 1875–1888, 2010.

[141] J. Chang, L. Wang, and W. Bao, "Mathematical modeling and characteristic analysis of scramjet buzz," *Proceedings of the Institution of Mechanical Engineers, Part G: Journal of Aerospace Engineering*, vol. 228, no. 13, pp. 2542–2552, 2014.

[142] J. Chang, L. Wang, W. Bao, J. Qin, J. Niu, and W. Xue, "Novel oscilla-

tory patterns of hypersonic inlet buzz," *Journal of Propulsion and Power*, vol. 28, no. 6, pp. 1214–1221, 2012.

[143] H. A. Holden and H. Babinsky, "Separated shock-boundary-layer interaction control using streamwise slots," *Journal of Aircraft*, vol. 42, no. 1, pp. 166–171, 2005.

[144] B. Anderson, J. Tinapple, and L. Surber, "Optimal control of shock wave turbulent boundary layer interactions using micro-array actuation," in *3rd AIAA flow control conference*, p. 3197.

[145] H. Babinsky, N. Makinson, and C. Morgan, "Micro-vortex generator flow control for supersonic engine inlets," in *45th AIAA Aerospace Sciences Meeting and Exhibit*.

[146] J. M. Delery, "Shock wave/turbulent boundary layer interaction and its control," *Progress in Aerospace Sciences*, vol. 22, no. 4, pp. 209–280, 1985.

[147] D. McCormick, "Shock/boundary-layer interaction control with vortex generators and passive cavity," *AIAA journal*, vol. 31, no. 1, pp. 91–96, 1993.

[148] A. G. Panaras and F. K. Lu, "Micro-vortex generators for shock wave/boundary layer interactions," *Progress in Aerospace Sciences*, vol. 74, pp. 16–47, 2015.

[149] N. Titchener and H. Babinsky, "Shock wave/boundary-layer interaction control using a combination of vortex generators and bleed," *AIAA journal*, vol. 51, no. 5, pp. 1221–1233, 2013.

[150] Y. Yan, C. Chen, P. Lu, and C. Liu, "Study on shock wave-vortex ring interaction by the micro vortex generator controlled ramp flow with turbu-

lent inflow," *Aerospace Science and Technology*, vol. 30, no. 1, pp. 226–231, 2013.

[151] Y. Yan and C. Liu, "Study on the ring-like vortical structure in mvg controlled supersonic ramp flow with different inflow conditions," *Aerospace Science and Technology*, vol. 35, pp. 106–115, 2014.

[152] J. Chang, D. Yu, W. Bao, Y. Fan, and Y. Shen, "Effects of boundary-layers bleeding on unstart/restart characteristics of hypersonic inlets," *The Aeronautical Journal*, vol. 113, no. 1143, pp. 319–327, 2016.

[153] S. Das and J. Prasad, "Cowl deflection angle in a supersonic air intake," *Defence Science Journal*, vol. 59, no. 2, 2009.

[154] S. Das and J. Prasad, "Unstart suppression and performance analysis of supersonic air-intake adopting bleed and cowl bending," *IE (I) Journal–AS*, vol. 91, pp. 27–35, 2010.

[155] S. Das and J. K. Prasad, "Starting characteristics of a rectangular supersonic air-intake with cowl deflection," *The Aeronautical Journal*, vol. 114, no. 1153, pp. 177–189, 2016.

[156] J. Donbar, M. Brown, G. Linn, and K.-Y. Hsu, "Simultaneous high-frequency pressure and tdlas measurements in a small-scale axisymmetric isolator with bleed," in *50th AIAA Aerospace Sciences Meeting including the New Horizons Forum and Aerospace Exposition*, p. 331.

[157] Y. Fan, J. Chang, W. Bao, and D. Yu, "Effects of boundary-layer bleeding on unstart oscillatory flow of hypersonic inlets," *The Aeronautical Journal*, vol. 114, no. 1157, pp. 445–450, 2016.

[158] J. Häberle and A. Gülhan, "Internal flowfield investigation of a hypersonic inlet at mach 6 with bleed," *Journal of Propulsion and Power*, vol. 23, no. 5, pp. 1007–1017, 2007.

[159] A. Hamed, S. Manavasi, D. Shin, A. Morell, and C. Nelson, "Effect of reynolds number on supersonic flow bleed," in *48th AIAA aerospace sciences meeting including the new horizons forum and aerospace exposition*, p. 591.

[160] G. J. Harloff and G. E. Smith, "Supersonic-inlet boundary-layer bleed flow," *AIAA journal*, vol. 34, no. 4, pp. 778–785, 1996.

[161] D. Herrmann, S. Blem, and A. Gulhan, "Experimental study of boundary-layer bleed impact on ramjet inlet performance," *Journal of Propulsion and Power*, vol. 27, no. 6, pp. 1186–1195, 2011.

[162] J. Iannelli, "A distributed wall mass removal system for improving scramjet isolator performance," in *46th AIAA Aerospace Sciences Meeting and Exhibit*, p. 65.

[163] K. Kobayashi, S. Tomioka, T. Hiraiwa, K. Kato, T. Kanda, and T. Mitani, "Suppression of combustor-inlet interaction in a scramjet engine under m4 flight conditions," in *39th AIAA/ASME/SAE/ASEE Joint Propulsion Conference and Exhibit*, p. 4737.

[164] M. Kodera, S. Tomioka, T. Kanda, T. Mitani, and K. Kobayashi, "Mach 6 test of a scramjet engine with boundary-layer bleeding," in *12th AIAA International Space Planes and Hypersonic Systems and Technologies*.

[165] T. Kouchi, T. Mitani, and G. Masuya, "Numerical simulations in scram-

jet combustion with boundary-layer bleeding," *Journal of propulsion and power*, vol. 21, no. 4, pp. 642–649, 2005.

[166] J. Lee, M. Sloan, and G. Paynter, "Lag model for turbulent boundary layers over rough bleed surfaces," *Journal of Propulsion and Power*, vol. 10, no. 4, pp. 562–568, 1994.

[167] C.-h. Li, H.-j. Tan, and D.-p. Wang, "Influence of secondary flow injection angle on a fluidic shock control technique," *Journal of Propulsion and Power*, vol. 31, no. 2, pp. 674–684, 2015.

[168] S. Lim, D. H. Koh, S. D. Kim, and D. J. Song, "A computational study on the efficiency of boundary layer bleeding for the supersonic bump type inlet," in *47th AIAA Aerospace Sciences Meeting including the New Horizons Forum and Aerospace Exposition*, p. 34.

[169] E. Loth, F. Roos, D. Davis, J. Mace, R. Jaiman, S. White, C. Dutton, and C. Dutton, "Mesoflap and bleed flow control for a mach 2 inlet," in *42nd AIAA aerospace sciences meeting and exhibit*, p. 855.

[170] T. Mitani, N. Sakuranaka, S. Tomioka, and K. Kobayashi, "Boundary-layer control in mach 4 and mach 6 scramjet engines," *Journal of Propulsion and Power*, vol. 21, no. 4, pp. 636–641, 2005.

[171] L. T. Obey, G. W. Englert, and T. J. Nussdorfer Jr, "Pressure recovery, drag, and subcritical stability characteristics of conical supersonic diffusers with boundary-layer removal," 1952.

[172] S. Rolston and S. Raghunathan, "An application of passive control to the shock wave boundary layer interaction in high speed intakes," in *12th Applied Aerodynamics Conference*, p. 1837.

[173] T. Sato and S. Kaji, "Study on steady and unsteady unstart phenomena due to compound choking and/or fluctuations in combustor of scramjet engines," in *AlAA 4th International Aerospace Planes Conference*, p. 5102.

[174] M. A. Shadab and M. Baig, "Investigation and control of unstart phenomenon in scramjets," in *21st AIAA international space planes and hypersonics technologies conference*, p. 2298.

[175] M. R. Soltani, J. Sepahi Younsi, and A. Daliri, "Performance investigation of a supersonic air intake in the presence of the boundary layer suction," *Proceedings of the Institution of Mechanical Engineers, Part G: Journal of Aerospace Engineering*, vol. 229, no. 8, pp. 1495–1509, 2015.

[176] M. R. Soltani, J. S. Younsi, and M. Farahani, "Effects of boundary-layer bleed parameters on supersonic intake performance," *Journal of Propulsion and Power*, vol. 31, no. 3, pp. 826–836, 2015.

[177] J. Syberg and J. L. Koncsek, "Bleed system design technology for supersonic inlets," *Journal of Aircraft*, vol. 10, no. 7, pp. 407–413, 1973.

[178] S. Im, H. Do, and M. A. Cappelli, "The manipulation of an unstarting supersonic flow by plasma actuator," *Journal of Physics D: Applied Physics*, vol. 45, no. 48, 2012.

[179] K. Yuceil, A. Valdivia, J. Wagner, N. Clemens, and D. Dolling, "Active control of supersonic inlet unstart using vortex generator jets," in *39th AIAA Fluid Dynamics Conference*.

[180] D. Baccarella, Q. Liu, A. Passaro, T. Lee, and H. Do, "Development and testing of the act-1 experimental facility for hypersonic combustion research," *Measurement Science and Technology*, vol. 27, no. 4, 2016.

요 약

이중모드 스크램제트 흡입구 불시동 현상 및 경계층 유출을 통한 불시동 제어에 대한 통합적인 연구가 진행되었다. 먼저 초음속 유동 내의 경계층 유출 기법의 성능을 알아보기 위해 이중모드 스크램제트 격리부 유동을 2차원 압축성 층류 유동으로 모델링을 진행하였다. 이 때 벽면에서의 수직방향 속도를 가정하여 경계층 유출을 모사하였으며 이를 통하여 얻은 속도 및 온도 프로파일을 통해 경계층 유출 기법의 성능을 다양한 운용조건에서 예측하였다. 결과로써 경계층 유출량이 약 1 % 근처에서 유출에 의한 효율이 최대가 됨을 알아내었으며, 이를 통하여 유로 내의 질식유량을 약 20 % 이상 증가시킬 수 있음을 확인하였다. 또한 위와 같은 환경에서 경계층 유출을 시도할 경우 경계층 유출이 최대성능을 보이기까지 약 수십 밀리초가 걸릴 수 있음을 보였다.

다음으로는 경계층 유출 기법을 실제 이중모드 스크램제트 격리부에 적용한 불시동 유동제어 실험을 진행하였다. 이를 위해 사각형 등단면적 이중모드 스크램제트 모델을 제작하였으며, 이 스크램제트 모델은 일반적인 이중모드 스크램제트 내부유동을 모사하기 위하여 흡입구, 격리부, 연소기, 공동형 화염안정기 및 노즐을 탑재하였다. 위와 같은 스크램제트 모델을 블로우-다운(blow-down)형 초음속 풍동을 이용한 실험을 진행하였으며, 경계층 유출을 위해 여러 개의 구멍이 뚫린 타공판을 설치하였으며, 위와 같은 타공판에 초고속 솔레노이드 밸브를 장착하여 경계층 유출 유동을 제어하였다. 또한 초음속 풍동에 탑재된 아크 히터를 켜고 끔으로써 저엔탈피 및 고엔탈피 자유류 흐름 모두를 모사하여 두 가지 다른 실험을 진행하였다.

먼저 저엔탈피 자유류 조건에서는 흡입구 불시동을 모사하기 위해 마하 6의 자유류 흐름 내 스크램제트 내부에 비반응성 제트를 과다주입하였다. 이를 통하여 불시동중인 유동과 불시동된 유동의 현상론적 이해증진을 목표로 하였다. 이를

위하여 초고속 쉴리렌(Schlieren) 기법을 통하여 스크램제트 모델 전체 영역의 유동가시화를 진행하여 내부유동을 분석하였다. 또한 흡입구 불시동 현상의 세기에 따른 분석을 위해 두 가지 제트주입량을 선정하였으며 이를 통하여 흡입구 불시동 완료시간이 다른 두 가지의 불시동 현상을 관찰하였다. 제트주입량이 낮은 약한 불시동 조건에서는 경계층 유출을 통한 유동제어가 빠르게 진행되면 흡입구 불시동이 완전히 회피될 수 있음을 보였다. 그렇지 않을 경우 흡입구 불시동이 약 수십 밀리초 지연됨을 확인하였다. 또한 경계층 유출을 사용하면 불시동된 흡입구의 재시동이 더 빠르게 일어날 수 있음을 관찰하였다.

고엔탈피 조건에서는 마하 4.5, 전온도 약 2,400 K의 자유류 조건에 대해 실제 연료인 상온 상태의 에틸렌(C_2H_4)을 주입하여 열적 질식을 통한 흡입구 불시동 현상을 야기하였다. 또한 벽면압력측정 및 CH^* 화학종의 화학발광현상(chemiluminescence)을 가시화하여 불시동 현상이 일어나는 현상의 전조(pre-cursor) 및 이에 따른 내부유동현상의 변화를 정량적으로 계측하는 것에 중점을 두었다. 같은 모델을 사용하여 진행된 고엔탈피 조건 실험의 경우, 에틸렌 주입의 당량비가 충분히 낮을 경우 스크램제트 모델이 램모드로 동작함을 확인하였다. 여기에서 당량비를 더 높여 일정 이상보다 에틸렌을 더 많이 주입할 경우 흡입구 불시동 현상이 나타남을 관찰하였다. 위와 같은 흡입구 불시동 현상은 급격한 압력하강, 고주파 압력섭동 감쇠 및 CH^* 화학종의 화학발광 세기 저하로 나타났으며 이를 불시동 현상의 지표로서 사용할 수 있었다. 위와 같은 불시동 지표 현상들은 당량비를 높일수록 더욱 이르게 발생하였다. 고엔탈피 조건에서 발생하는 불시동중인 유동에 경계층 유출을 적용했을 경우 흡입구 불시동이 약 수십 밀리초 지연되었으나 저엔탈피 조건에서처럼 흡입구 불시동이 완전히 회피되지는 않았다. 흡입구 불시동의 지연시간은 경계층 유출이 더 빠르고 더 많은 유량으로 작동될 경우 더 길어짐을 확인하였다.

주요어: 이중모드 스크램제트, 흡입구 불시동, 유동제어, 경계층 유출
학번: 2016-20666